AN ABSTRACT OF THE THESIS OF

Bertrand P.E. Dano for the degree of Master of Science in Mechanical Engineering presented on October 12, 2000. Title: Flow Characteristics of Semi-confined Impinging Jet Arrays

Abstract approved: Redacted for Privacy

James A. Liburdy

The present study proposes to investigate the flow structure of different arrays of jets impinging on a flat surface enclosed by three walls, creating a channel that forces the air to leave in one preferential direction, generating a self sustain crossflow. Details of both the mean and some turbulence quantities for two 7x7 jet arrays are presented. The first array was a circular orifice array while the second was a "cusped" ellipse array. The non-symmetry of the cusped ellipse shape allowed two alignments with the crossflow, one where the crossflow was along the major axis (0°) and one where the crossflow was along the minor axis (90°). The Reynolds number ranged from 8,500 to 15,900.

Surface flow visualization, jet orifice flow coefficient measurements and PIV measurements of the entire flow field were used to interpret the complex flow characteristics. The mean velocity, turbulent kinetic energy, mean vorticity and mean squared vorticity fields were calculated from the PIV data at three different locations

along the downstream flow direction: close to the back, at the center of the jet array and close to the exit.

The visual observation of the impinging flow pattern shows similar results for all of the different geometries and configurations. The jets generated cells defined by detachment-reattachment zones with a characteristic "horseshoe" shape around each jet. The cells become increasingly more oblong in shape with increasing crossflow due to an uneven shifting of the upstream and downstream cell boundaries, in the downstream direction. The flow coefficient of each jet decreases monotonically and quasi-linearly along the crossflow direction while the average value increases only a few percent for increasing Re. PIV measurements of the entire flow field in the vicinity of the jet exits reveals complex flow structures. A large rotating vortex created by the merging of the crossflow and the jet column return-flow, moves towards the jet column as the crossflow increases in strength. This interaction appears to generate multiple turbulent flow patterns that may have consequences in improved surface cooling. For the lower values of Re, the cusped ellipse jet array, placed in the (0°) position, appears to generate significantly more turbulence than the circular jet array. For higher values of Re, both configurations show similar results. But when placed in the (90°) position, there is a considerably smaller increase in the levels of turbulence when compared to the circular jets. Evidence of axis switching in the jet column for the cusped ellipse jets tends to prove that a transport in the lateral direction could be a secondary factor to take into account for surface cooling efficiency.

Flow Characteristics of Semi-confined Impinging Jet Arrays

by

Bertrand P.E Dano

A THESIS

submitted to

Oregon State University

in partial fulfillment of
the requirement for the
degree of

Master of Science

Presented October 12, 2000
Commencement June 2001

Master of Science thesis of Bertrand Dano presented on October 12, 2000

APPROVED:

Redacted for Privacy

Major Professor, representing Mechanical Engineering

Redacted for Privacy

Head of Department of Mechanical Engineering

Redacted for Privacy

Dean of Graduate School

I understand that my thesis will become part of the permanent collection of Oregon State University libraries. My signature below authorizes release of my thesis to any reader upon request.

Redacted for Privacy

Bertrand Dano

ACKNOWLEDGEMENT

I would like to thank my parents (Raymond and Nicole) and the rest of my family members for their endless support, patience and love.

I would like to offer my deepest thanks to all the teachers I ever had, past and present, east and west, scientific and non-scientific, and in particular to Dr Liburdy who brought my interest in science and in life together. Thanks to all the members of my committee: Dr Pence, Dr Kanury and Dr. Skyllingstad.

I would like to thank all my colleagues and especially Brian Daniels for his help and suggestions throughout the entire experimental process.

My warmest appreciation I also express to "Stevy" Adams, who did much more than help with the experimental setup. His comments and suggestions were invaluable and were matched only by his patience for my antics.

Finally, I extend my grateful thanks to all my friends who in any way, helped, supported and encouraged me.

TABLE OF CONTENTS

TABLE OF CONTENTS (Continued)

LIST OF FIGURES

LIST OF FIGURES (Continued)

LIST OF FIGURES (Continued)

LIST OF FIGURES (Continued)

LIST OF FIGURES (Continued)

LIST OF FIGURES (Continued)

LIST OF TABLES

NOMENCLATURE

A_j	Jet exit area, m^2
A_T	Total jet exit surface area, m^2
D_H	Hydraulic orifice diameter, m
H	Height of jet array above surface, m
$\dot{M}$	Mass flow rate, kg/s
N_j	Number of jets
Q_R	Volume flow rate readout from flowmeter, m^3/s
Q_A	Actual volume Flow Rate, m^3/s
Re	Reynolds number, $\dot{M} D_H/A_j\mu$
S	Spacing from jet center to center, m
S_C	Stagnation Point Size
S_{VS}	Surface vortex stagnation to stagnation point distance
S_S	Surface vortex separation distance
T_j	Jet air temperature, °C
T_a	Ambient temperature, °C
X	Distance along the streamwise direction, m
Z	Height of jet array above impingement surface, m
μ	Viscosity,
ρ	Density, kg/m^2

Flow Characteristics of Semi-confined Impinging Jet Arrays

CHAPTER I
INTRODUCTION

Background

Many engineering applications currently use jet impingement to improve the cooling of micro- and macro-systems. The use of impinging jets of air in industrial applications evolved rapidly from a single jet to arrays of jets, providing better mixing and/or a more uniform cooling.

Numerous combustion systems, such as airplane jet engines, are substantially improved using jet arrays "mixers" due to their superior mixing and their lower noise levels. The glass uniformity and transparency is an example of this uniform cooling capability where an array of air jets is used to quench the glass still hot from the foundry. Gas turbine industries often use rows of jets to cool large turbine blades with operating temperature above 1,000°F. Inside the blades, a core/tubing system supplies air to multiple orifices disposed along the inner surface. Each hole generates a jet that impinges on the inside surface of the turbine blade, reducing the temperature and the temperature gradient of the blade. In this specific case, the impinging air carries away the heat but also generates a cross flow that

influence the cooling effect of the other jets. Special military applications also use air jet arrays. The V.S.T.O.L (Vertical/Short Take Off and Landing) system used on various tactical military fighters found air jet arrays to help the planes take off quasi-vertically. The uniformity of the jet creates a more stable base to sustain the military airplane above the ground.

Specific Objectives

The present study proposes to investigate the flow structure of different arrays of jets impinging on a flat surface in the presence of a crossflow. The surface is enclosed by three walls, creating a channel that forces the air to leave in one preferential direction, generating a crossflow. Two jet nozzle geometries are studied: a circular cross section and a cusped ellipse cross-section. The cusped ellipse nozzle offers a non-axisymmetric shape and suggests two different orientations: aligned parallel to the crossflow and normal to the crossflow.

The goal of this study is to achieve two main objectives. The first focuses on understanding the crossflow-to-jet interaction along the flow and the corresponding effect of the impingement distance and the flow rate (or Reynolds number). The second objective is to identify any specific behavior for a jet array with a non-axisymmetric geometry (cusped ellipse).

CHAPTER II

LITERATURE REVIEW

This literature surveys four principal area of interest: free stream jet arrays, jet arrays with a crossflow, jet array with impingement and finally, jet arrays with crossflow and impingement. In the free stream jet arrays literature review, the co-flowing jet interaction and mixing distance will be emphasized along with the role of the flow structure in the mixing process. Different experiments on the use of jet arrays for cooling purposes will be discussed, emphasizing the flow characteristics rather than the cooling efficiency. Then, the use of jet arrays in presence of a crossflow or an impingement surface will be presented. Finally, the effect of an impingement plate and a self-induced crossflow will be presented with special attention being given to the experimental methods used.

Jet Arrays without Impingement or Crossflow

Raghunathan and Reid (1) investigated the noise level and flow structure of multiple air jets. The number of nozzles was varied from 5 to 9 and arranged in a circle around a central jet. The total nozzle area for each configuration was kept constant at 9.75mm^2. Using a Pitot tube, they measured the velocity profiles at different distances along the central axis. For the multiple jet configurations, the

peak velocity of the outside jets appears to shift closer to the center axis until they merge into a single unique jet. The downstream merging distance is about $Z/D_0=14$ for the 5-jet configuration. For the single jet the axial velocity stay constant until $Z/D_0=5$ where it starts to decrease asymptotically until $Z/D_0=20$ where it remains constant. This axial velocity decay starts to drop earlier at $Z/D_0=2$ for the 9-jet configuration, and reach its asymptotic value at about $Z/D_0=10$. The rate of decay appears to increase with the number of jets. After a distance of $Z/D_0=50$, the axial velocity is less than 2% than the exit velocity and the differences between the multiple-jet configurations are not significant. Concerning the noise level, a significant reduction of noise is observed compared to a single jet but the noise reduction difference between 5 and 9-jets is very small.

Moustafa et al. (2) studied the modified behavior of a twin-jets configuration in addition of a third jet, creating a triple air jets configuration. The nozzles were arranged in an equilateral triangular configuration for different jet-to-jet spacing (12, 16, 18 and 22 mm). Velocity profiles were measured along the central axis using a three-hole Pitot tube. Three different planes were studied: across the flow of the twin-jets, across the center line between the twin-jets and the third jets, and across the flow of the third jet. Results shows that the velocity decay of the third jet is more rapid than for a single jet and strongly dependent of the jet-to-jet spacing. The base twin-jets merge together to form a unique jet further downstream and this merging distance increases with nozzle spacing while the potential core length decreases with bigger nozzle spacing. At the exit, the

spreading rate of the twin-jets appears to be larger than for the third jet. Along the symmetry axis, the spreading rate of the twin-jets increases, but much slower that of the third jet. At an intermediate location of approximatly Z/D_0=20, the spreading rate of the three jets crossover. The entrainment of the three jets generates a low pressure in the interior region between the jets. Due to this low pressure and the difference in velocity profiles, the jets attract each other and an axis switching occurs. This phenomenon is found to enhance the entrainment as well as the mixing of the jets.

Moustafa, and Rathakrishnan (3) took the preceding results one step further and studied the behavior of four jets in a square formation with the same flow conditions. This configuration shows the same behavior as the three jet array, except for the spreading rate: starting with a larger value, the spreading rate of the 4-jet array increases slightly faster than that of the 3-jet configuration. Therefore, the crossover takes places much further downstream at about Z/D_0=50.

Villermaux and Hopfinger (4) investigated the interaction of circular jets set in a large network. Perforated plates with two different configurations were studied: a square network with 1mm diameter holes with a mesh size of S=2.54mm and a triangular network of 0.8mm diameter holes with a mesh size of S=2.73mm. The perforated plates were placed into an 80x80 mm^2 cross-section wind tunnel designed for low residual turbulence. Measurement of the velocity fluctuations were performed with one or two independent hot-wire probes, while the mean velocity measurement was made with a Pitot tube attached to a differential pressure

sensor. Flow visualization was performed using a continuous laser and a 25 fps digital camera. The laser beam was directed on an oscillating mirror, generating a 1mm laser-sheet, which was aligned with a row of jets, inside the wind tunnel test section. A smoke generator injected dense white smoke at a distance of 10xS (where S is the mesh size) upstream of the network and with an injection velocity equal to the mean wind-tunnel velocity. A large-amplitude quasi-periodic oscillation was observed at the jet merging distance for $300<Re<3\text{-}4x10^3$. This instability appears to be part of a feedback process. A weak positive pressure gradient eases the creation of a recirculation flow in the cavity formed by co-flowing jets. The authors implemented a new model (non-linear delay saturation) that proved to be in close agreement with the experiment results.

Jet Arrays with Crossflow

Kim and Benson (5) proposed a computer simulation of a row of jets in a confined crossflow without impingement. Using a finite volume method to solve the Reynolds-averaged Navier-Stokes equations, they successfully reproduced the complex flowfield in the vicinity of the jet exit for low Re (~500). A primary vortex is observed immediately downstream of the jet. Due to the blockage of the crossflow, a recirculation flow is formed in the wake of the jet. A strong adverse pressure gradient is formed, creating a reverse flow, upstream of the jet. This

reverse flow and crossflow interaction leads to the formation of a secondary vortex, formed upstream of the jet, in the streamwise plane of symmetry. In the spanwise direction, the secondary vortex is deflected along the jet column, creating a helical vortex shaped like a horseshoe.

Jet Arrays with Impingement

Arjocu and Liburdy (6) investigated the effect of non-axisymmetric orifice jets using a 3x3 array of elliptic jets on an impingement surface. The jet orifice aspect ratio was set to the values r=2 and 3. The jet hydraulic diameter was D_H=9mm, the Reynolds number ranged in 300<Re<1,500 and the impinging distance was varied between H/D_H=1 and 5. The authors used flow visualizations in three planes: two were placed along the central row of jets along the major and minor axis of the ellipse while the third one was placed parallel to the surface, at a distance of Z/D_H=1/9, from the impingement surface. Using a 1mm thin argon-ion laser sheet to illuminate the flow, 60 μm size glass micro-particles were introduced as tracers while a CCD camera recorded the images. Particle Image Velocimetry, (PIV) measurements were also obtained using 27μm fluorescent micro-beads and illuminating the planes with a pulsed Nd:YAG laser. Finally, velocity measurements at different locations were obtained using a hot-film anemometer. Based on the velocity measurements, the vorticity field was also computed. The

results show that at the higher impingement distances, the jet streamlines converge in the major axis planes while they spread in the minor axis plane. This behavior is typical of non-symmetric jet orifices and is known as "axis switching". The axis switching superimposed on the jet column instability, swaying motion, and presence of small-scale shear layer structures leads to a high level of turbulence and entrainment in the impingement region.

Jet Arrays with Crossflow and Impingement

Barata et al (7) examined the crossflow effects on twin-water-jets impinging on a surface in two different configurations: a uniform crossflow normal to the jets, and a crossflow with a third jet placed upstream of the twin-jets. The twin-jets separation distance was 5D and the distance to the third jet is 15D (where D is the diameter of the jet). For all the experiments, the impingement distance was kept at H/D=5, the Reynolds number was kept constant (Re=105,000) as well as the jet-to-crossflow velocity ratio at V_j/V_c=30. Several flow visualizations were performed using a continuous argon-ion laser while air bubbles were injected in the crossflow. The beam was expanded through a cylindrical lens to produce a 2mm thick laser sheet, which was aligned with the downstream flow with the plane of symmetry between the twin-jets. Mean and turbulent velocities were measured with a dual-beam, forward-scatter laser Doppler anemometer. For both configurations, an

upwash fountain flow was observed in the symmetry plane, and upstream of the twin-jets position. They noted that while impinging, the twin-jets form a wall jet that interacts with the crossflow, creating a complex vortical structure, referred to as a horseshoe vortex, wrapped like a scarf around then twin-jets. For the three-jet configuration, the recirculation zone appears to be extended upstream and confined between the singular jet and the twin-jets.

Later, Barata (8) proposed a numerical study to correlate these results. Based on time averaged Navier-stokes equations and the k-ε turbulence model, the numerical results show a very good agreement with the previous experiments. The model adequately represents the fountain upwash flow and reveals a large low-pressure zone, resulting from the acceleration of the crossflow around the twin-jets.

Florschuetz and Isoda (9) studied the flow distribution of circular air jets impinging on a surface. The jets were arranged into arrays of ten spanwise parallel rows with the number of jets in the streamwise direction varying between 9 and 36, depending on the jet-to-jet spacing. The impingement distance was varied with values of 1D, 2D, and 3D, with D being the jet exit diameter. The impinging flow was constrained to exit in a single direction by an independent crossflow, with jet flow rate ratio values of 0.2, 0.5, and 1.0. The pressure measurement was achieved by introducing a static pressure probe at a determined position along the downstream direction, at the bottom surface of the channel. The jet plate flow coefficient C_D was obtain as the ratio of the actual to the ideal flow rate:

$$C_D = \frac{\dot{M}_{Actual}}{\dot{M}_{Isentropic}}$$

where $\dot{M}_{Actual}$ is the actual mass flow rate measured with an orifice meter upstream of the jet plate and $\dot{M}_{Isentropic}$ was computed assuming one-dimensional isentropic ideal gas flow. The results show that the average value of C_D can be considered a constant for crossflow-to-jet velocity ratios smaller than one and decreases asymptotically from 0.85 to 0.50 for a crossflow-to-jet velocity ratio between 1.0 and 3.0, respectively. C_D was not found to be very sensitive to Re_D variations ($0<Re_D<40,000$), with deviations from the mean value no larger than a few percent. The authors also presented a theoretical and a numerical model based on a one-dimension assumption, which numerical results are in excellent agreement with the experimental results. It is also observed that for the smaller impingement distance. Z/D=1, C_D strongly decreases, thought to be due principally to wall shear effects.

Most recently, Bernard et al. (10) extended Barata's results on the "horseshoe vortex" in the specific case of an array of round jets within their own crossflow. The impingement surface is enclosed between three walls, leaving a unique direction for the flow to exit. The array was made of 5x3 orifices with a diameter of D=10mm. The separation distance was set at 4D and the impingement distance was kept constant at H/D=2. The Reynolds number was chosen to be Re=12,600. Various experimental techniques were used: surface flow visualization, laser sheet visualization, and laser-Doppler velocity measurement. The surface flow visualization has been achieved by spreading a mixture of calcium carbonate

particle suspended in oil, over the impingement surface. The results reveal the cellular aspect of the flow near the impingement surface and the detachment zone separating each jet impingement area to the others. Laser sheet visualizations were performed using an argon-ion laser (~1mm laser sheet) illuminating sections of the flow. A glycerin and water mixture was sprayed into the flow while a S-VHS camera (50 fps) was used to record images. A similar rotating structure as Barata's "ground vortex" was observed upstream of the impinging jets. The fountain flow was also observed between co-flowing jets. Finally, velocity measurements were performed using a LDA system, providing the three velocity components in the test section. Combining these different techniques, the authors proposed a topology of the flow structure including the ground vortex structure and the fluid behavior in the vicinity of the plane wall. This topology is shown in figure 2.1.

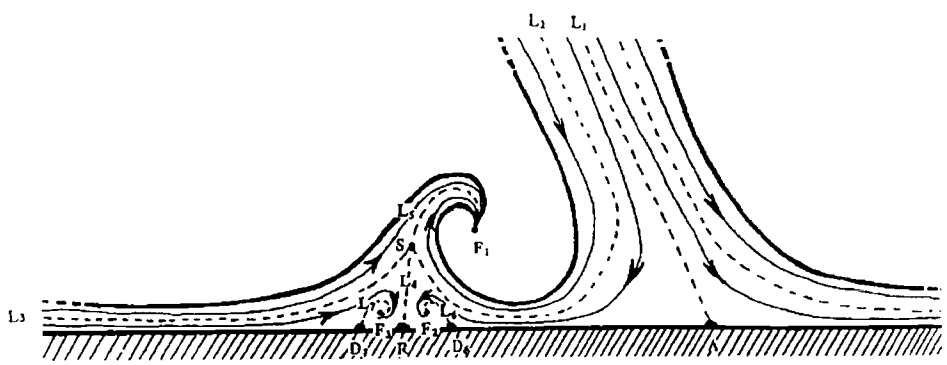

Figure 2.1 Impinging jet topology

Many authors investigated the heat transfer distribution from impinging jets and jet arrays. In these studies, the cooling efficiency was emphasized rather than the flow mechanism. Meanwhile, the effect of some parameters such as the jet spacing, the impingement distance, and the Reynolds number was analyzed, providing a comparative database to be linked with the associate flow analysis.

Metzger et al. (11) investigated the cooling effects of circular jet arrays on a impinging surface enclosed between three walls. The impinging air is forced to exit in one direction, creating a crossflow. The crossflow-to-jet velocity ratio ranged from 0 to 0.8. The jet spacing was varied from 4D to 8D, with D being the jet diameter. The Reynolds number ranged from 2,500 to 70,000 and the impingement distance was varied between H/D= 1 and 3. The authors found that for the larger jet spacing and smaller channel height, the crossflow provided an increased heat transfer distribution. They explained that for the smaller jet spacing, the crossflow becomes canalized between adjacent rows, creating non-uniformity in the jet distribution. For the larger channel height, the authors concluded that the cooling effectiveness is reduced by the crossflow diffusive action on the jets.

A similar study was achieved recently by Koonlaya Kanokjaruvijit (12). The effect of the orifice geometry and the surface boundary condition on the heat transfer distribution of an impinging jet array are investigated for two 7x7 jet arrays. The first one is composed of circular jet nozzles while the second one is

composed of cusped-ellipse nozzles with the long axis perpendicular to the crossflow. In a similar setup as Metzger et al. (11), the impinging air is forced to exit in one direction, creating a crossflow with a crossflow-to-jet velocity ratio increasing from 0 to 0.194. The Reynolds number ranged from 5,000 to 11,000 and the impingement distance was varied between H/D_H=1 and 4. The local heat transfer was mapped using thermochromic liquid crystals for two boundary conditions: isothermal surface and uniform heat flux. The experimental results show that the cusped ellipse jet array provides a better cooling compared to the circular jet array for both boundary conditions. In addition, the results show that the cusped ellipse performance is more sensitive to Reynolds number variation.

CHAPTER III

EXPERIMENTAL SETUP

The test facility is described in the following two sections. The first section describes the compressed air delivery system which supplies air to the jet arrays, and the second section describes the impingement surface setup, including the pressure measurement apparatus, the flow visualization, and the PIV system to obtain the jet characteristics and the method used to obtain the impingement surface streamline pattern.

Air Delivery System

A 110-psi dried air compressor provides the air for of all the impingement experiments. A schematic of the air delivery system is presented in Figure 3.1. The air is passed through a filter to remove any potential impurities present in the supplied air. Then, a pressure regulator is used to damp the pressure fluctuations due to the cycling of the compressor. A persistent pressure fluctuation was still measurable and the use of a surge tank would have been a possible solution. Instead, it was decided to open another line from the air supply and vent it to the atmosphere through a needle valve. Since the compressor was designed to supply a unique maximum flow rate, the second line was set to "complete" our flow rate at

this maximum. The compressor did not cycle under these conditions and tests proved that this method reduced the fluctuations to below 0.5%. In order to turn on/off the air without changing the settings, a gate valve was installed followed by a flowmeter equipped with a needle valve for fine adjustment. A pressure gage was placed at the flowmeter outlet. This pressure was used to correct the flowmeter readout (see Appendix A). A thermocouple was also placed downstream of the flowmeter in order to measure the air temperature needed for the calculations in Appendix A.

Further downstream of the flowmeter, the air flowed into the plenum chamber through a 3.6-meter section of 25.7 mm inside diameter PVC pipe, followed by a 1.5-meter section of 35-mm inside diameter flexible tube. The plenum chamber was made of five 300x300x3.5 mm steel plates welded together. The 6th plate was tightened with 16 screws providing a quick and easy access for set-up and maintenance. A diffuser plate was placed inside the plenum chamber 11 centimeters from the top. Breaking down any turbulence of the incoming jet from the air supply, the diffuser plate generated a volume of high pressure, low velocity air above the jet array. At the center of the bottom plate was attached a mounting frame that held the jet array plate in place. The jet array plates were square pieces of steel 3.6 mm thick containing 7x7 circular holes or cusped ellipse holes. Figure 3.2 shows the different geometries and jet array spacing.

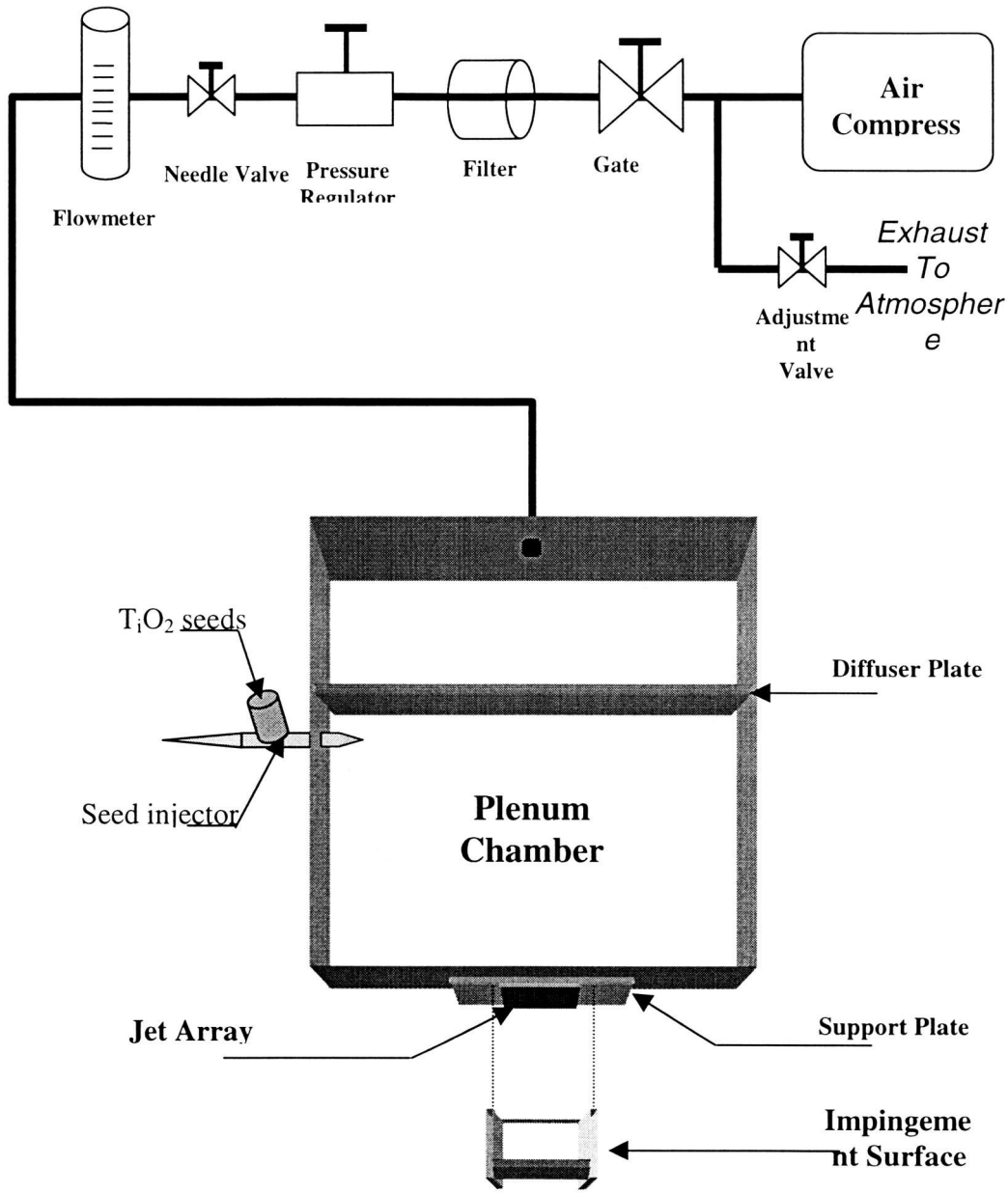

Figure 3.1. Schematic of the air delivery system

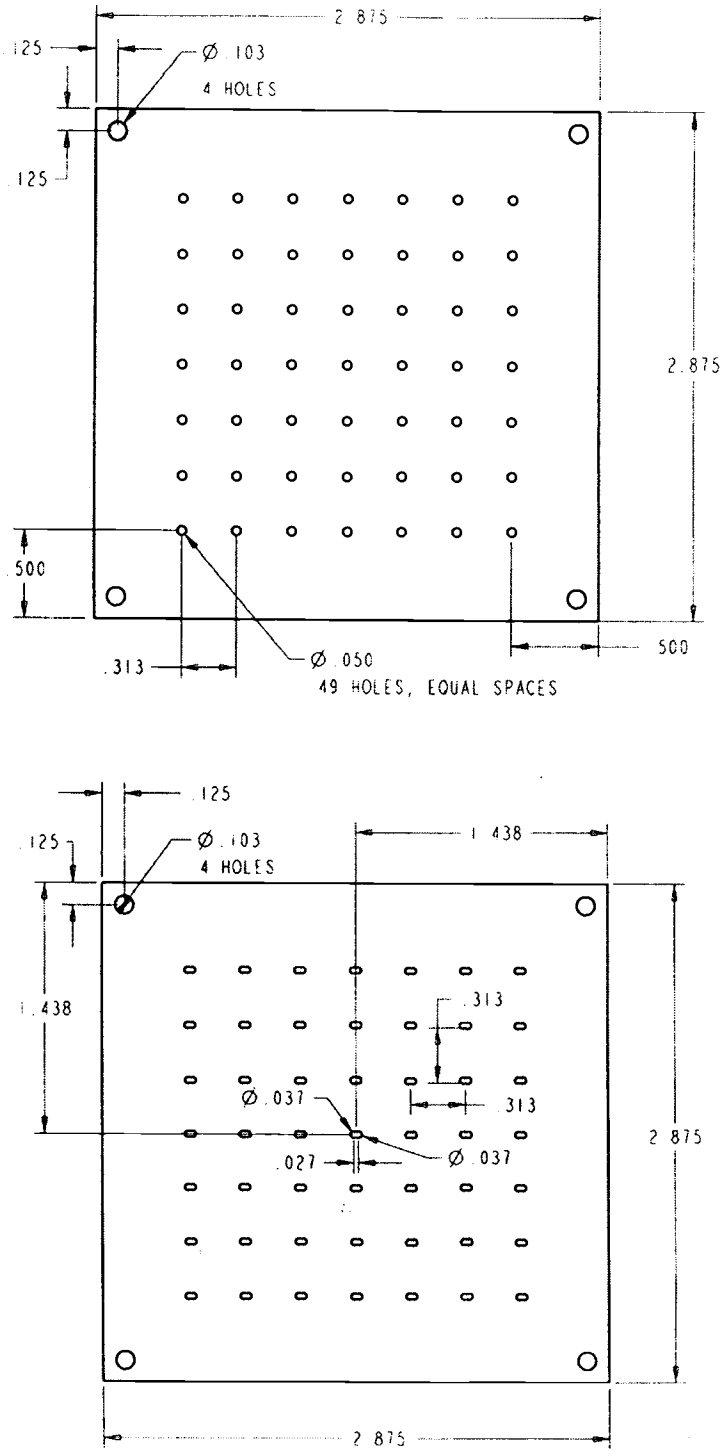

Figure 3.2. Jet arrays geometry (top: circular jet array, bottom: cusped ellipse jet array)

Impingement Surface

The impingement surface was built with 5.8 mm thick Plexiglas plates, mounted together to form a "U-shaped" channel and closed on one side (the "back wall") such that the jets generate a crossflow in the "forward" direction (Figure 3.3 shows the general setup). To provide a better viewing medium for the PIV studies, a glass window was inserted in one of the Plexiglas side walls. Two Plexiglas blocks were mounted on either side of the channel, providing a stable base to be attached to the plenum chamber's mounting frame. A thin layer of foam, with a film of silicon paste covered the tops of the walls to prevent leaks. The impingement plate was mounted in between the sidewalls, using 90° brackets fastened to the walls. A groove was machined along the impingement plate where an O-ring was placed to prevent leaks. Four pairs of metallic rods were machined at specific diameters. Each pair was used as a spacer to measure the distance in between the jet array and the impingement plate. The impingement distance to jet hydraulic diameter ratio (H/D_H) ranged from 1 to 4 (H/D_H=1, 2, 3 & 4). Once the impingement plate was fastened at the desired impingement distance, the spacers are removed and the experimental system is ready.

Since the cusped-ellipse is not an axisymmetric shape, three different cases were studied: (i) the circular jet (abbreviated CJ), (ii) the cusped ellipse with the

major axis aligned parallel the crossflow (abbreviated CE0), and (iii) the cusped ellipse with the major axis normal to the crossflow (abbreviated CE90).

Pressure Drop Measuring Apparatus

In order to obtain the pressure drop and the orifice flow coefficient, a special pressure measurement impingement plate was prepared: seven 1mm diameter holes were drilled on the impingement plate at specific locations (see Figure 3.4). Five pressure taps were placed along the central streamwise flow-line to measure the crossflow effect on the pressure drop. Two additional taps were placed on either side of the centerline on the central spanwise axis and were used to obtain the average pressure on the impingement plate, and also served as a guideline to center the impingement plate under the jet array. Each pressure tap was located halfway between two adjacent jets along the symmetry axes of the jet array. (See Figure 3.4 for more details). A needle pressure tap was inserted into each hole and connected to a pressure manifold with 4mm inside diameter flexible tube. The manifold consisted of a series of on/off valves connecting each pressure tap to a common pressure transducer. The pressure measurements were taken one at a time, which reinforced the necessity of a steady flow rate between the measurements. Two pressure-taps were also placed in the plenum chamber, on each side of the

diffuser plate, in order to measure the generating pressure and the pressure drop through the diffuser plate.

Once the desired air flow rate is set with the needle valve, the adjustment valve was set to achieve the maximum flow rate that the compressor could sustain. The needle and the adjustment valves were readjusted again until the desired flow rate was obtained and the pressure in the plenum was stabilized. Then, the pressure at the different pressure taps was acquired, switching the corresponding valves on the manifold. The pressure transducer used was a Kulite-K190, providing a resolution of 0.75 psi for a working pressure of 25 psi. The pressure transducer output was connected to a Fluke data logger that was programmed to transform the voltage directly into pressure units (psi), according to the manufacturer's calibration curve. Table 3.1 shows the different test conditions used during the pressure measurements, and then used to determine the flow coefficient.

Table 3.1. Pressure tests and conditions

Jet Array	H/D_H	Re
Circular jet (CJ)	1	9,860 - 11,880 - 13,920 - 16,760
	2	9,740 - 11,680 - 13,660 - 15,980
	3	9,740 - 11,550 - 13,590 - 15,830
	4	9,740 - 11,550 - 13,590 - 15,830
Cusped Ellipse 0° (CE0)	1	8,730 - 10,420 - 12,260 - 14,200
	2	8,560 - 10,200 - 11,830 - 13,580
	3	8,560 - 10,160 - 11,770 - 13,520
	4	8,560 - 10,160 - 11,770 - 13,520
Cusped Ellipse 90° (CE90)	1	8,730 - 10,420 - 12,260 - 14,200
	2	8,560 - 10,200 - 11,830 - 13,580
	3	8,560 - 10,160 - 11,770 - 13,520
	4	8,560 - 10,160 - 11,770 - 13,520

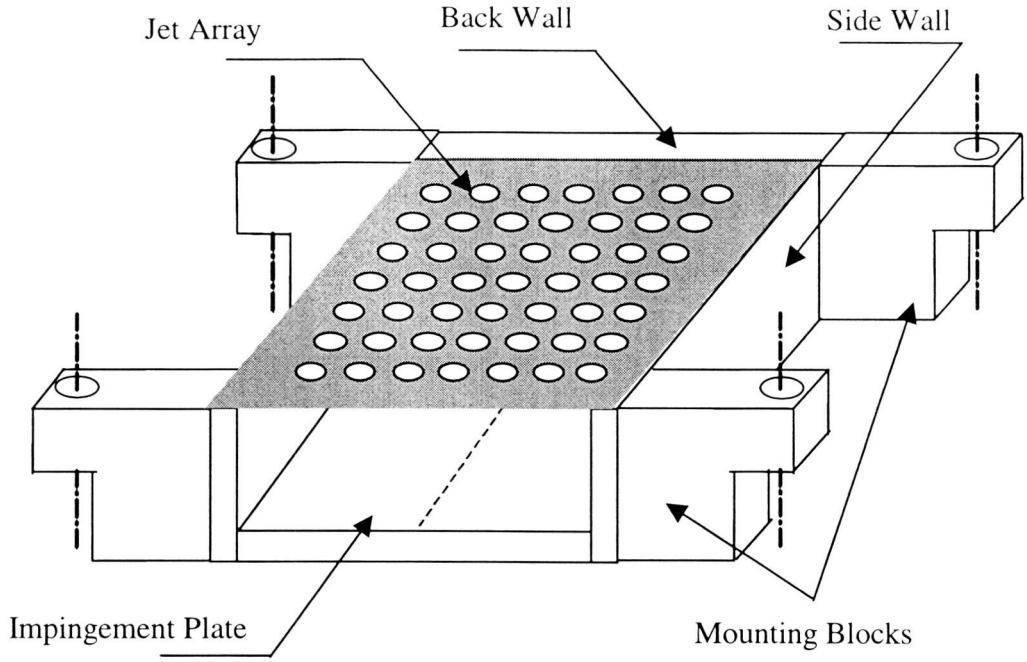

Figure 3.3. Impingement Plate Setup

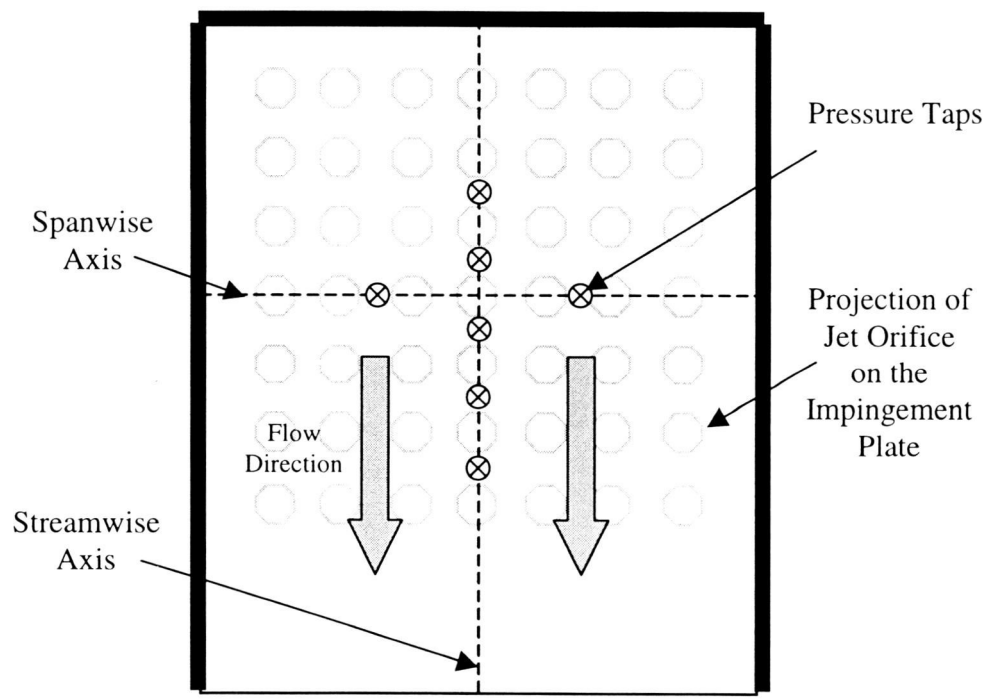

Figure 3.4. Pressure Tap Locations

Flow Visualization Apparatus

Velocity Field Measurements

Particle Image Velocimetry, PIV, provides an improved method to obtain the entire velocity field across a well define flow region. Compared to the classic single point hot-wire anemometry measurement or laser Doppler anemometry, PIV offers a non–intrusive measuring method which covers a larger field of view for instantaneous measurement. The flow is seeded with micron-size particles and a laser is pulsed through the flow-field. The seed particles scatter the laser light, which is formed into a planar sheet. By pulsing the light, two images of this field are taken at a known time delay between the two laser pulses. One can then analyze the two pictures and estimate the local velocity field within the light sheet plane.

Using a modified sand blaster as a seed-injector, the seeds were injected into the plenum chamber at mid-height, providing good mixing. Titanium Dioxide (T_iO_2) particles were used with an average particle size of 2 to 3 μm. These seeds proved to be an excellent "tracer" for PIV but also for the streamline pattern visualization. The laser, a double Nd:YAG laser, was able to perform a double pulse with a 1μs time interval at a frequency of 15 Hz. After a series of lenses, the round beam is converted into a laser sheet (<1mm thick) and directed vertically into the space between the jet array and the impingement plate (see Fig 3.5).

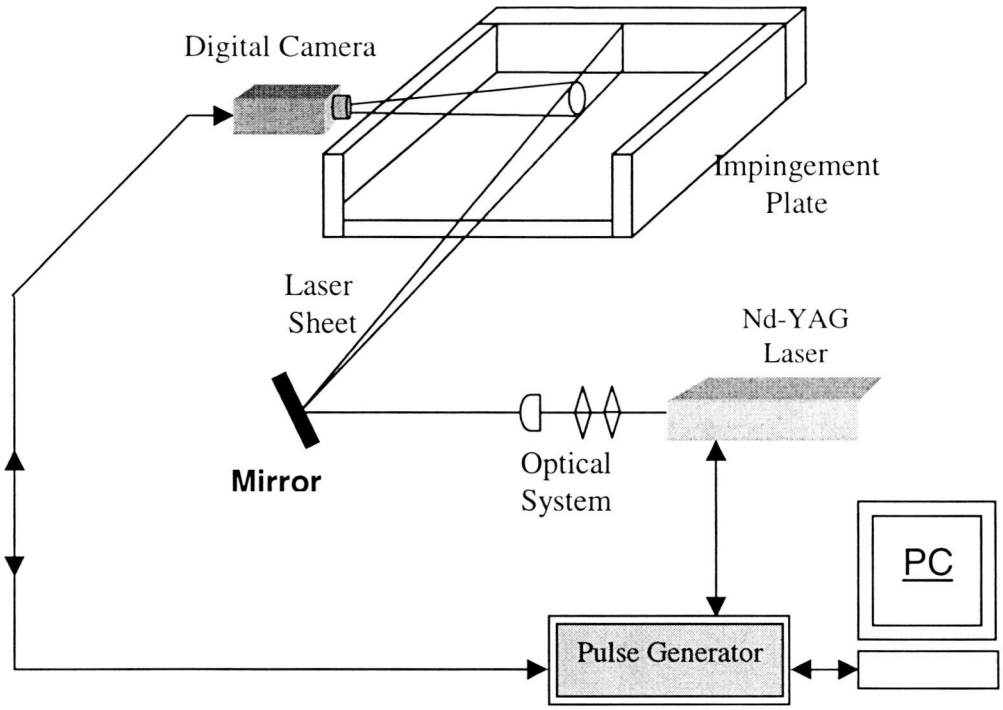

Figure 3.5. Visualization Apparatus

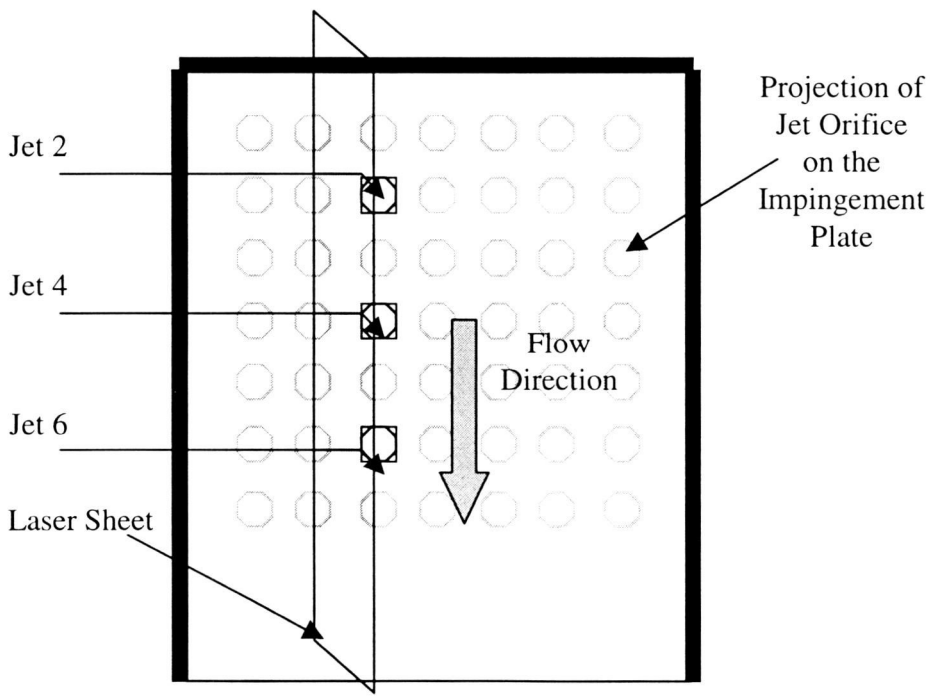

Figure 3.6. Laser Sheet Location

The laser sheet is lined up with a designated row of jets, as shown in Fig. 3.6, lighting it up at the appropriate frequency while a digital camera (placed perpendicular to the laser sheet) was capturing the images. The camera used was a Princeton Instruments, Inc. MicroMAX 5MHZ, with a CCD array resolution of 1,300x1,030 pixels. The camera and the laser were synchronized such that pairs of pictures could be taken with a time separation lower than 2μs.

P.I.V Acquisition and Software

In order to analyze the images of the seed particles to obtain the velocity field, VISIFLOW™ was used. VISIFLOW™ is software package that directly computes the velocity vector fields. For more information on the software and the parameters used for throughout the experiments, refer to Appendix B. PIV analyses have been performed for 3 jets along the adjacent row to the center streamwise row/axis (see Figure 3.6), for two volumetric flow rates (Q_R=14 and 20 CFM), and for two impingement distances (H/D_H=2 and H/D_H=4). The list of PIV tests and the corresponding Reynolds number for each geometry are shown in Table 3.2.

Impingement Surface Streamline Apparatus

Visualizations of the streamline patterns on the impingement surface were realized by seeding the flow with the same TiO_2 seeding system as used for PIV seeding. A set of exchangeable impingement surfaces was designed to suit the different tests and investigate the streamlines on the impingement surface and the sidewall surface. Made of 0.2 mm thick propylene, they offer a smooth and robust impingement layer that can be inserted in between the actual impingement surface and the jet arrays. The list of tests is given in Table 3.3. Once the flow is set to the desired flow rate, TiO_2 seeds are injected in the plenum and flow toward the impingement surface, leaving a deposit at the stagnation points and the locations of near zero velocity. Then, the air is cute-off and the impingement layer is removed. A Sony Digital Color Camera provided the 640x480 pixels pictures of the surfaces and the side walls. See Figure 3.7 and 3.8 for the surface and viewing orientations.

Table 3.2. PIV tests and conditions

Jet Array	JET #	H/D_H	Re
Circular jet	2	4	9740 - 15,800
	4	2 & 4	9740 - 15,800
	6	2 & 4	9740 - 15,800
Cusped Ellipse 0°	2	4	8,570 - 13,500
	4	4	8,570 - 13,500
	6	4	8,570 - 13,500
Cusped Ellipse 90°	2	4	8,570 - 13,500
	4	4	8,570 - 13,500
	6	4	8,570 - 13,500

Table 3.3. Streamline Visualization tests and conditions

Jet Array	H/D_H	Re
Circular jet	2	9740 - 15,800
	4	9740 - 15,800
Cusped Ellipse 0°	2	8,570 - 13,500
	4	8,570 - 13,500
Cusped Ellipse 90°	2	8,570 - 13,500
	4	8,570 - 13,500

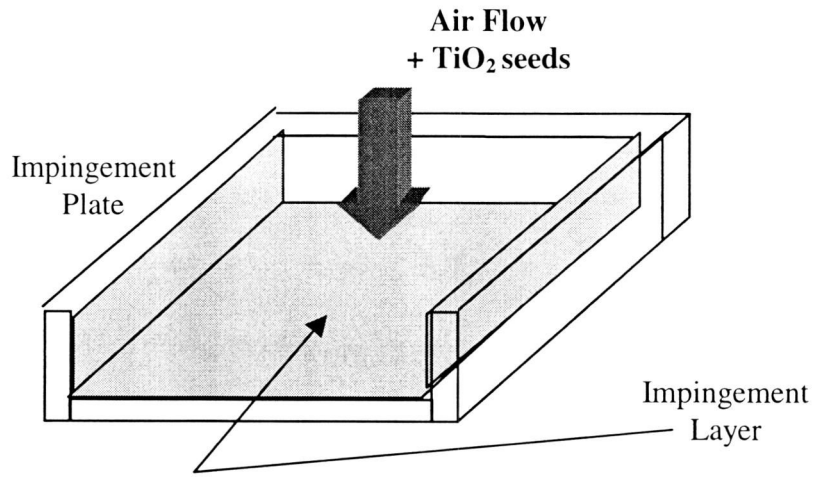

Figure 3.7. Impingement Layer Location

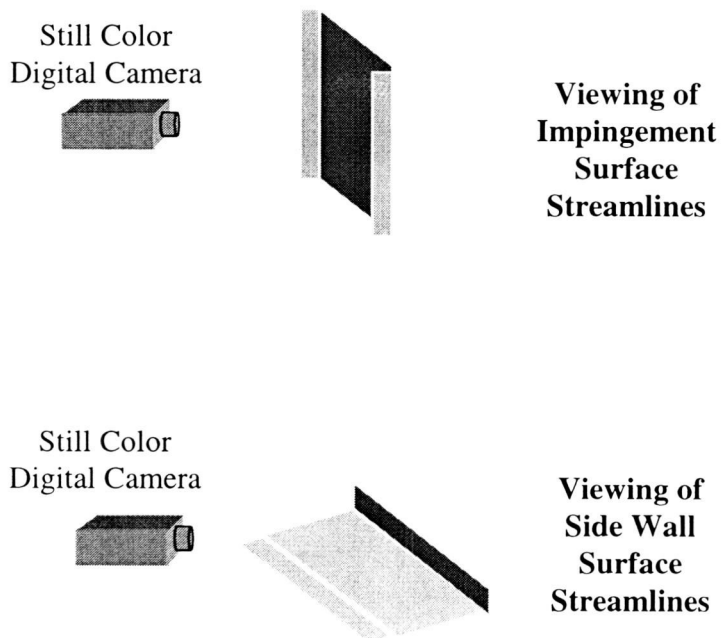

Figure 3.8. Impingement Layer Visualization

CHAPTER IV

EXPERIMENTAL DATA ANALYSIS

Velocity Ratio

The downstream location along the flow can be defined either as the jet number or the distance from the back-wall. However, the crossflow-to-jet velocity ratio, V_r, is a convenient variable used to define this location. It is defined as follows: $V_r = \frac{V_c}{V_j}$, where V_c is the velocity of the flow coming from the upstream jets, and V_j is the exit velocity of the jet. As can be seen in Figure 4.1, V_r is a linear function of the jet position with a larger slope for larger impingement distance H/D_H.

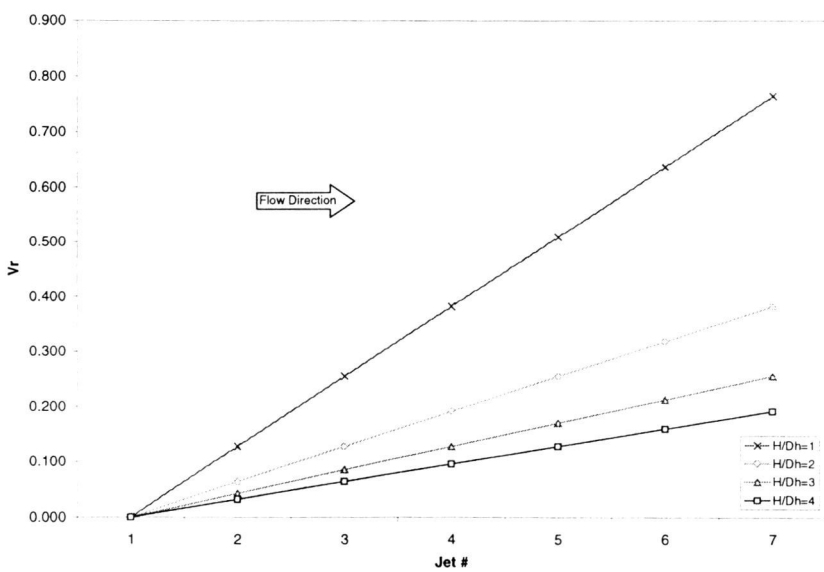

Figure 4.1 Crossflow-to-jet velocity ratio, V_r versus jet number measured from the most upstream jet.

Pressure Data

Pressure data are used to determine the flow coefficient of the jets and how it varies along the downstream flow. The flow coefficient, C_D, for an individual jet is defined as follows:

$$Cd = \frac{\dot{M}_{actual}}{\dot{M}_{isentropic}}$$

where $\dot{M}_{actual}$ is the actual mass flow rate measured from the flowmeter, and $\dot{M}_{isentropic}$ is the ideal mass flow rate (isentropic). Using the isentropic gas dynamics laws for flow through an orifice, Florschuetz and Isoda (9) expressed C_D in the following form:

$$C_D = \frac{\frac{\dot{M}_{actual}}{A_t}}{P_0\left(\frac{P}{P_0}\right)^{\frac{1}{\gamma}}\sqrt{\frac{2\gamma}{R.T_0(\gamma-1)}.\left[1-\left(\frac{P}{P_0}\right)^{\frac{\gamma-1}{\gamma}}\right]}}$$

where A_t = Total area of jets = 49 x jet orifice area ,

P = Impingement surface pressure,

P_0 = Plenum chamber pressure,

T_0 = Plenum chamber temperature.

This definition assumes that the total mass flow rate is evenly divided among the 49 jets. Prior tests were performed to verify the uniformity of the flow by using

a Pitot tube under each jet to detect any variation in the dynamic pressure and were found uniform within 2%. For each jet-array configuration, impingement distance and Re, graphs of C_D are plotted versus crossflow-to-jet velocity ratio along the center streamline and the average flow coefficient, $<C_D>$, versus Reynolds number.

Velocity and Mean Velocity Field

The field of view for the pictures is $6D_H x 4D_H$ for the higher impingement distance. Each instantaneous PIV velocity field is composed of 37x25 vectors. Therefore, the spacing between adjacent vectors is typically less than 200μm.

In order to highlight the properties and specific behavior of each jet and the interaction with the crossflow, a large number of instantaneous fields were obtained (approx. 50). All PIV realizations for each jet were filtered to show the intrinsic interaction of the jet and the crossflow. In order to smooth the data, a 5x5-smoothing filter was applied using VISIFLOW™ to each of the instantaneous flow-fields. The filter weight-coefficient table is presented in Table 4.1.

Table 4.1 Filter Weight-Coefficients

0.05917	0.10687	0.13533	0.10687	0.05917
0.10687	0.24311	0.36787	0.24311	0.10687
0.13533	0.36787	1	0.36787	0.13533
0.10687	0.24311	0.36787	0.24311	0.10687
0.05917	0.10687	0.13533	0.10687	0.05917

VISIFLOW™ provides velocity vector flow field plots, but uses an automatic scaling function (based on the maximum velocity) to make convenient flow fields without vectors crossing each other. Therefore, each smoothed flow field was exported into a data file composed of the position, magnitude and angle of each vector of the flow field. Then, all these data files were imported into MATLAB™ and processed to provide the following results. The use of a unique scale factor for all jets and all configurations provides unreadable results for very low or very high velocities. MATLAB's auto-scale feature was de-activated and the scale factor adjusted manually for each flow field for the same jet, with the same configuration, but different Re. This scaling coefficient was applied to the flow field for both Re, dividing each velocity component by the scaling factor. The scaling factor used for the different configurations is given in Table 4.2.

Table 4.2 PIV scaling factor

Configuration Case		**Jet #**	**Scaling coefficient**
Round Jet:	H/D_H=4	2	45
		4	90
		6	180
	H/D_H=2	4	90
		6	90
Cusped Ellipse (0°)	H/D_H=4	2	110
		4	130
		6	150
Cusped Ellipse (90°)	H/D_H=4	2	45
		4	80
		6	100

The larger the velocity is, the larger the scaling factor needs to be to reduce the vector length in order avoid the overlap of the adjacent vectors. Meanwhile, the mean velocity field was also displayed. Its purpose is to provide details on the velocity range and the local spot of maximum velocity.

Mean Vorticity

The mean vorticity fields are used to identify the locations of various eddies and concentrated vorticity resulting from the interaction of the crossflow and jets. Using a cell-centered finite difference scheme, the mean vorticity was computed using two different methods. First, the vorticity field based on the mean velocity field was computed, second, the vorticity field for each instant flow-field was computed, summed up and averaged to obtain an average vorticity field. Both of these methods yield the same results. The finite difference approximation used was of the form

$$\omega = \frac{1}{2}\left(\frac{\partial V}{\partial x} - \frac{\partial U}{\partial y}\right) \quad \Rightarrow \quad \omega_{i,j} = \frac{1}{2}\left(\frac{V_{i,j+1} - V_{i,j-1}}{\Delta x} - \frac{U_{i+1,j} - U_{i-1,j}}{\Delta y}\right)$$

Turbulent Kinetic Energy

The TKE field provides a good overview of the location of large scale turbulent eddy production. Using the Reynolds decomposition of the Navier-Stokes equation the turbulent kinetic energy is represented by:

$$TKE = \frac{1}{2}\left(\overline{U'^2} + \overline{V'^2}\right),$$

where $\overline{U'^2} = U_{ms} = \frac{1}{N}\sum_{n=1}^{N}\left(U_n - \overline{U}\right)^2$ and $\overline{V'^2} = V_{ms} = \frac{1}{N}\sum_{n=1}^{N}\left(V_n - \overline{V}\right)^2$.

First, the average velocity fields, $\overline{U}$ and $\overline{V}$ (x axis and z axis, respectively) are computed by averaging the local velocity components over all the instantaneous flow field. The number of instantaneous flow field used was approximately N=50 for each configuration. Then, the mean squared U_{ms} and V_{ms} are computed by subtracting the local values of U and V to the average $\overline{U}$ and $\overline{V}$ for each instantaneous flow field, respectively, then squaring the results. The TKE flow field is then obtained by averaging the local values of the two mean squared U_{ms} and V_{ms}, at each position throughout the entire flow field.

Mean Squared Vorticity

For any turbulence production, there is always an associated dissipation. Using the Reynolds decomposition of the Navier-Stokes equation the dissipation due to turbulent motion is proportional to the mean of the fluctuating vorticity squared. Therefore, taking the mean squared vorticity gives information on the location where the dissipation of TKE is concentrated. The means squared vorticity, ω_{ms}, was calculated as:

$$\overline{\omega'^2} = \omega_{ms} = \frac{1}{N}\sum_{n=1}^{N}\left(\omega_n - \overline{\omega}\right)^2 .$$

The mean squared ω_{ms} is computed, subtracting the local values of W on each instantaneous flow field to the average $\overline{\omega}$, squaring the results and finally averaging the local values over the N=50 instantaneous flow fields.

Data Reduction

In order to compare the flow characteristics for each of the cases, average levels of vorticity, TKE and mean squared vorticity were computed. The information of interest is near the impingement surface. A section of the flow has

been defined by excluding the top part of the flow and the borders. A schematic of this section is shown in Figure 4. 2.

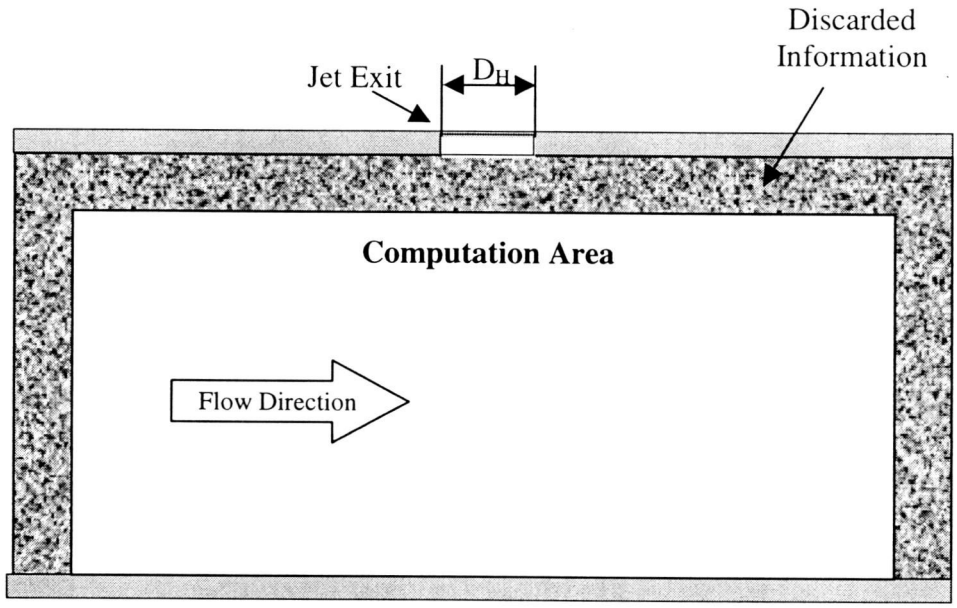

Figure 4.2 Computation area for property levels.

In the case of $H/D_H=4$, the computation area is reduced to 3.7x3.2 D_H. For $H/D_H=2$, a larger stripe of data is discarded. In that case, the area has is reduced to 3.7x2.6 D_H. The justification for this reduced computation region is provided in Chapter V, in the discussion of the side wall effect section.

Surface Flow Visualization

For each combination of jet-array geometry, impingement distance, and Re, pictures of the TiO_2 deposits have been acquired and analyzed. Direct observation of the general impingement surface provides interesting information on the impingement surface flow patterns and the locations of surface vortices. For each row aligned with the downstream flow, the dimensions and locations of the stagnation points and the accumulation rings were measured directly from the pictures, in units of pixels. With the assumption of a quasi-uniform flow, from one row to the over, in the downstream direction, averaged values have been calculated and converted into millimeters, and finally into proportions of D_H.

CHAPTER V

RESULTS AND DISCUSSIONS

This chapter discusses the results of the experiments and is subdivided into five sections: (i) flow structure versus downstream positions, (ii) effect of the Reynolds number, Re, on the flow structure, (iii) effect of impingement distance, H/D_H, on the flow structure, (iv) effect of geometry/alignment of the cusped ellipse jet array, and (v) side-wall effects. In the first section, the flow structure is described and the influence of the crossflow on the jets is discussed. The second section analyzes the effects of Re on the flow structure. The third section discusses the effects of the impingement distance, H/D_H, on the flow structure. The fourth section discusses the effects of the alignment of the cusped ellipse jet array on the flow structure. The cusped ellipse, being a non-axisymmetric shape, two configurations arises with either the major axis aligned with or normal to the crossflow direction or not. Finally, the fifth section analyzes the effects, direct and indirect, of the side walls on the flow and its visualization.

For each section, sample plots of the flow coefficient is shown for the different parameters, H/D_H and Re. Graphs of PIV plots, mean velocity, vorticity, turbulent kinetic energy and mean squared vorticity flow fields and TiO_2 surface flow visualization are also provided.

In order to highlight the different properties of the impinging jet, a schematic of the different jet areas of interests are defined. These are listed below, and illustrated in Figure 5.1.

- Region 1: Jet Column Development
- Region 2: Jet Column Impingement
- Region 3: Upper Crossflow
- Region 4: Upstream Surface Vortex Flow
- Region 5: Downstream Flow

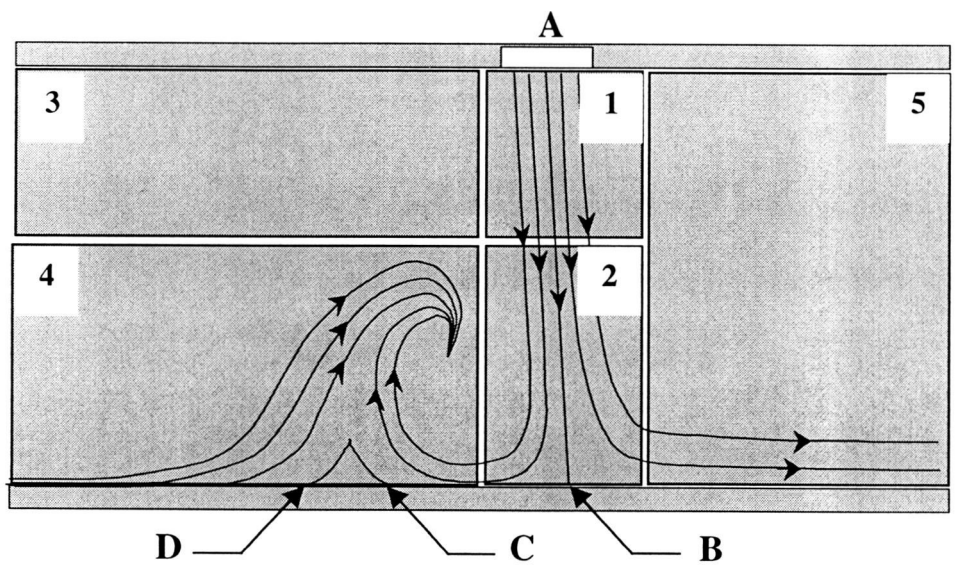

Figure 5.1 Definition of jet regions with four points of interests identified

Four points of interest are defined below and labeled in Figure 5.1:

- A: Jet Exit

- B: Stagnation Point
- C: Surface Vortex Detachment Point
- D: Upstream Flow Detachment Point

The stagnation point, B, will also be referred to as the stagnation area due to the relatively large size of the stagnation flow around B. Therefore, B is defined as the geometric center of the stagnation region. The near-stagnant flow region, close to the surface between C and D, will be referred to as the "surface vortex stagnation" region.

Flow Structure versus Downstream Position

In this section, the flow structure and the influence of the crossflow on the jets are described for both the circular and the cusped ellipse (0°) jet array for the following conditions: higher impingement distance (H/D_H=4) and the same low flow rate Q_R=14CFM. The corresponding Reynolds number are Re=9,740 for the circular jet array and Re=8,570 for the cusped ellipse (0°) jet array. The cusped ellipse (90°) jet array is described separately due to its unique flow-field, in the forth section of this chapter.

In Figure 5.2, the variation of the flow coefficient, C_D, is plotted as a function of downstream distance labeled with the corresponding crossflow-to-jet

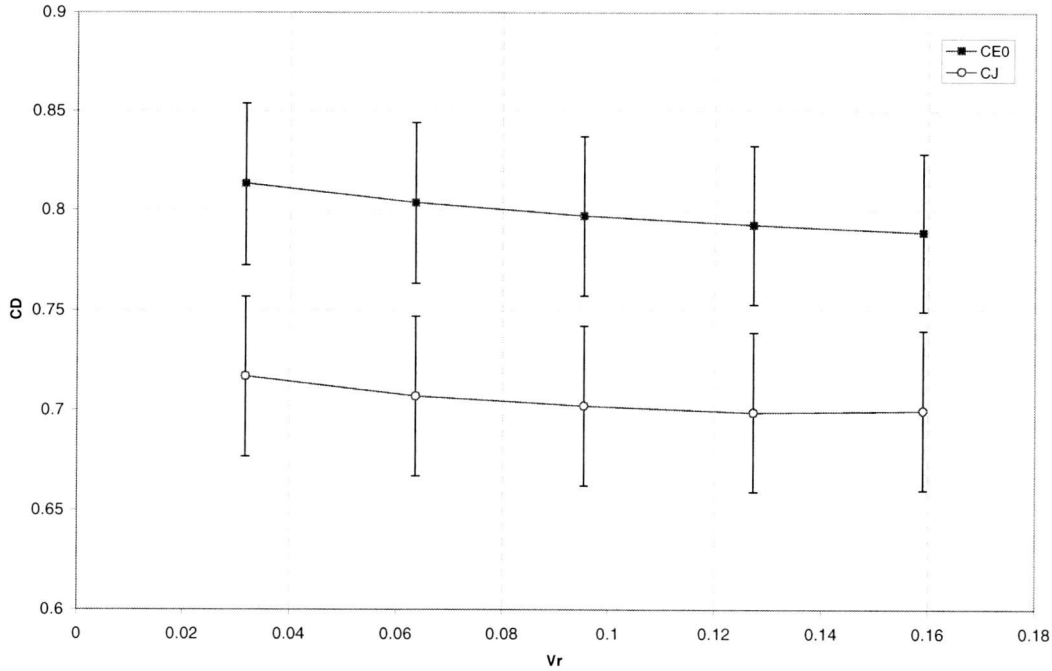

Figure 5.2. Flow coefficient, H/D_H=4, Flow rate Q_R=14CFM,
Circular jet: Re=9,740, Cusped ellipse (0°) jet: Re=8,570

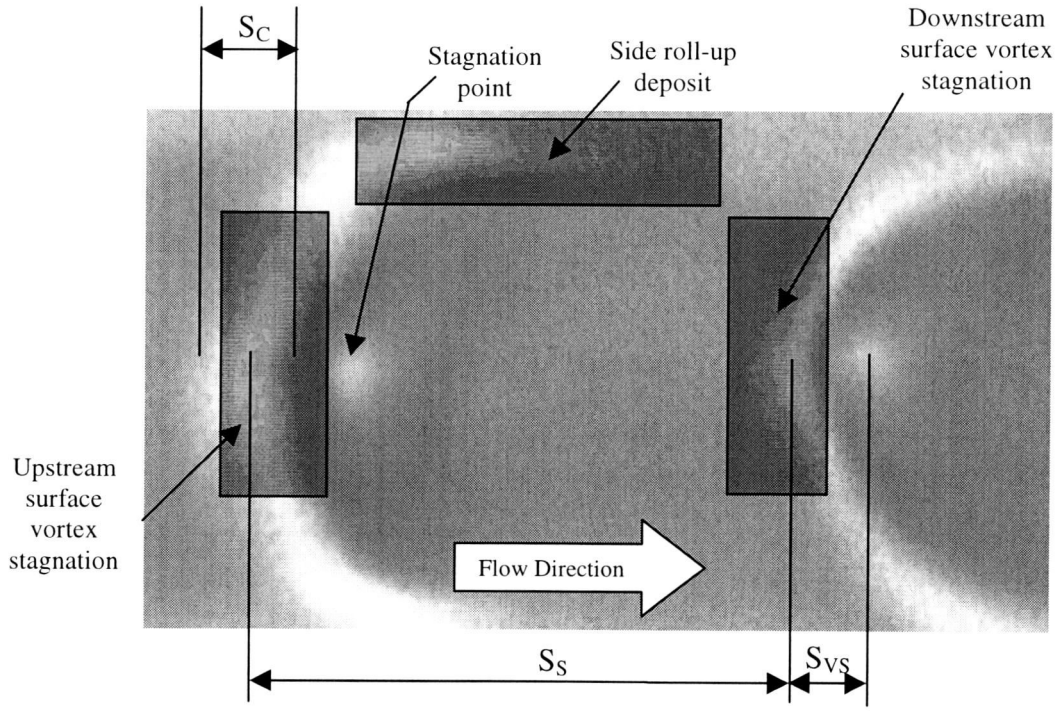

Figure 5.3. Close-up of the flow visualization by surface deposition illustrating the relative dimensions of the surface vortex and stagnation point.

velocity ratio, V_r, which was determined to be the best variable to describe the downstream distance. Moving downstream along the impingement surface, the flow coefficient, C_D, decreases slightly and monotonically. The average value, $<C_D>$, is 0.70 for the circular jet array and 0.80 for the cusped ellipse (0°) jet array. For $V_r >$ 0.16, C_D appears to reach a constant value.

The surface flow visualization provides details of what the flow pattern is at the impingement surface. All the jets spread over the surface, creating an array of cells defined by four detachment-reattachment zones with a characteristic "horseshoe" shape around each jet. A close-up of a cell is shown in Figure 5.3. The first zone is due to the upstream collision of the crossflow and the return-flow (upstream surface vortex stagnation). The bands on each side of the jet are due to the roll-up of the jet flow with the two adjacent jets. The downstream zone is caused by the surface vortex detachment, which is a result of the impingement of the flow with the downstream jet. Along the lateral direction (across the flow), the results show a quasi-periodic aspect proving that each row can be considered as a partial symmetry plane. Results shown in Figures 5.4 and 5.5 show the typical patterns for the circular and the cusped ellipse (0°) jet array, respectively.

Moving downstream from the back to the exit where the crossflow ratio is increasing, it can be observed that the "horseshoe" shapes of the cells become increasingly more oblong in shape. For jets closer to the back wall, the impingement point is located at the center of the cell, but further downstream, this center appears to shift slightly upstream of the center of the cell. Figure 5.6 shows

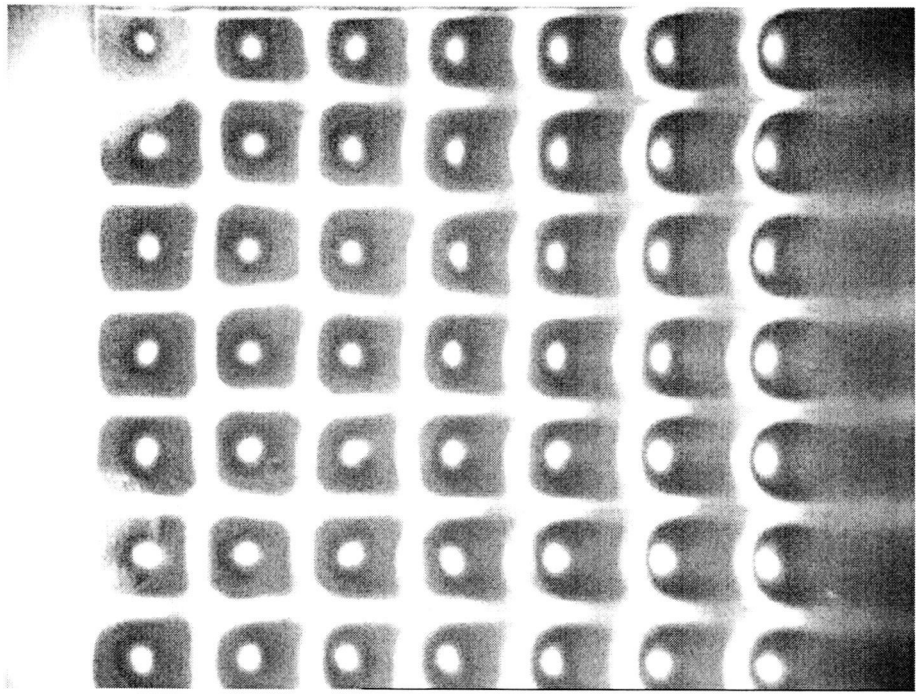

Figure 5.4. Surface Flow Visualization, Circular jet,
H/D_H=4, Q_R=14CFM, Re=9,740

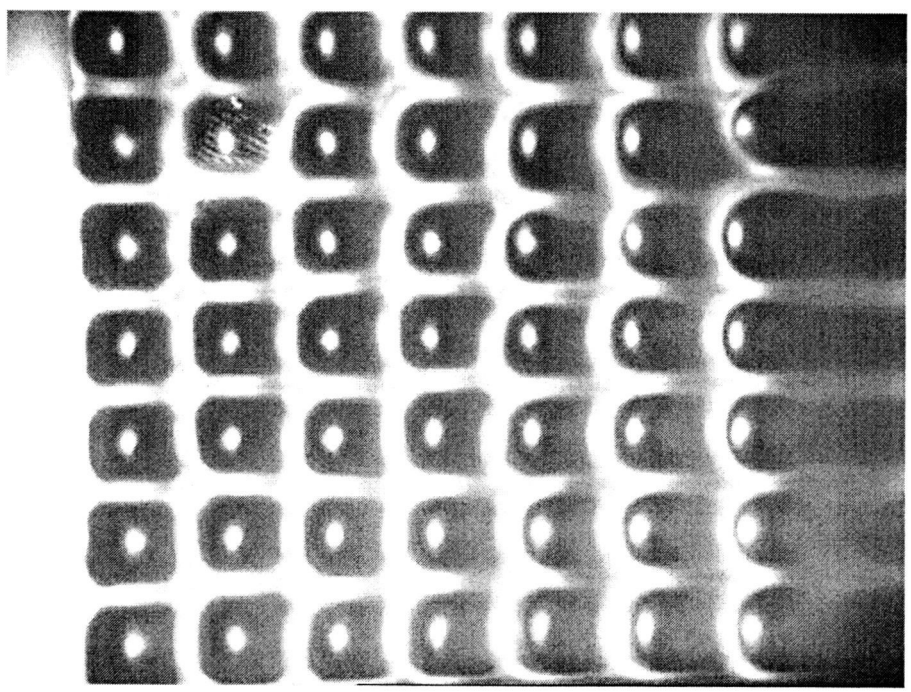

Figure 5.5. Surface Flow Visualization, Cusped ellipse (0°) jet,
H/D_H=4, Q_R=14CFM, Re=8,568

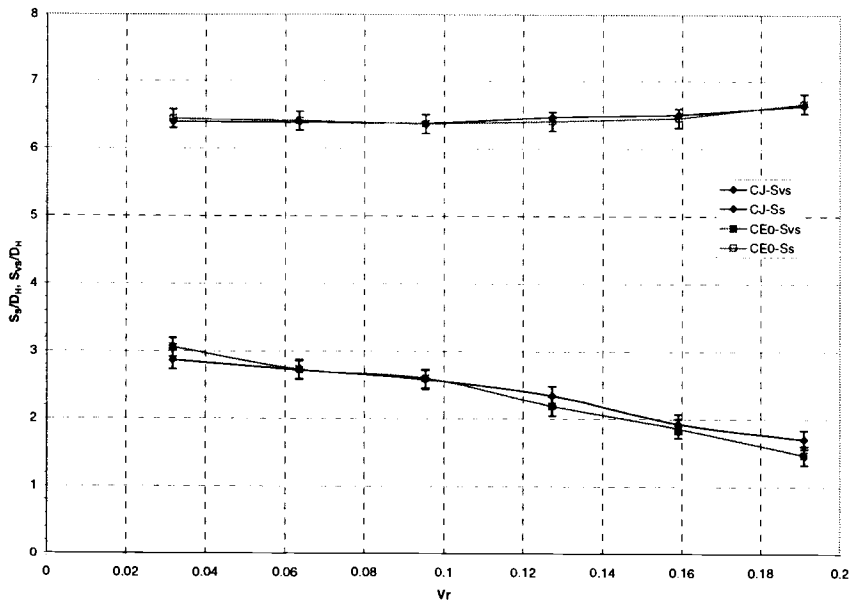

Figure 5.6. Surface vortex and Stagnation point relative location, H/D_H=4, Q_R=14CFM, Circular jet: Re=9,740, Cusped ellipse (0°) jet: Re=8,570

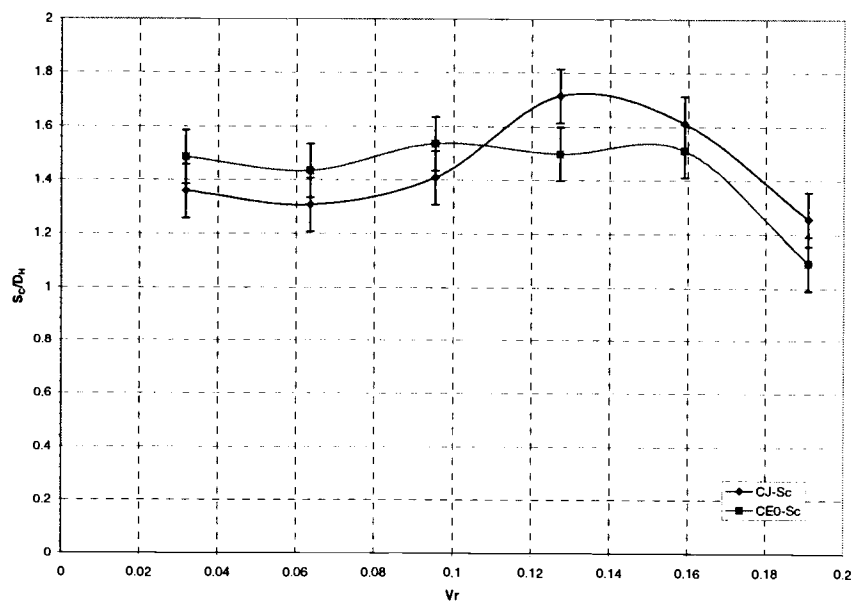

Figure 5.7. Surface vortex deposit size, H/D_H=4, Q_R=14CFM, Circular jet: Re=9,740, Cusped ellipse (0°) jet: Re=8,570

the evolution of S_{VS} and S_S (which are defined in Figure 5.3) along the flow for the circular and the cusped ellipse (0°) jet array. Both configurations show similar results: a very small increase (<5%) in the surface vortex separation distance, S_S, indicates that the cell size is not changing significantly along the downstream direction while a 50% decrease in S_{VS} is observed. Because the cell size is relatively unchanged, it is concluded that it is not the center that is shifting, but the upstream and downstream cell boundaries. As the crossflow-to-jet ratio increase, the boundaries are progressively shifted downstream. This indicates that S_{VS} decreases along the flow direction such that the distance from the upstream boundary to the stagnation point decreases due to the downstream movement of the surface vortex stagnation region. Figure 5.7 shows the evolution of the surface vortex stagnation size, S_C, along the downstream flow. For the cusped ellipse (0°) jet array, S_C doesn't appear to be very sensitive to the crossflow except near the exit, where there is a 27% drop. However, for the circular jet array, there is a greater sensitivity in the region closer to the exit (25% increase followed by an equivalent drop), as the crossflow velocity ratio increases.

For jet 2, close to the back wall, the impingement point is localized at the center of the cell. At this location, the crossflow-to-jet velocity ratio, V_r, is 0.032. The mean velocity vector field plot for both the circular and the cusped ellipse (0°) jet 2, are shown in Figures 5.8 and 5.9, respectively. From these PIV plots, the upper part of the flow [region 3] appears nearly stationary. The jet column [region 1] breaks into a downstream flow [region 5] and a relatively weak return-flow

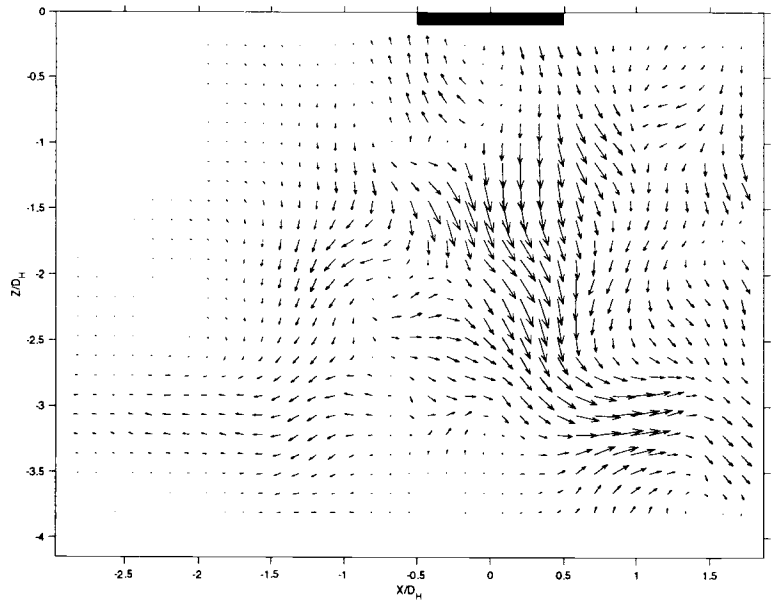

Figure 5.8. PIV, Circular jet, H/D_H=4, Jet 2, Vr=0.032, Re=9,740

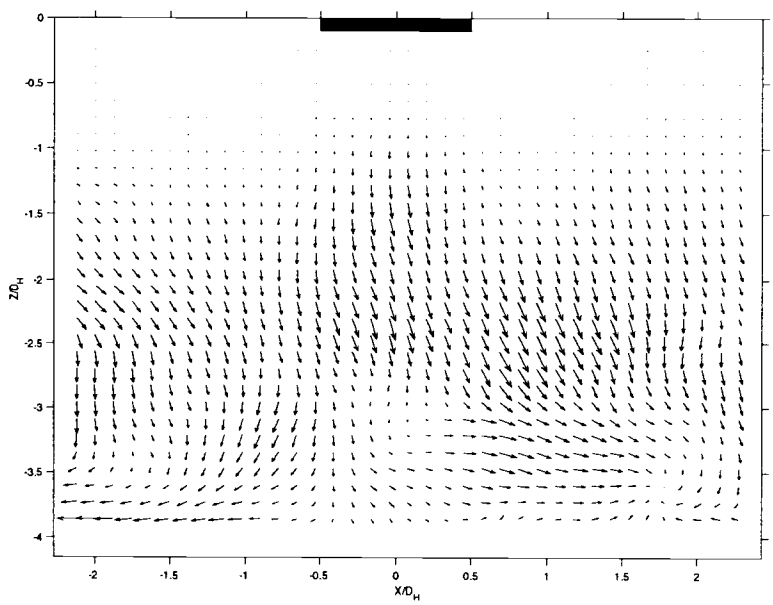

Figure 5.9. PIV, Cusped ellipse (0°) jet, H/D_H=4, Vr=0.032, Re=8,570

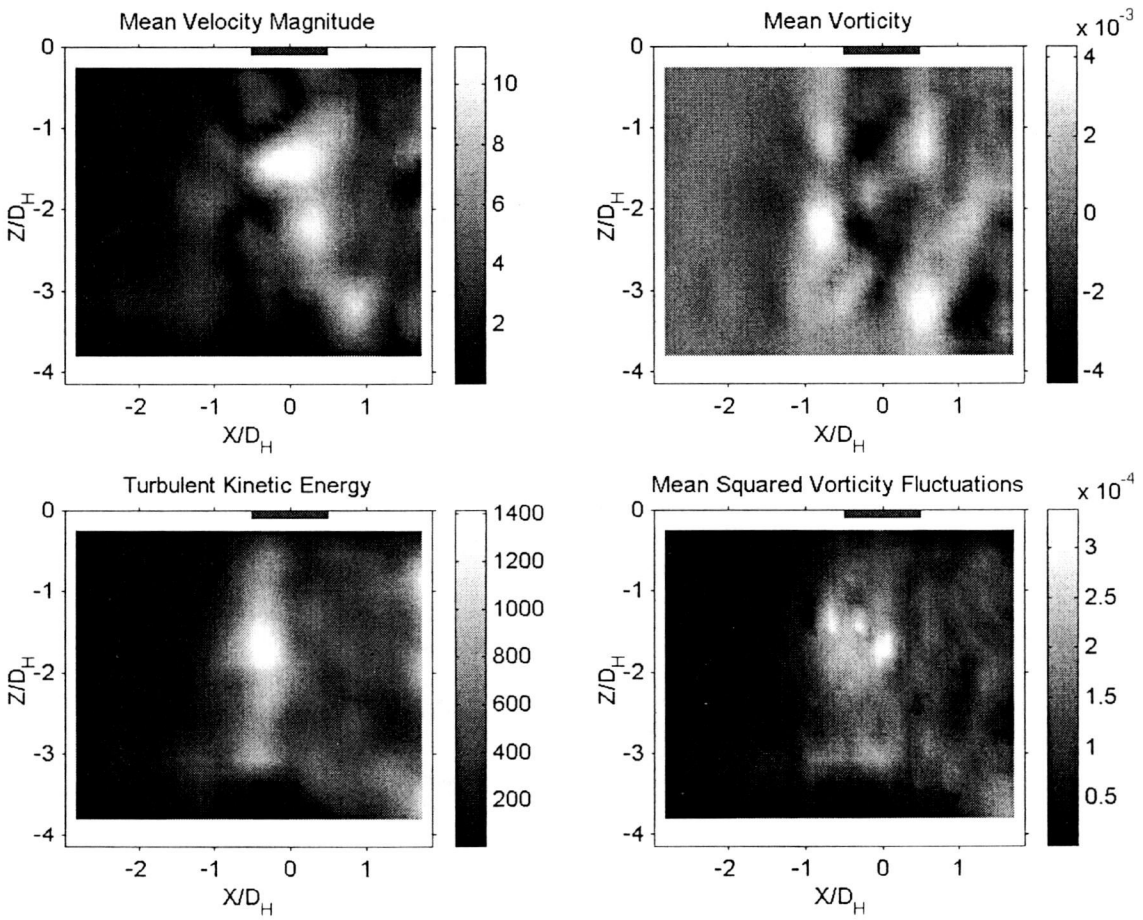

Figure 5.10. Flow characteristics, Circular jet,
H/D_H=4, Vr=0.032, Re=9,740

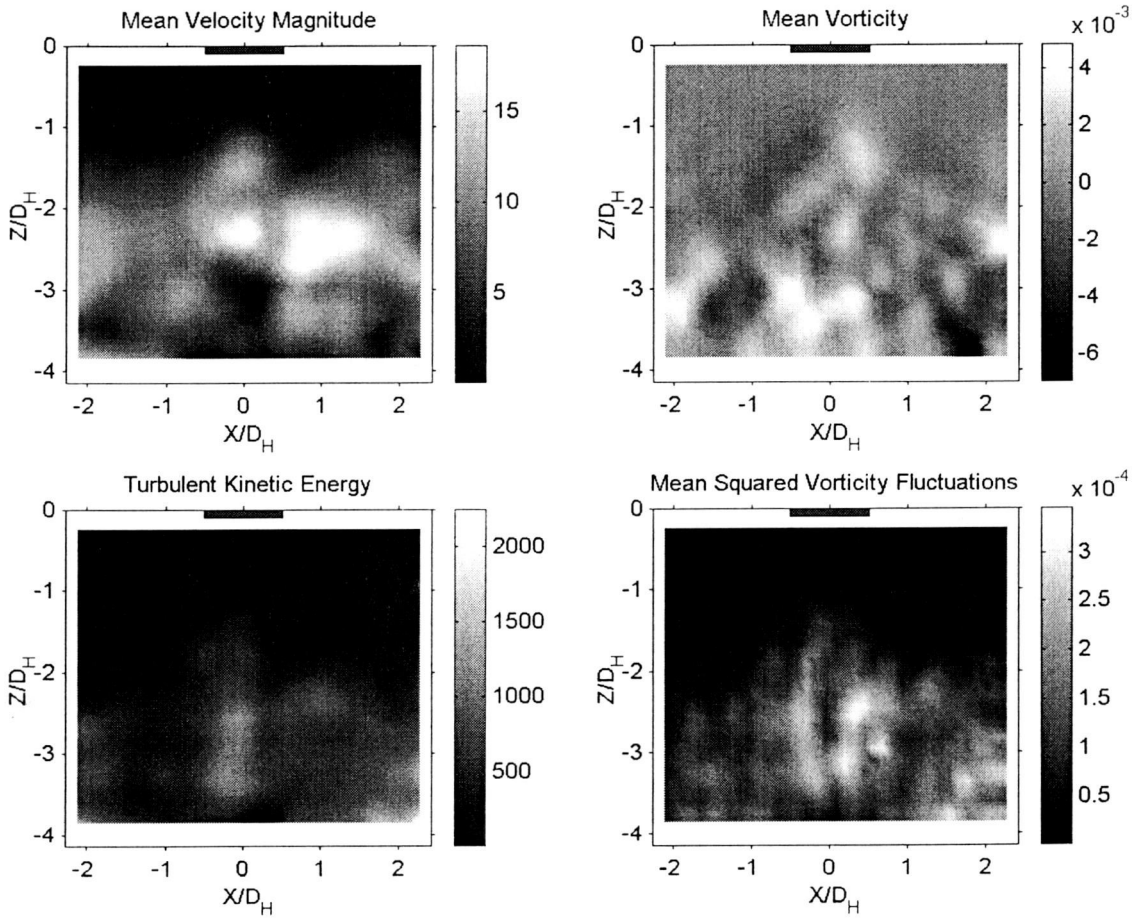

Figure 5.11. Flow characteristics, Cusped ellipse (0°) jet,
Vr=0.032, H/D_H=4, Re=8,570

[region 4] at $1D_H$ from the impingement surface. This return-flow and the flow coming from the upstream jets appear to generate a large scale rolling structure with its center of rotation outside of the field of view ($X/D_H>2$). This structure is more pronounced and therefore stronger for the cusped ellipse (0°) jet 2. This rolling structure is defined as a "surface vortex". The stagnation point region, B, is very well defined for the cusped ellipse (0°) jet 2 but very scattered for the circular jet 2. The flow downstream of the jet column [region 5] is vertically entrained flow, progressively turning into a parallel flow along the impingement surface. For both geometries, this parallel flow region is about $1D_H$ thick. The flow characteristics for this jet location are shown in Figures 5.10 and 5.11. The jet is particularly well defined for the circular jet 2 with a high-speed core generating pairs of counter-rotating vorticity by shear with the air present in the channel. The cusped ellipse (0°) jet 2 has a slightly faster jet with a better-diffused vorticity field. The turbulent core and the dissipation seem concentrated in the jet column but the average over the flow field shows a 43% increase in both properties, compared to the circular jet.

Further downstream, near the jet array center, at jet 4, the crossflow-to-jet velocity ratio is $V_r=0.095$. Figures 5.12 and 5.13 show the mean velocity vector field plot for the circular and the cusped ellipse (0°) jet 4. For both configurations, the jet column [region 1] separates into a downstream flow and a return flow at $1D_H$ from the impingement surface [region 2]. The return flow collides with the upstream jet flow and creates a surface vortex in region 4 that is stronger than at the upstream location, jet 2. For the circular jet, the center of rotation of the surface

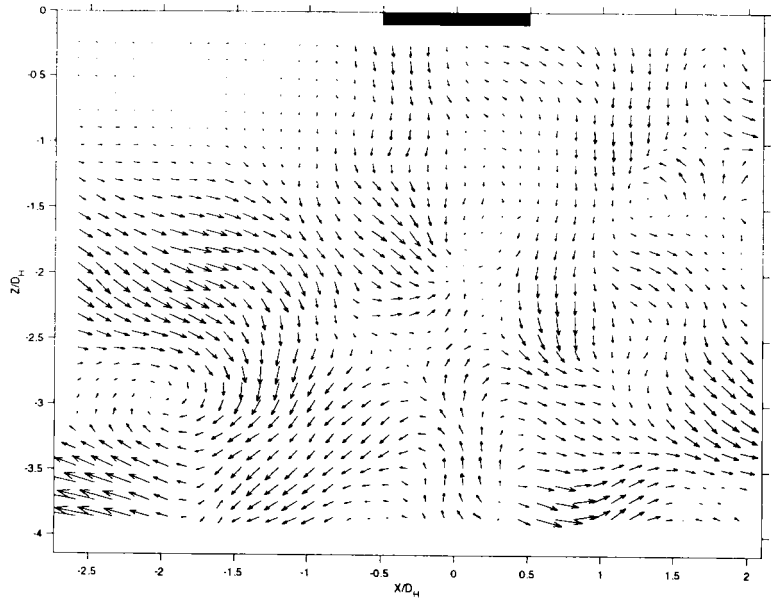

Figure 5.12. PIV, Circular jet, H/D_H=4, Vr=0.095, Re=9,740

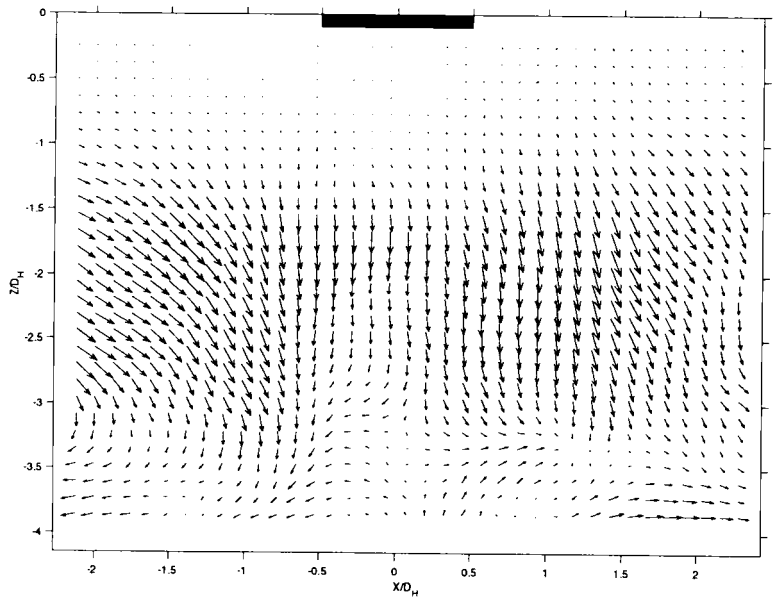

Figure 5.13. PIV, Cusped ellipse (0°) jet, H/D_H=4, Vr=0.095, Re=8,570

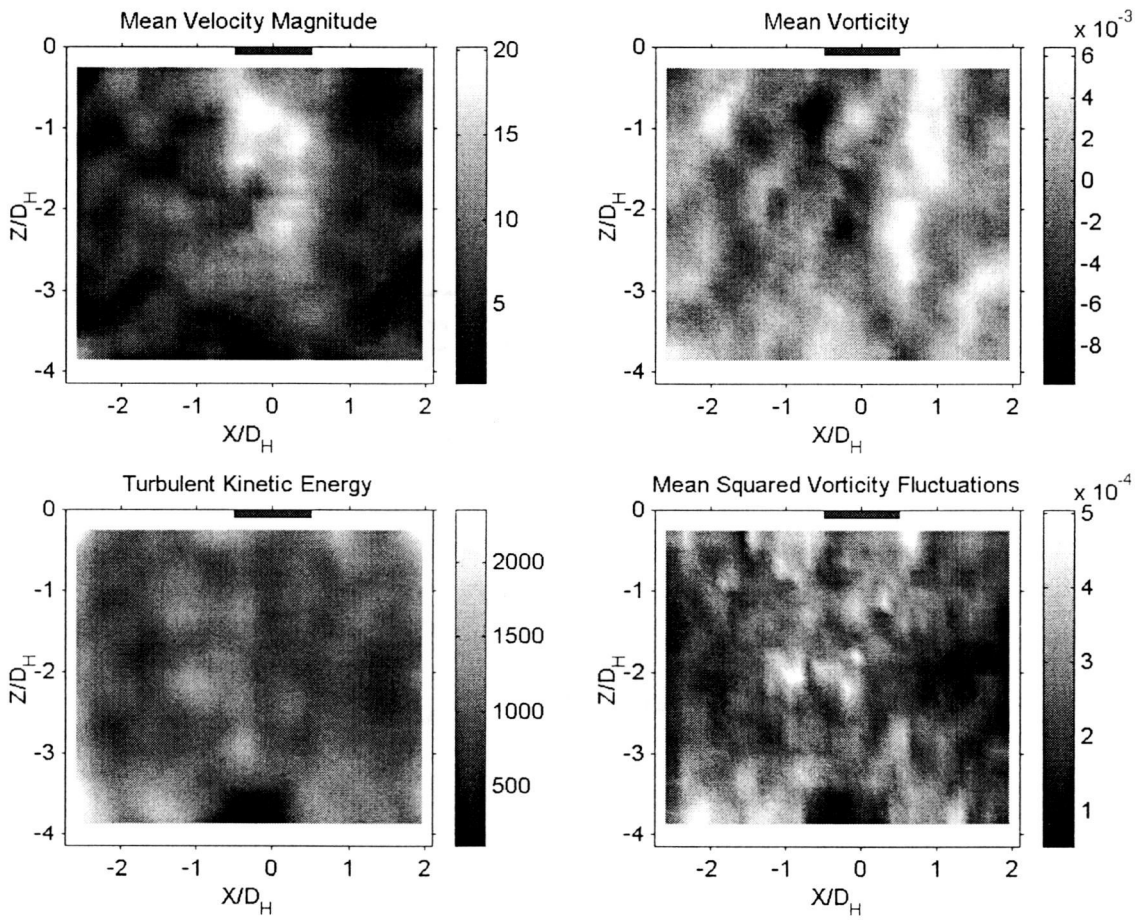

Figure 5.14. Flow characteristics, Circular jet,
H/D_H=4, Vr=0.095, Re=9,740

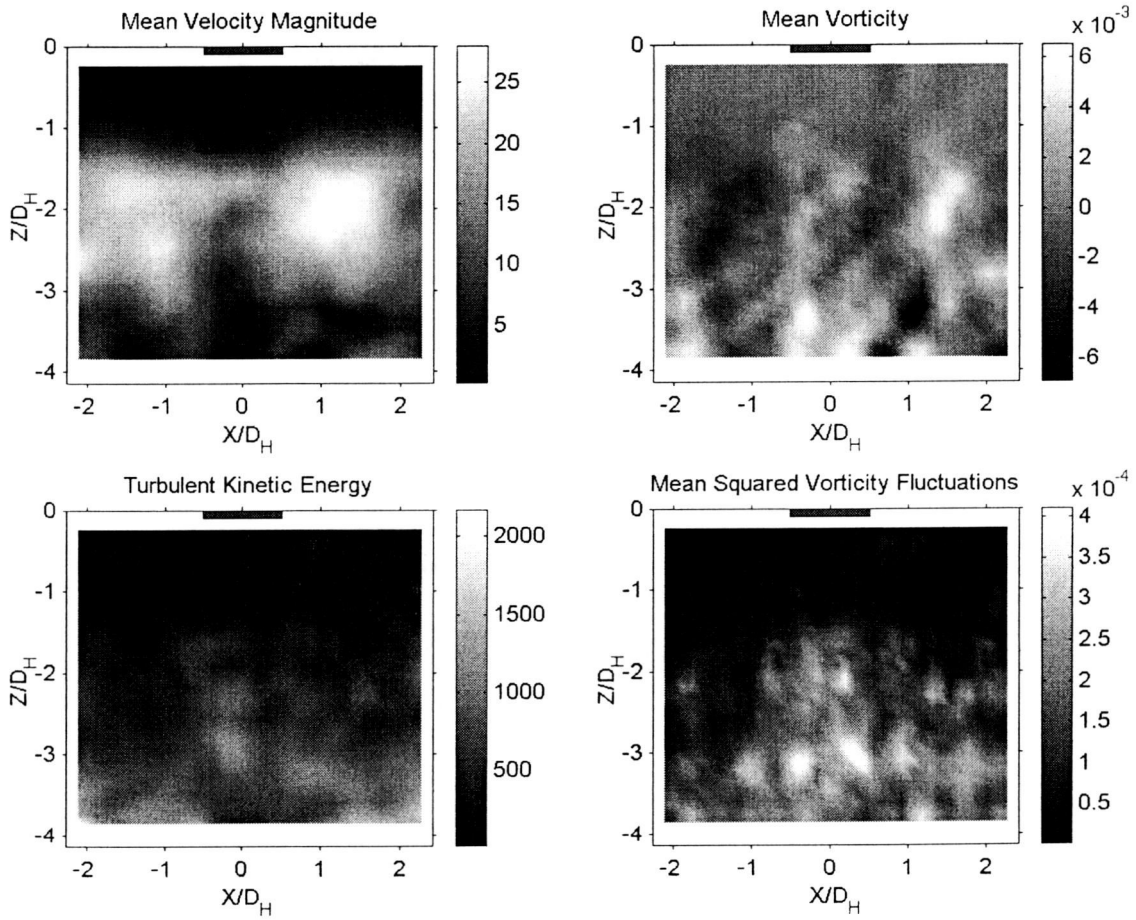

Figure 5.15. Flow characteristics, Cusped ellipse (0°) jet,
H/D_H=4, Vr=0.095, Re=8,570

vortex comes into the field of view and is at $1.8D_H$ from the impingement point. For the cusped ellipse (0°) jet, the center of rotation is still outside of the field of view but the rotation speed is faster than for the circular jet. The flow downstream of the jet column [region 5] shows a vertically entrained flow, progressively turning into a parallel flow along the surface. It is important to note that for the circular jet, the downstream flow is slightly disturbed by some independent structures in the flow. Also, not that for the cusped ellipse (0°) jet , the top part of the flow field is very weak. This phenomenon will be explained by the side wall effect discussed in last section of this chapter. The flow characteristics for this jet are shown in Figures 5.14 and 5.15. For the circular jet, the shearing within the jet increases in intensity while spreading over the impingement surface. The turbulent kinetic energy and the dissipation spread over a larger portion of the channel increasing the average vorticity by 160% compared to jet 2. Similar results are obtained for the cusped ellipse (0°) jet but the increase is smaller, only 16% higher than jet 2.

Further downstream, at jet 6, the crossflow-to-jet velocity ratio is V_r=0.159. The mean velocity vector field plot for the circular jet and the cusped ellipse (0°) jet are shown in Figures 5.16 and 5.17. For both configurations, a surface vortex is created by the return flow from the impinging jet and the flow coming from the upstream jet in region 4. The center of rotation appears to be at height $Z=1D_H$ from the impingement surface and at distance $X=1D_H$, upstream of the stagnation point. For the circular jet, the surface vortex appears to lean strongly against the jet column, entraining a large mass of flow [region 3] into the jet column. The flow

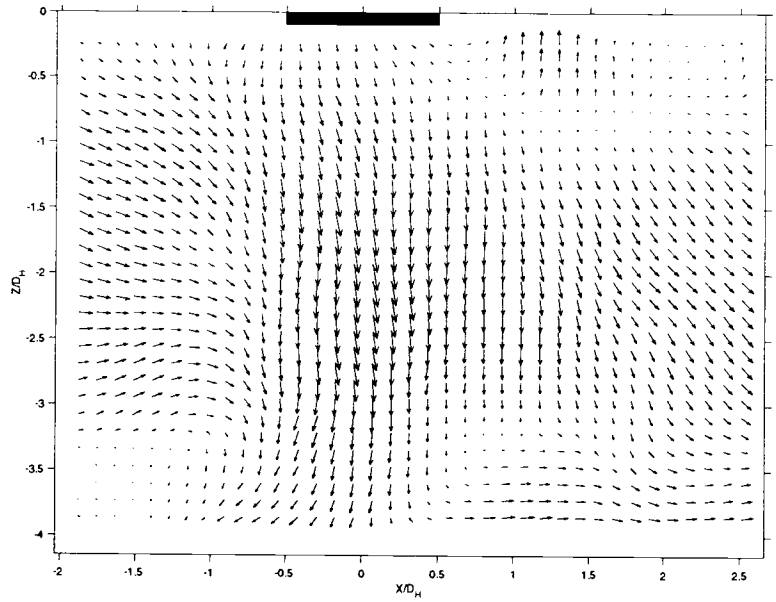

Figure 5.16. PIV, Circular jet, H/D_H=4, Vr=0.159, Re=9,740

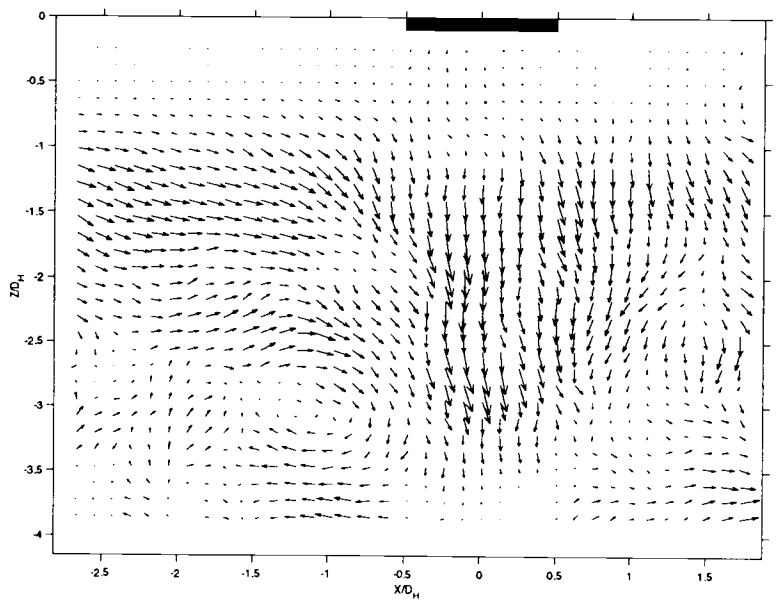

Figure 5.17. PIV, Cusped ellipse (0°) jet, H/D_H=4, Vr=0.159, Re=8,570

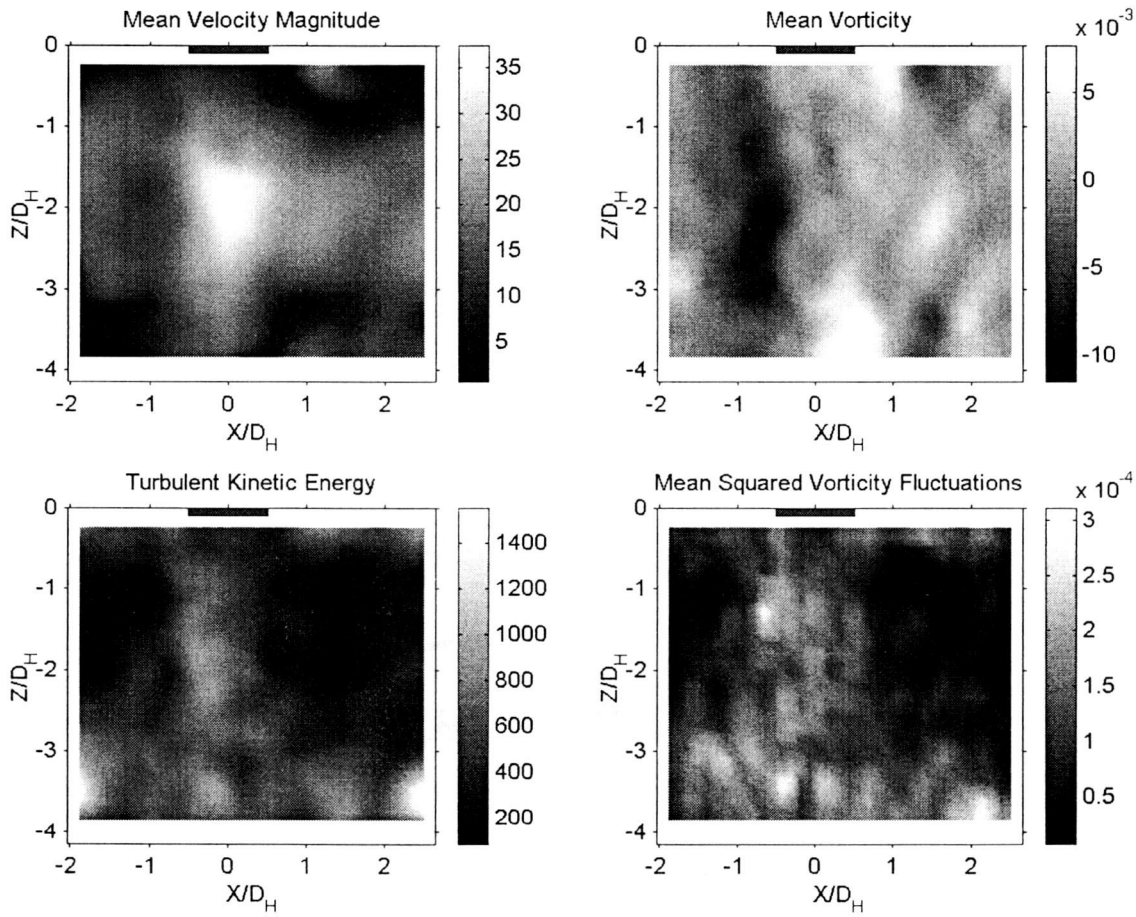

Figure 5.18. Flow characteristics, Circular jet,
H/D_H=4, Vr=0.159, Re=9,740

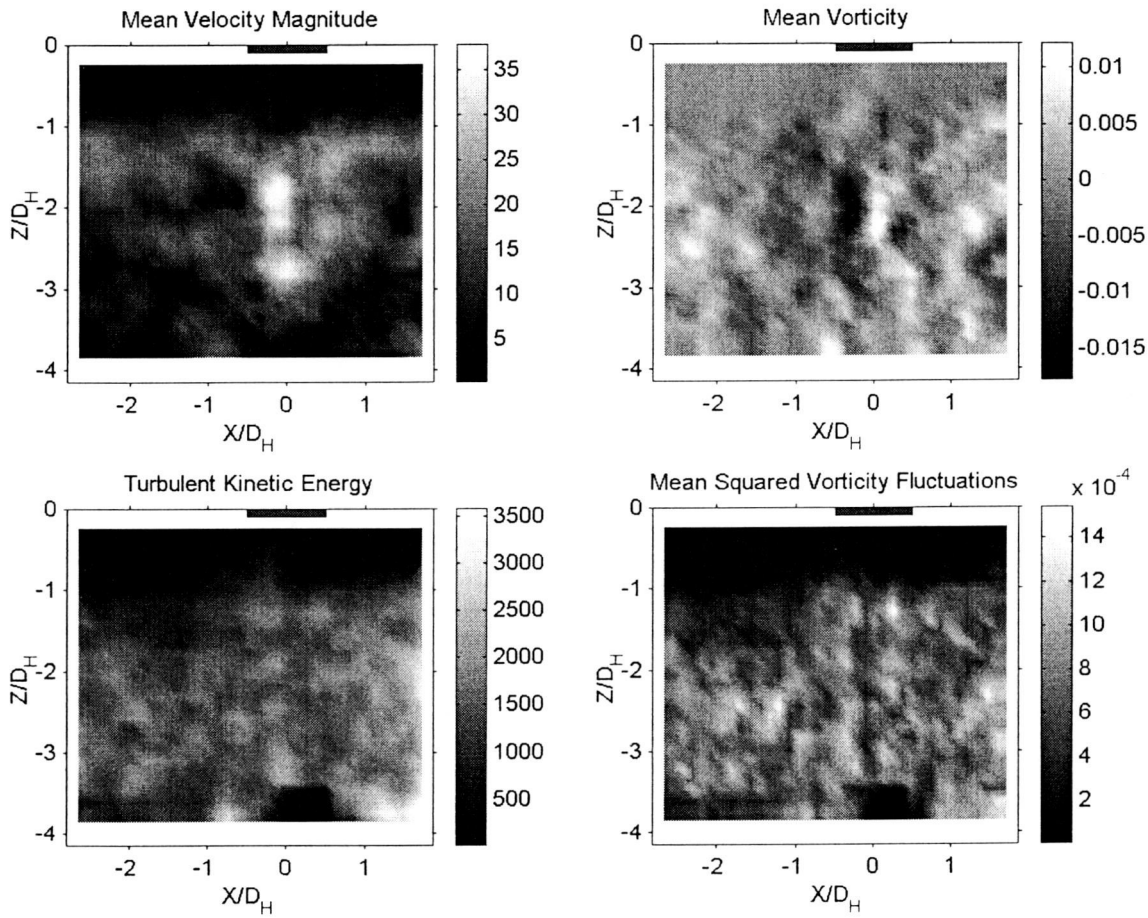

Figure 5.19. Flow characteristics, Cusped ellipse (0°) jet,
H/D_H=4, Vr=0.159, Re=8,570

characteristics for this jet location are shown in Figures 5.18 and 5.19. The pair of counter-rotating vorticity appears to be broken and is biased in the downstream direction. The TKE appears to be concentrated in the jet column and spread relatively uniformly over the impingement surface creating "pockets" of concentrated TKE. For the cusped ellipse (0°) jet, the surface vortex appears to be slightly larger in size. Multiple vorticity pockets appears all over the flow while the jet shearing layers appears locally reduced. Both TKE creation and dissipation occurs all over the channel with levels of TKE 2 times greater than for the circular jet and mean squared vorticity levels 5 times greater than for the circular jet.

Effect of the Reynolds Number

In this section, the influence of Re on the flow is described at two locations: close to the back of the jet array and close to the exit, at jet 2 and jet 6 locations, respectively. The flow structures for the circular jet array and the cusped ellipse jet array (0°) are analyzed for the following conditions: the higher impingement distance ($H/D_H=4$) and with the flow rate ranging from 14 to 20 CFM, resulting in a wide range of Reynolds number values. For the circular jet, the Re range is $9{,}740<Re<15{,}830$ while for the cusped ellipse (0°) jet, the Re range is $8{,}570<Re<13{,}530$. For each jet along the flow, the crossflow-to-jet velocity ratio is unchanged with Re variations, since it is solely a function of the geometry.

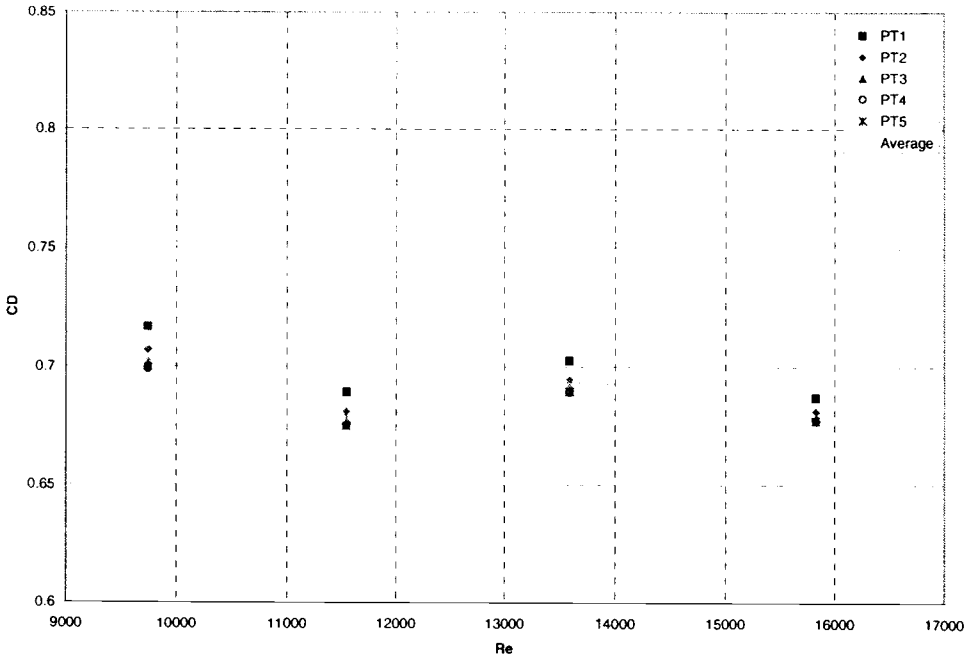

Figure 5.20. Flow coefficient, Circular jet, $H/D_H=4$

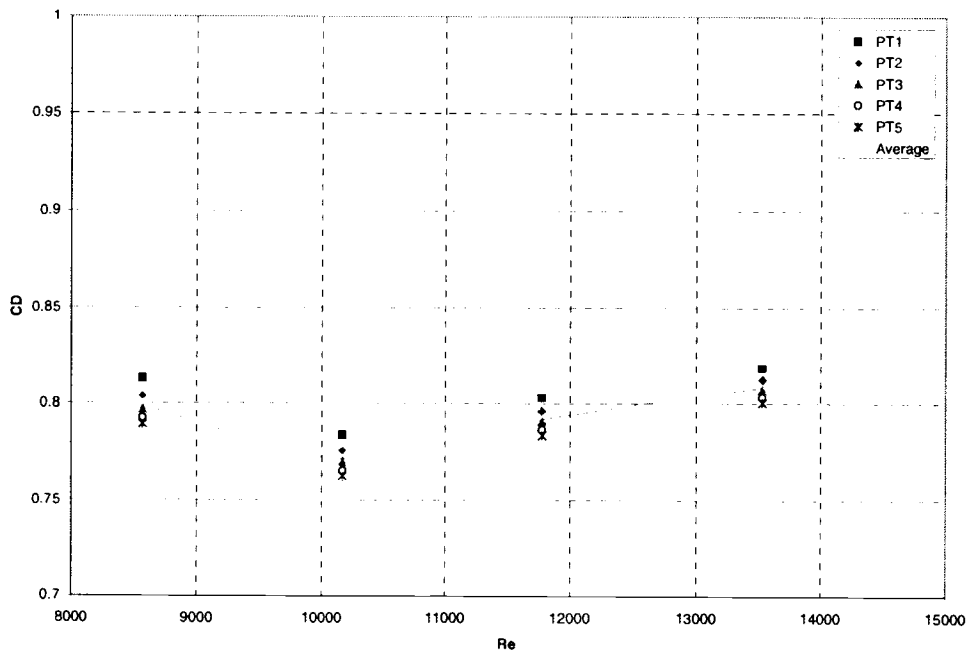

Figure 5.21. Flow coefficient, Cusped ellipse (0°) jet, $H/D_H=4$

Figures 5.20 and 5.21 show the evolution of the flow coefficient versus increasing Re. On these graphs, the flow coefficient values are plotted for the different pressure taps as a function of Re and the corresponding average values, $<C_D>$. For the lower Re, $<C_D>$ is about 0.70 for the circular jet and 0.80 for the cusped ellipse (0°) jet. For the circular jet, $<C_D>$ fluctuations of ±4% are observed over the range of Re, but no clear pattern is detected. For the cusped ellipse (0°) jet, $<C_D>$ first decreases by 3.5%, then continues to increase until the maximum Re is reached. For this maximum value of Re, $<C_D>$ is only 1% higher than for the lowest Re and still decreases monotonically along the crossflow with the same slope as in Figure 5.2.

Figures 5.22 and 5.23 show the surface flow visualization for the maximum Re condition. Compared to the lower Re (see Figures 5.4 and 5.5), no major difference in the flow pattern are perceptible. Figure 5.24 shows the change of S_{VS} and S_S along the flow for the circular and the cusped ellipse (0°) jet arrays. Compared to Figure 5.6, the surface vortex to stagnation point distance, S_{VS}, decreases along the downstream flow with equivalent values and corresponding slope for both lower and higher Re. The surface vortex separation distance, S_S, increases slightly along the downstream direction, but by less than 6%. Figure 5.25 shows the change of the surface vortex stagnation size, S_C, along the flow. For both configurations, S_C doesn't appear to be very sensitive to the crossflow up to the jet array center. Further downstream (near jet 4), Sc appears to increase by nearly 20%, until the exit location where a significant drop is observed.

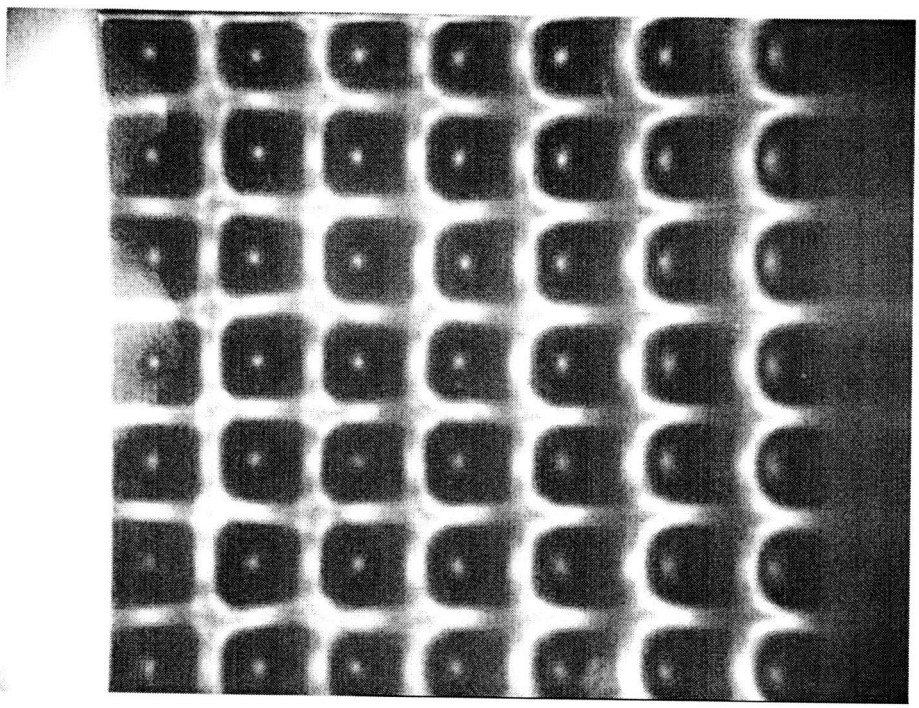

Figure 5.22. Surface flow visualization, Circular jet, $H/D_H=4$, $Q_R=20CFM$, Re=15,800

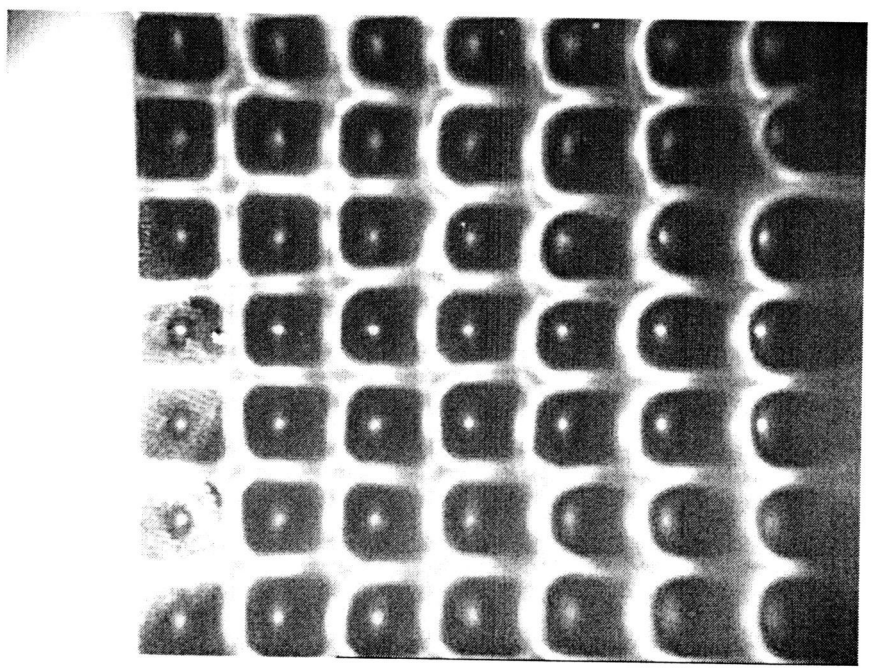

Figure 5.23. Flow coefficient, Cusped Ellipse (0°) jet, $H/D_H=4$, $Q_R=20CFM$, Re=13,500

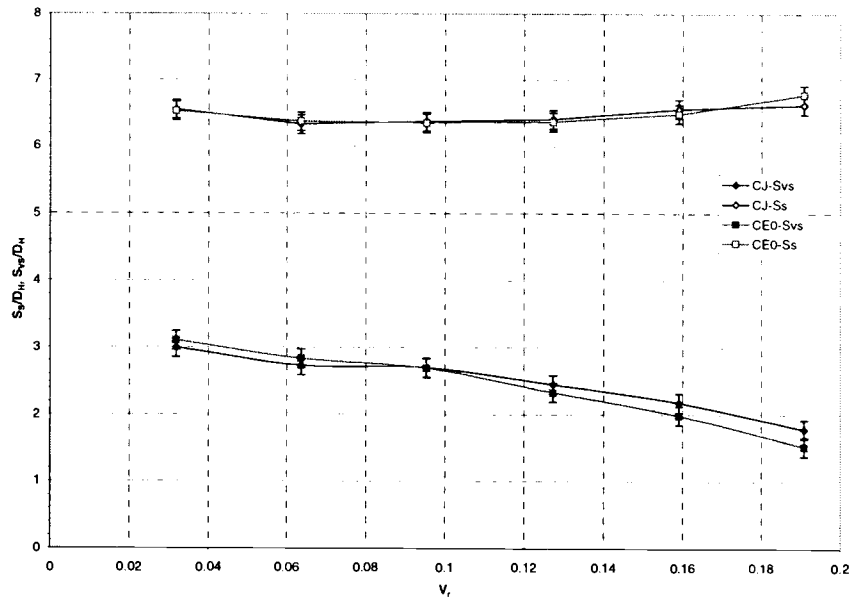

Figure 5.24. Surface vortex and stagnation point relative location, H/D_H=4, Q_R=20CFM, Circular jet: Re=15,800, Cusped ellipse (0°) jet: Re=13,500

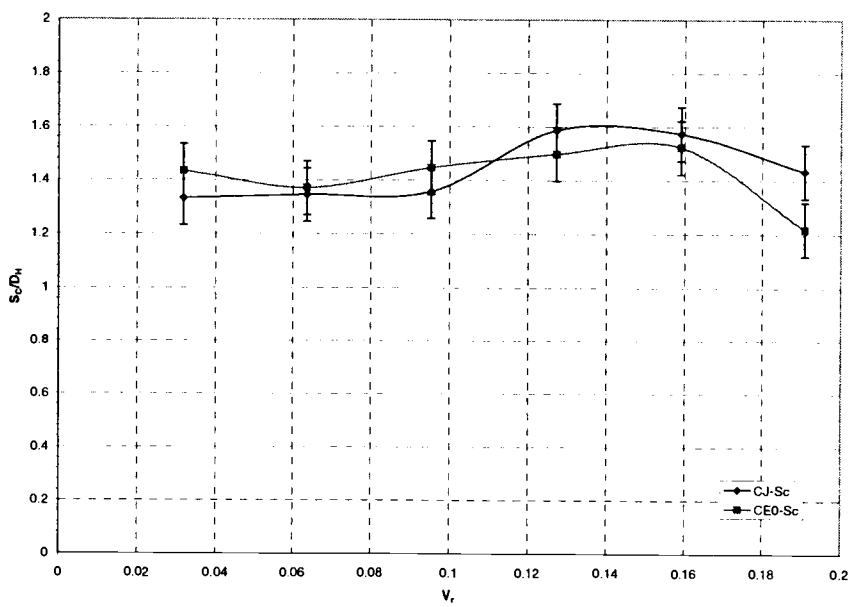

Figure 5.25. Surface vortex deposit size, H/D_H=4, Q_R=20CFM, Circular jet: Re=15,800, Cusped ellipse (0°) jet: Re=13,500

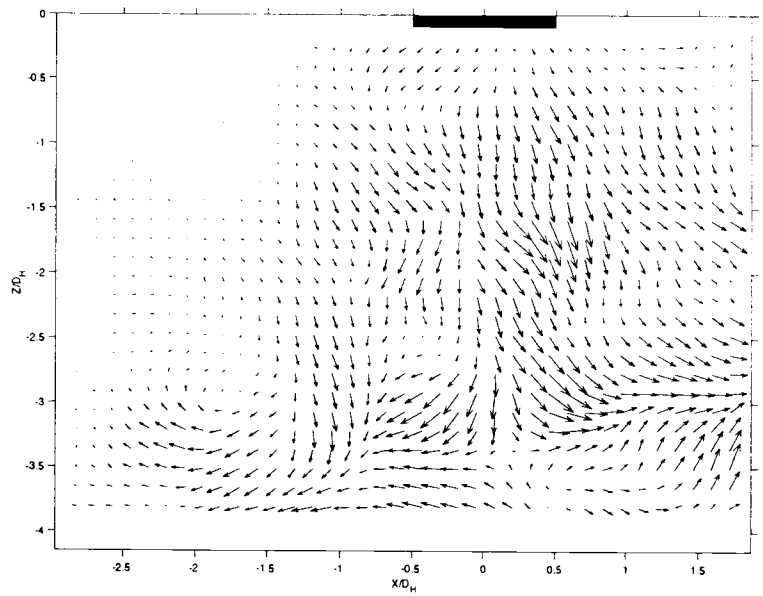

Figure 5.26. PIV, Circular jet, H/D_H=4, Vr=0.032, Re=15,800

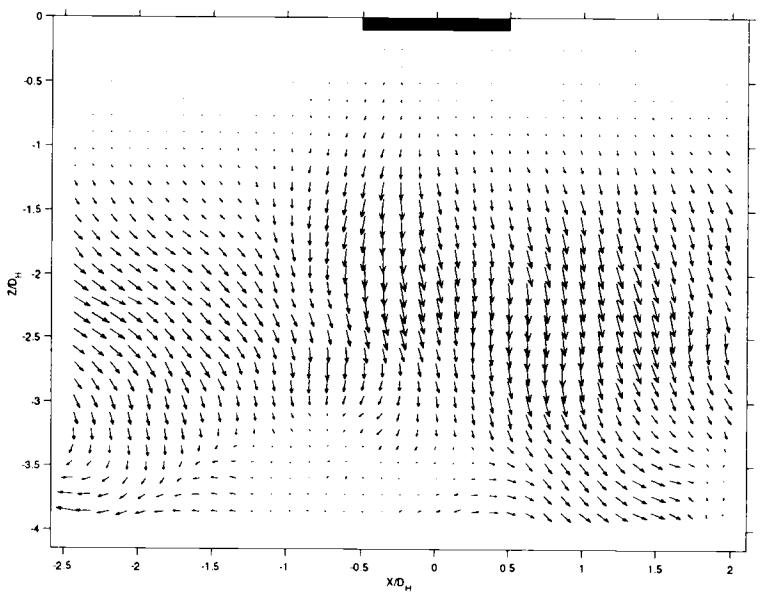

Figure 5.27. PIV, Cusped ellipse (0°) jet, H/D_H=4, Vr=0.032, Re=13,500

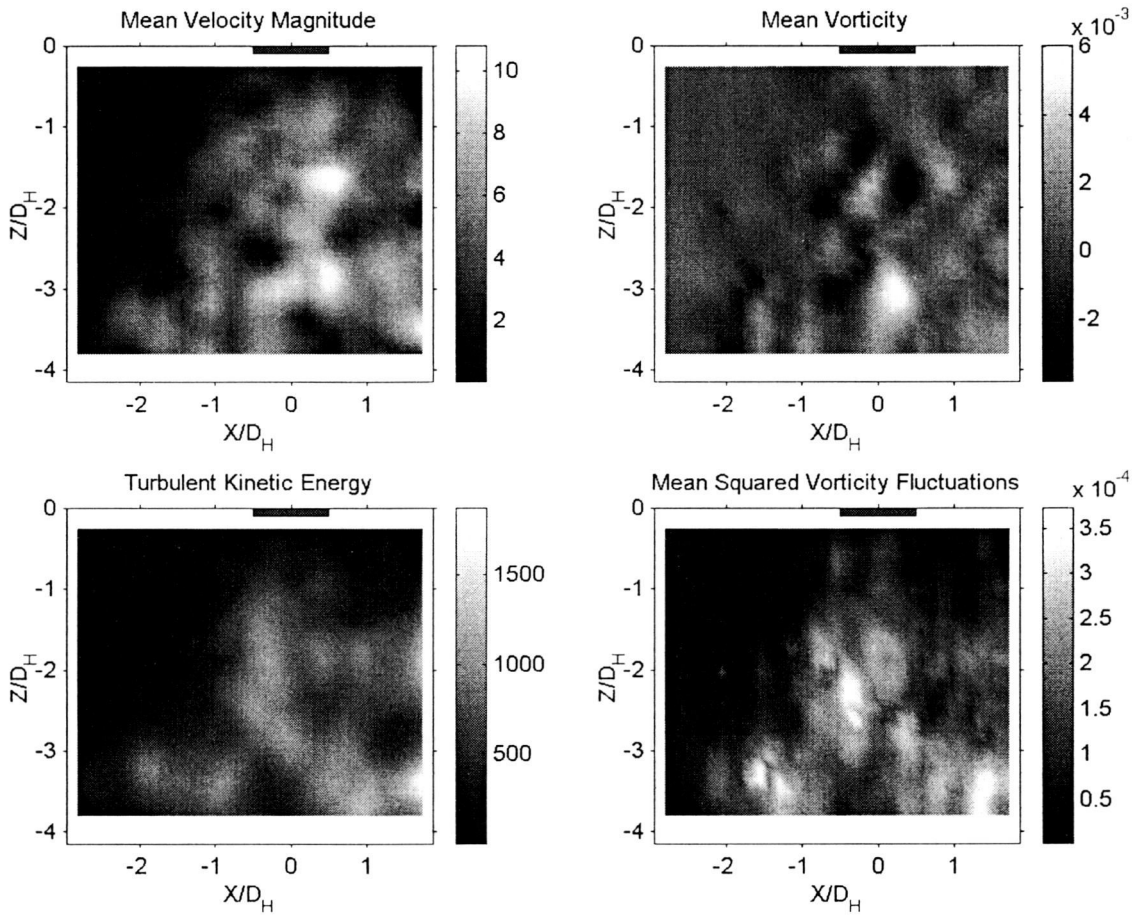

Figure 5.28. Flow characteristics, Circular jet, H/D_H=4, Vr=0.0.32, Re=15,800

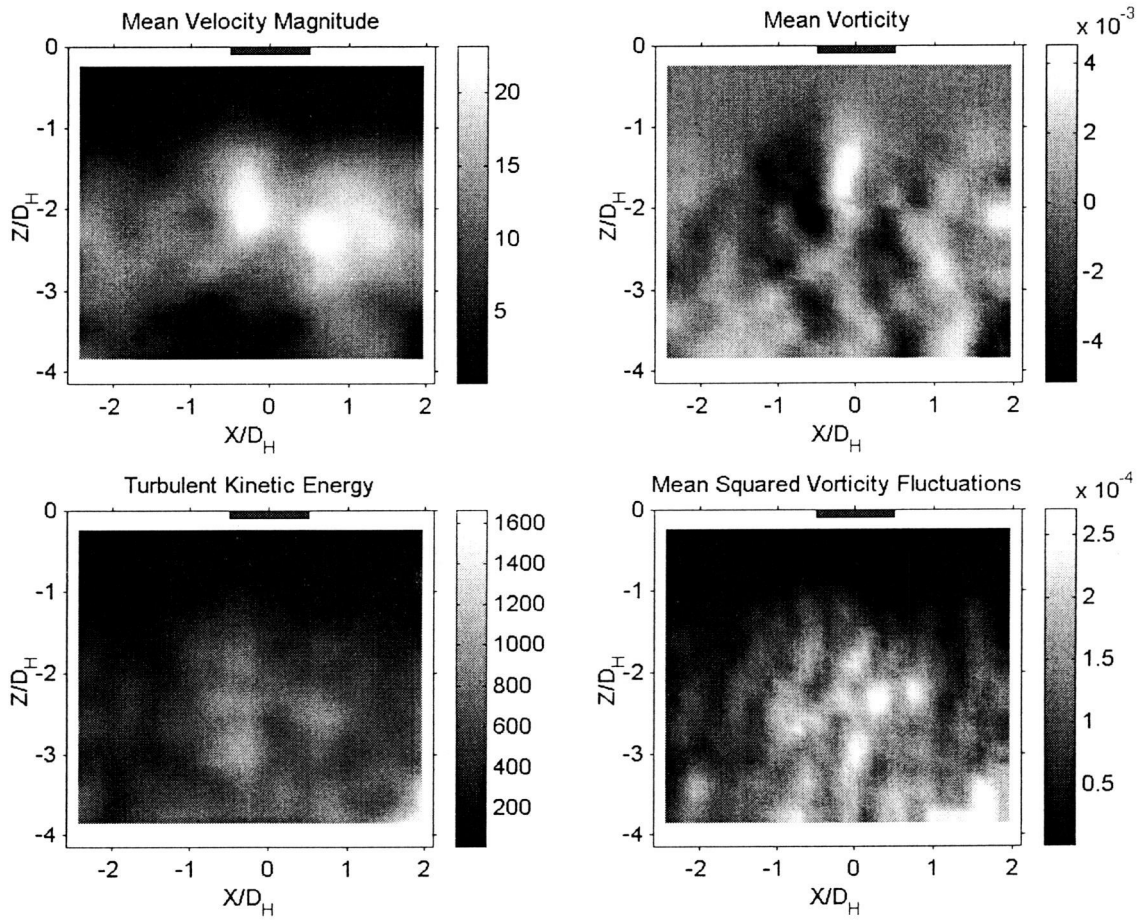

Figure 5.29. Flow characteristics, Cusped ellipse (0°) jet,
H/D_H=4, Vr=0.0.32, Re=13,500

The mean velocity vector field plot for the circular jet and the cusped ellipse (0°) jet are shown in Figures 5.26 and 5.27. Closer to the back of the array, at the jet 2 location where V_r=0.032, the jet structure of the circular jet strengthens slightly for the higher Re. The breakdown of the jet column [region 2] into a parallel flow and a return flow is better defined than for the lower Re. For the circular jet 2, the surface vortex center of rotation location appears to be at $Z=1D_H$ from the impingement surface and its distance to the impingement point is $X=1.7D_H$. The flow characteristics for the circular jet array at this location are shown in Figure 5.28. The vorticity plot indicates that the jet column [region 1] is disturbed about half way down the height of the channel with similar vorticity levels, as for lower Re. The TKE and mean squared vorticity seems to spread further downstream, but also a 54% increase in TKE levels and 61% in mean squared vorticity can be observed compared to the lower Re. As can be seen in Figure 5.27, no major change occurs for the cusped ellipse (0°) jet. The flow characteristics for the cusped ellipse (0°) jet array at this location are shown in Figure 5.29. The surface vortex appears to strengthen slightly but its location and size remain unchanged. The entrainment of the downstream flow appears stronger. The vorticity plots show a better definition of the jet shearing layers and the vorticity levels stay the same. The TKE and mean squared vorticity locations are localized along the jet column and along the impingement surface. Their levels increase slightly by 6% and 9% respectively, when compared to the lower Re (see Figure 5.11).

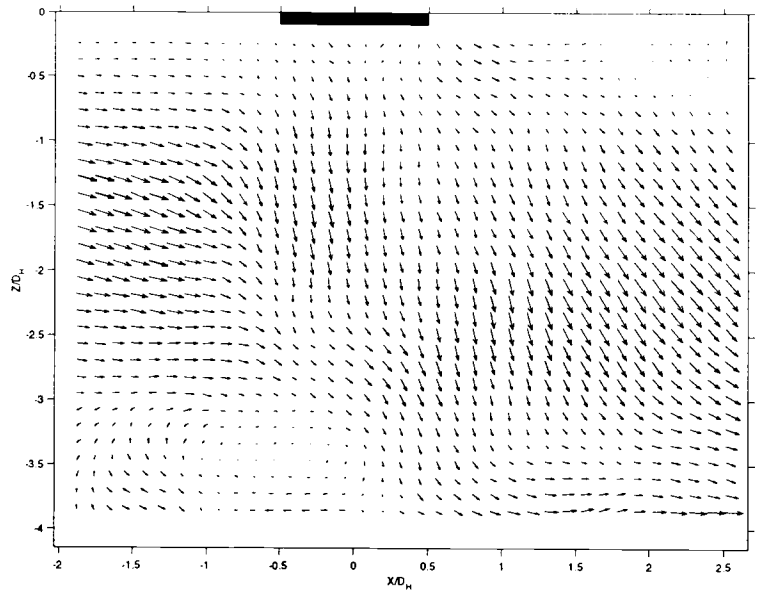

Figure 5.30. PIV, Circular jet, H/D_H=4, Vr=0.159, Re=15,800

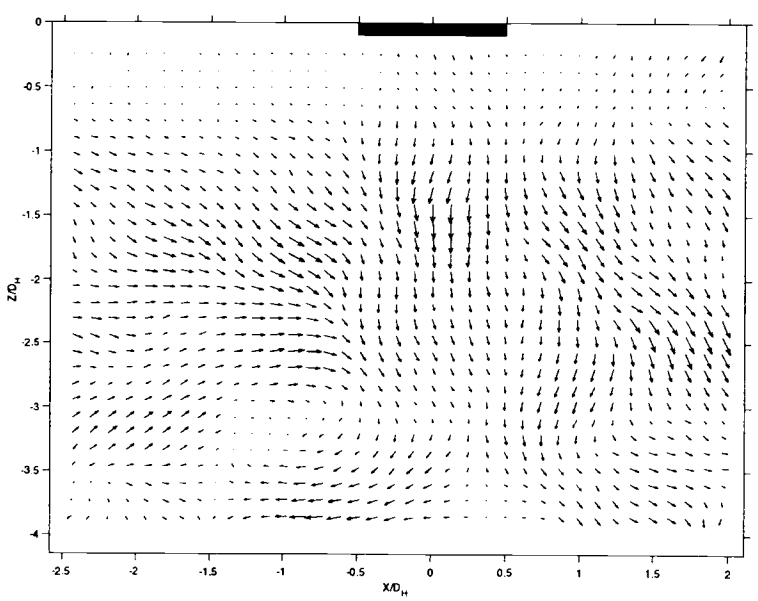

Figure 5.31. PIV, Cusped ellipse (0°) jet, H/D_H=4, Vr=0.159, Re=13,500

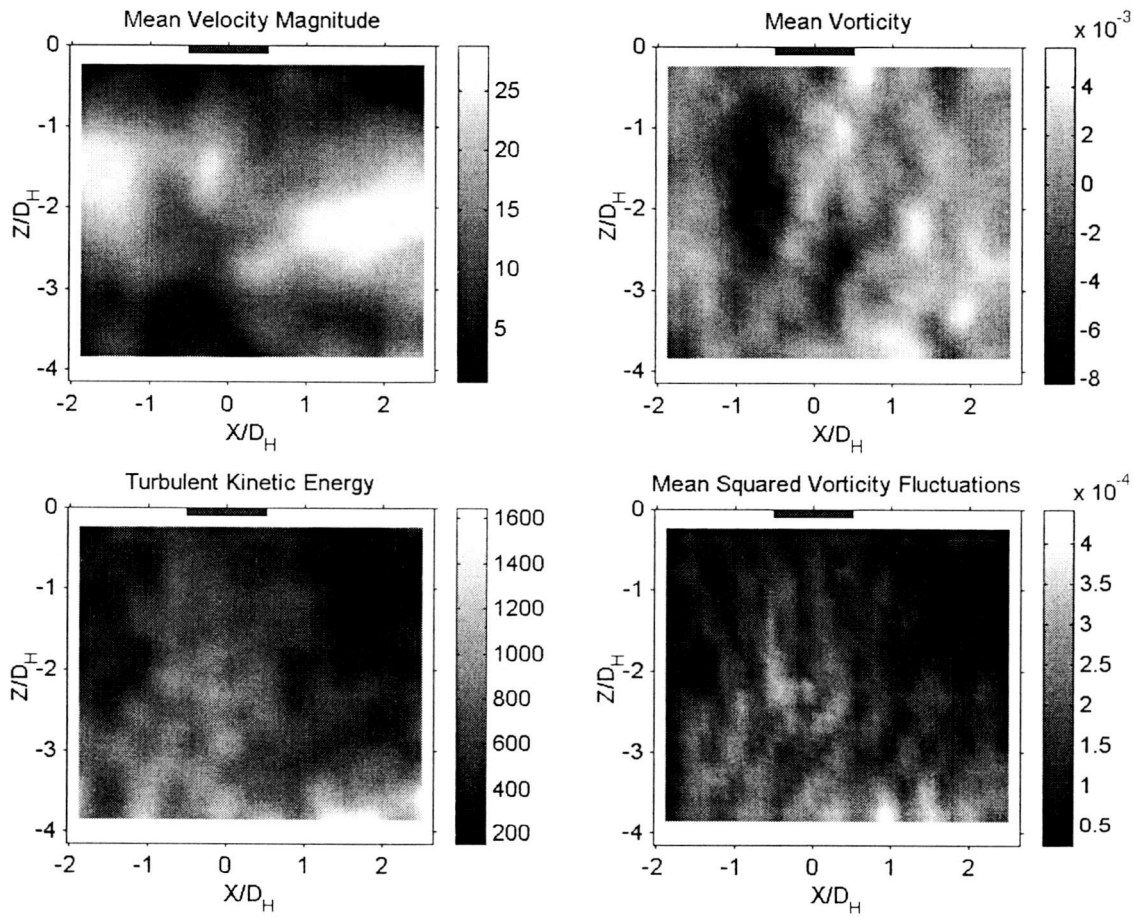

Figure 5.32. Flow characteristics, Circular jet,
H/D_H=4, Vr=0.159, Re=15,800

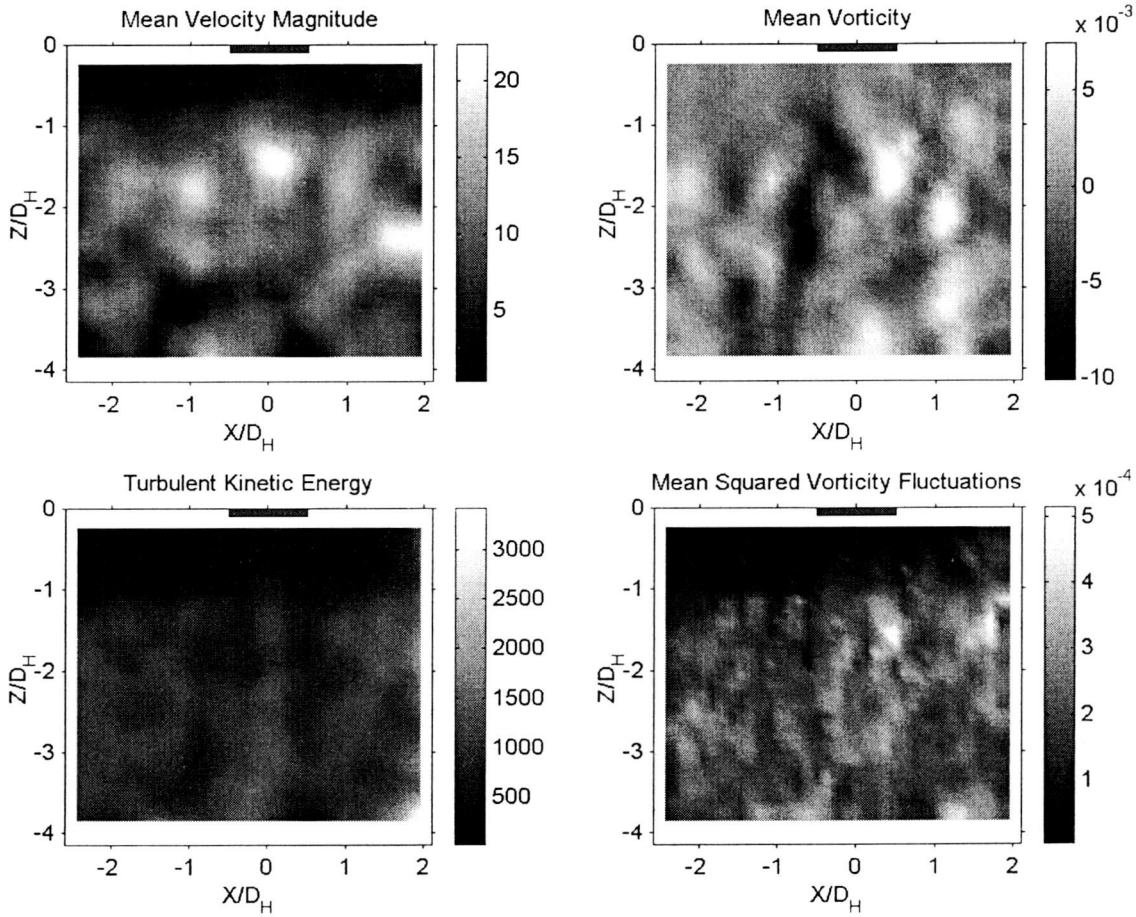

Figure 5.33. Flow characteristics, Cusped ellipse (0°) jet,
H/D_H=4, Vr=0.159, Re=13,500

Further downstream, at jet 6, singular changes occur. Figures 5.30 and 5.31 show the mean velocity vector field plot for the circular and the cusped ellipse (0°) jet 6. For the circular jet, the surface vortex [region 4] seems to strangely collide with the jet column [region 1], deflecting the column significantly downstream. The surface vortex size appears to expand in the streamwise direction while it shrinks in height. The jet column velocity reaches a minimum just at the interface with the surface vortex, before accelerating in the downstream direction. Consequently, the entrainment of the downstream flow increased. The different flow characteristics for the circular jet are shown in Figure 5.32. The vorticity plot shows that the jet column is not disturbed until reaching the ground vortex interface and the shearing effect strength drops by 57%. The TKE and mean squared vorticity repartition appear to stay essentially the same but with a 36% increase in TKE levels and 43% increase in mean squared vorticity.

A major change is observed for the cusped ellipse (0°) jet, shown in Figure 5.31. As the jet breaks down into a downstream and return-flow a contraction of the jet column is observed at $1D_H$ from the impingement surface. This appears to create a slight "return-curve" of the downstream flow creating a larger and more diffuse impingement zone. This is speculated to be due to the axis switching effect, typical for non-axisymmetric jets where the major and minor axis interchange some distance downstream. This also explains the reduction of the jet column velocity, resulting from a flow transfer in the transversal direction. The surface vortex location appears unchanged with its center of rotation at $X=1D_H$ from the

stagnation point and at $Z=1D_H$ from the impingement surface. The different flow characteristics for the cusped ellipse (0°) jet are shown in Figure 5.33. Significant decreases are observed for all the flow properties. The average over the flow field shows a 39% decrease in TKE and a 65% decrease in dissipation.

Effects of the Impingement Distance

In this section, the influence of the impingement distance, H/D_H, on the flow structure of the circular jet array is investigated. The impingement distance is varied from 2 to 4. Results for the lower Reynolds number, Re=9,740, are investigated in details, but the Reynolds number influence is also discussed.

Recall from Figure 5.2, for $H/D_H=4$, the local flow coefficient, C_D, decreases slightly and monotonically from the back wall to the exit, with an average of 0.70. The change of C_D with Re are shown in Figure 5.34. For $H/D_H=2$, it is observed that the decrease along the downstream direction is more pronounced. C_D increases by 6% close to the back-wall (PT1) and simultaneously decreases by less than 2% at the exit (PT5), resulting in an average flow coefficient, $<C_D>$, close to 0.73. When the height of the channel is reduced to $H/D_H=1$ (Figure 5.35), C_D increases by 13% close to the back wall and decrease by 8% close to the exit, with the average flow coefficient at 0.74. Therefore, the use of the average flow coefficient, $<C_D>$, has to be interpreted with care, since a very low impingement

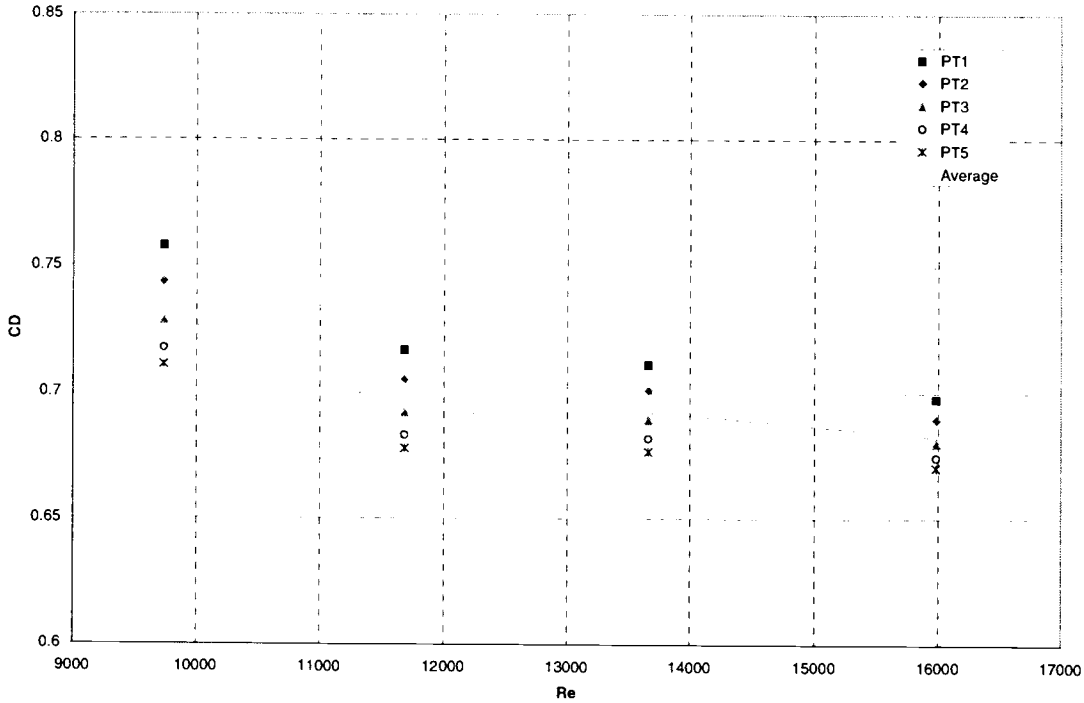

Figure 5.34 Flow coefficient, Circular jet, $H/D_H=2$

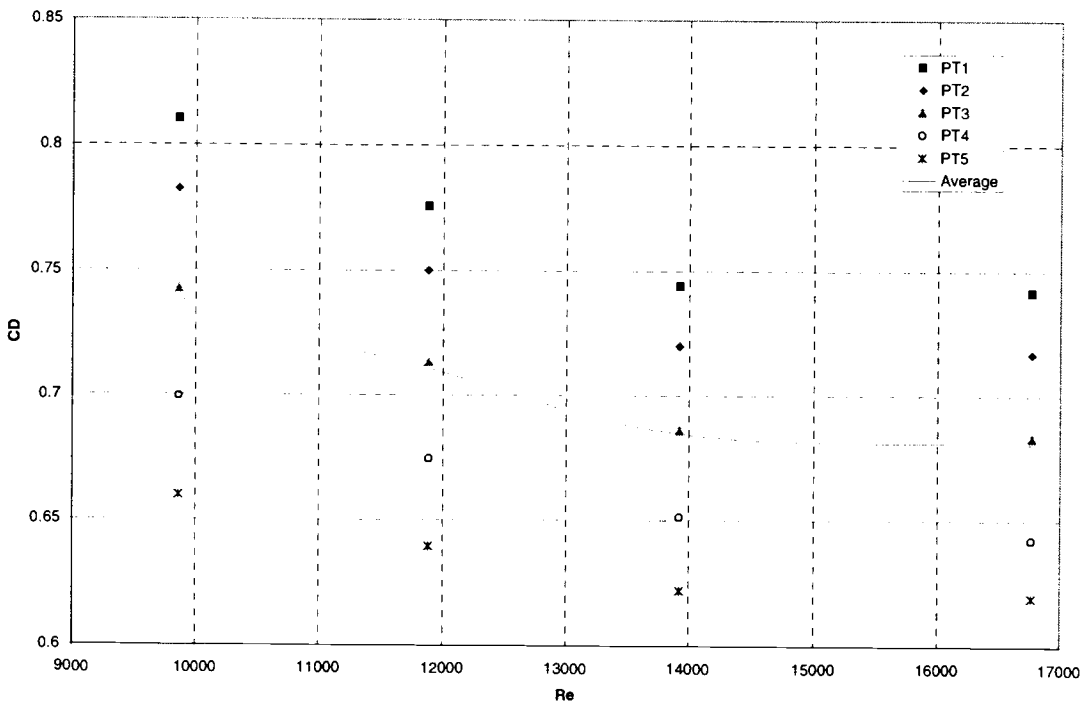

Figure 5.35 Flow coefficient, Circular jet, $H/D_H=1$

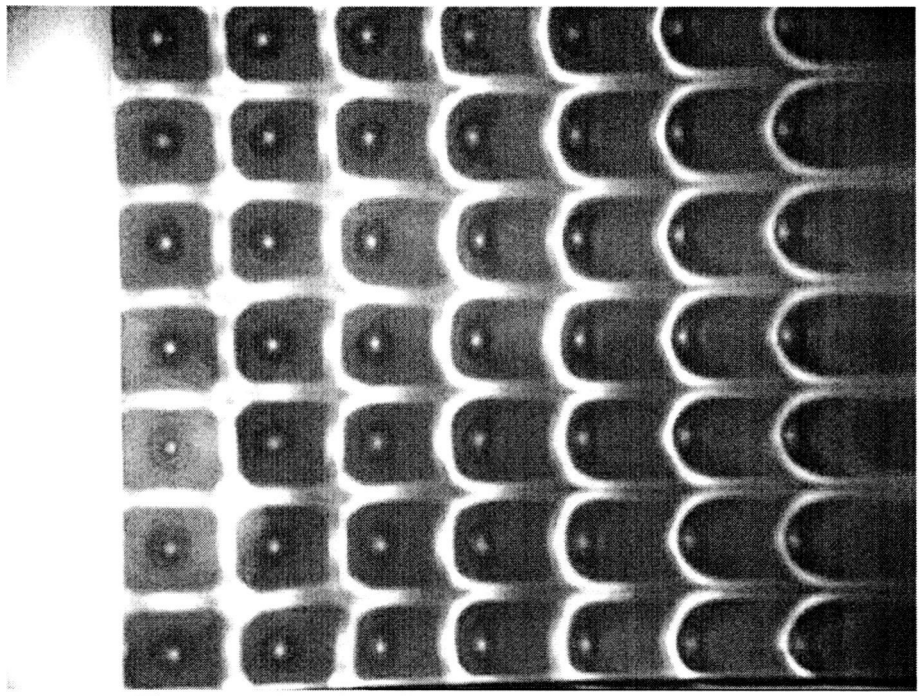

Figure 5.36 Surface flow visualization, Circular jet, $H/D_H=2$, Re=9,740

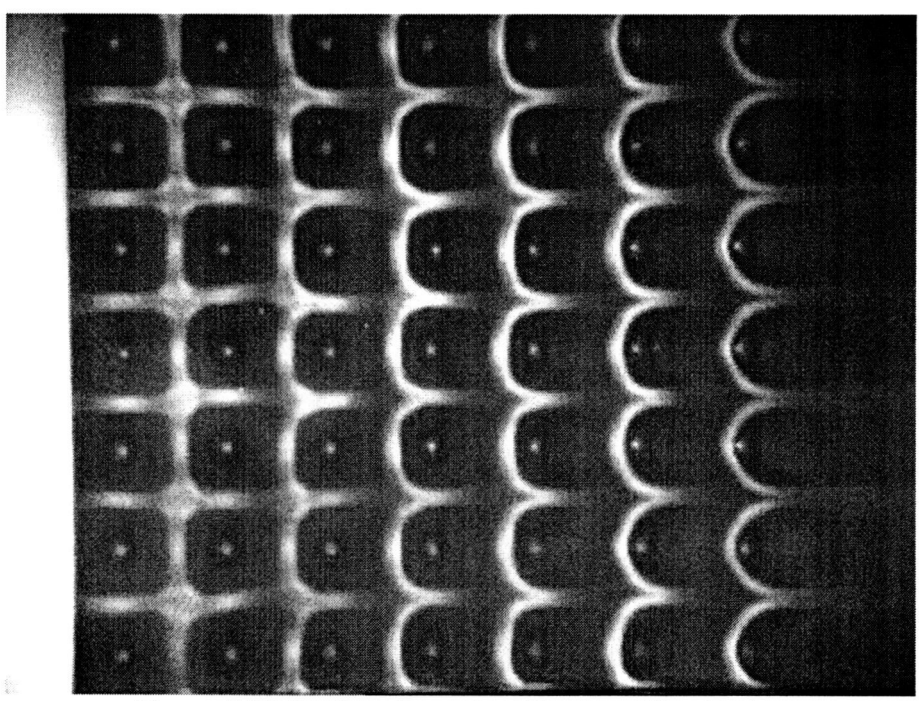

Figure 5.37 Surface flow visualization, Circular jet, $H/D_H=2$, Re=15,830

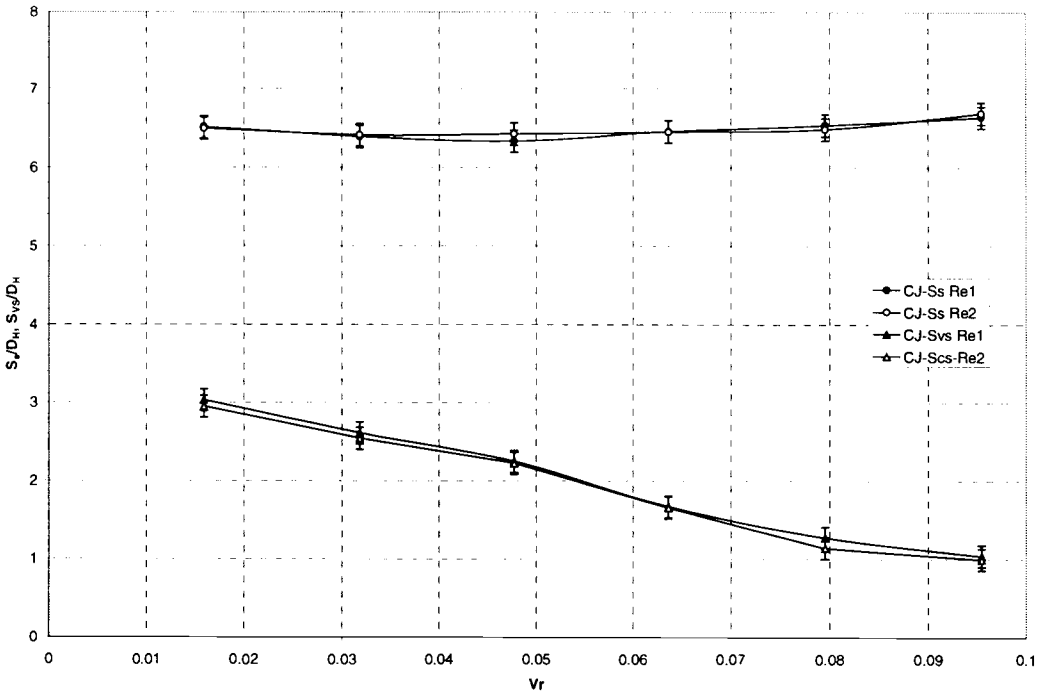

Figure 5.38 Surface vortex and stagnation point relative location, Circular jet, H/D_H=2, Re1=9,740 and Re2=15,830

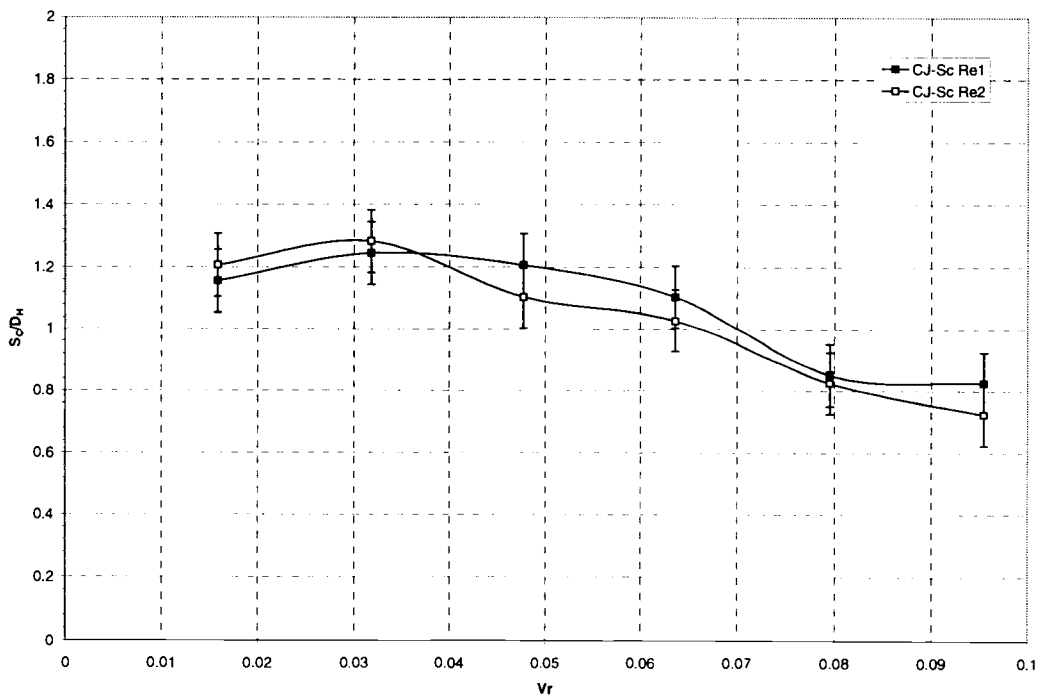

Figure 5.39 Surface vortex deposit size, Circular jet, H/D_H=2, Re1=9,740 and Re2=15,830

distance results in large variations over the surface. Large impingement distances have fairly uniform values for the average flow coefficient $<C_D>$.

Figures 5.36 and 5.37 show the surface flow visualization for $H/D_H=2$ and for both low and high Re. Figure 5.38 shows the change of S_{VS} and S_S along the flow. The surface vortex-to-stagnation point distance decreases along the downstream flow with equivalent values and slope for both lower and higher Re. S_{VS} decreases linearly and reaches a minimum of $1D_H$ at the channel exit indicating that the surface vortex is close to the stagnation point or that its size decreases greatly. The surface vortex separation distance, S_S, grows slightly along the downstream direction but by less than 6%. The surface vortex stagnation size, S_C, appears to decrease along the downstream direction as shown in Figure 5.39.

At the center of the jet array, at jet 4, the crossflow-to-jet velocity ratio is $V_r=0.048$. The mean velocity vector field plot for the circular jet is shown in Figure 5.40. A relatively weak surface vortex is visible, impinging against the jet column and deflecting it downstream. Its center of rotation appears is approximately from $Z=0.2D_H$ to the impingement surface, but extends to $X=1.2D_H$ in the streamwise direction. The flow appears to accelerate in a similar way, as the case for the flow from jet 6, with $H/D_H=4$ and high Re (Figure 5.30). The jet column appears to entirely feed the downstream flow, creating a $0.2D_H$ thick parallel flow along the impingement surface. The vorticity plots in Figure 5.42 show that several spots of counter-rotating vorticity appears along the impingement surface accompanied by a 40% decrease in vorticity level, when compared to $H/D_H=4$. The TKE and mean

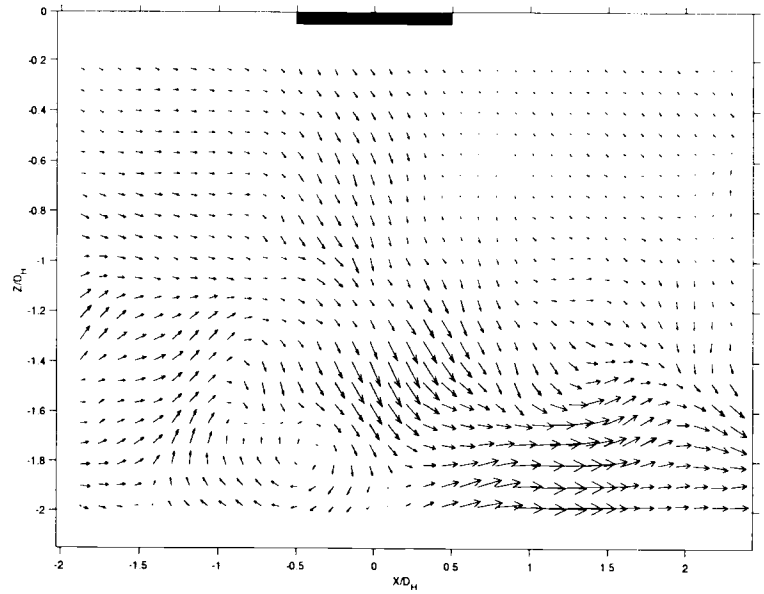

Figure 5.40 PIV, Circular jet, H/D_H=2, Vr=0.048, Re=9,740

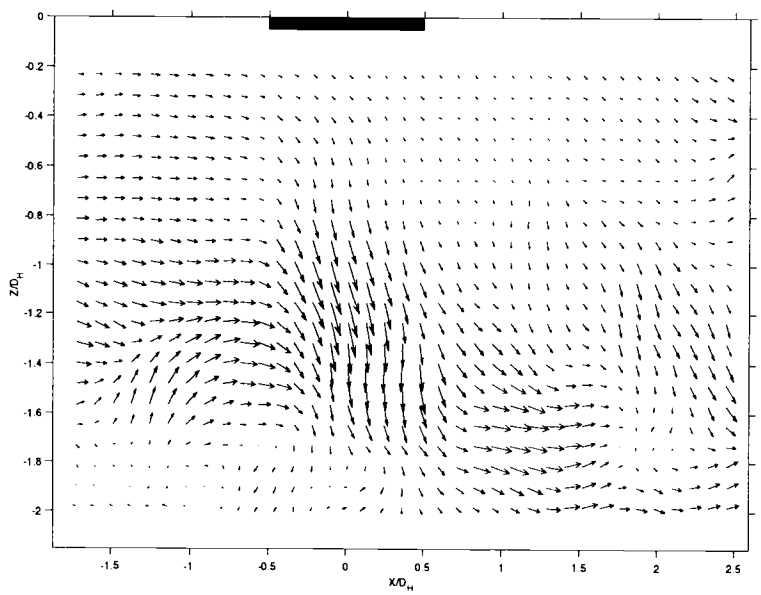

Figure 5.41 PIV, Circular jet, H/D_H=2, Vr=0.048, Re=15,830

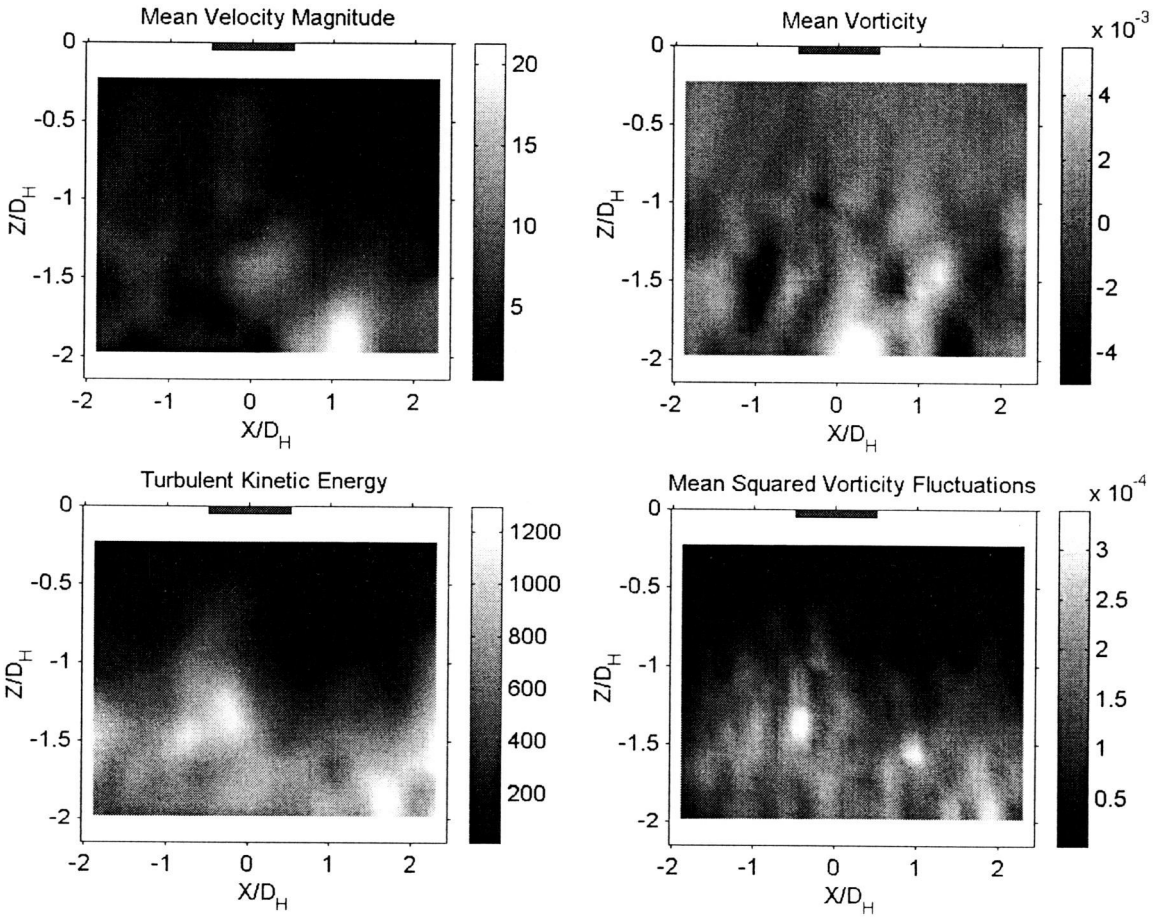

Figure 5.42 Flow characteristics, Circular jet,
H/D_H=2, Vr=0.048, Re=9,740

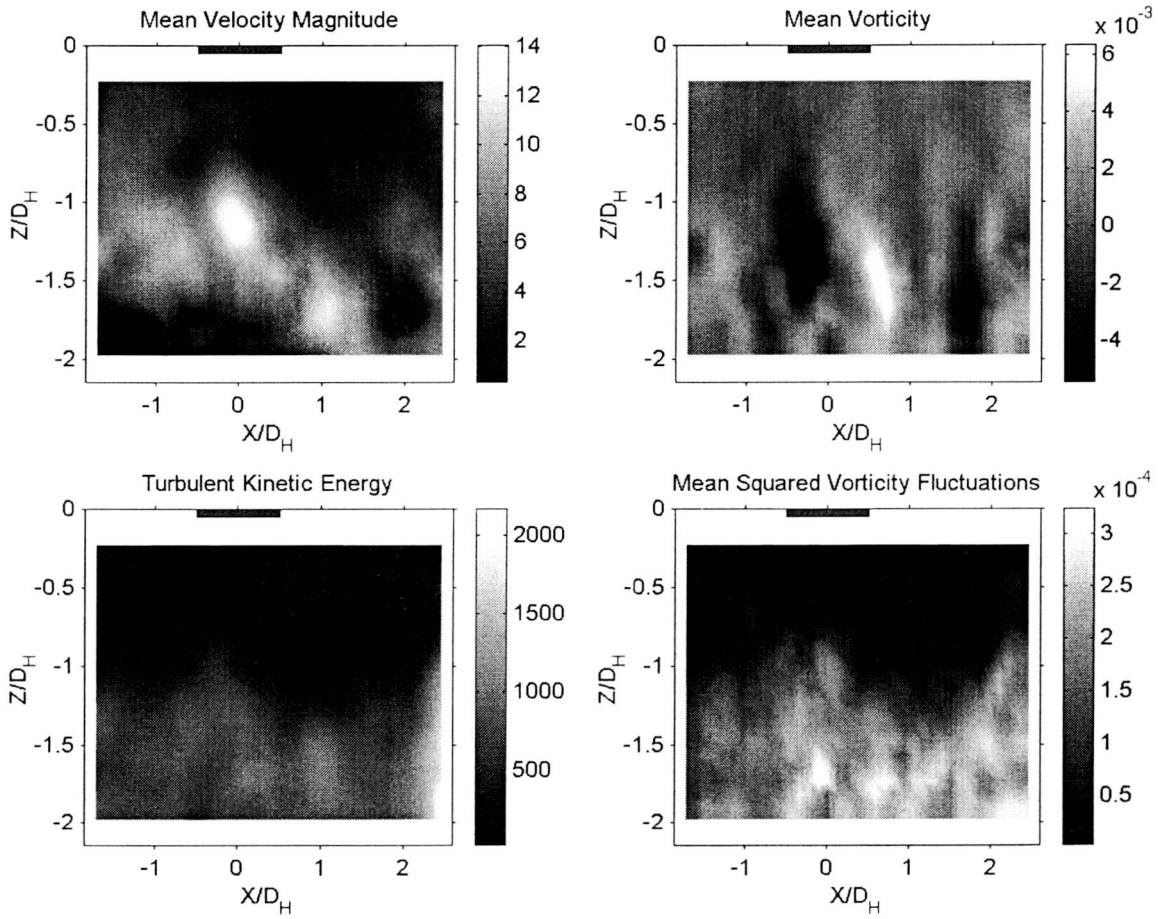

Figure 5.43 Flow characteristics, Circular jet,
H/D_H=2, Vr=0.048, Re=15,830

squared vorticity plots in Figure 5.42 show a more localized creation and dissipation of turbulence along the impingement surface. The levels of TKE and dissipation drop by 47% and 51%, respectively, compared to H/D_H=4 and same low Re. The mean velocity vector field for the same jet but for a higher Re is shown in Figure 5.41 with the associated flow characteristics in Figure 5.43. Increasing Re seems to strengthen the surface vortex both in speed and size, creating a stronger acceleration of the jet column with a smaller deflection of the jet. The vorticity plot in Figure 5.43 shows a slightly better defined jet column with the classic pair of counter-rotating vorticity pockets defining the jet shearing with the crossflow. The TKE and mean squared vorticity fields don't appear to be different than the precedent case (Figure 5.42), with H/D_H=2 and a lower Re.

Further downstream, at jet 6, remarkable changes occur. The crossflow-to-jet velocity ratio at jet 6 is V_r=0.095. These changes are shown in the mean velocity vector field, Figure 5.44. For low Re, the surface vortex appears to merge and accelerate with the jet column, resulting in a strong downstream parallel flow. The surface vortex size increases to approximately one half of the channel height. The center of rotation appears to move downstream, at $X=0.6D_H$ from the stagnation point. The vorticity plots show a well defined jet column with a symmetry breakup half way down the height of the channel. Compared to H/D_H=4, a 11% decrease in TKE and a 1% decrease in mean squared vorticity can be observed from Figure 5.46. The mean velocity vector field for the same jet and conditions but with a higher Re is shown in Figure 5.45, and the corresponding flow characteristics in

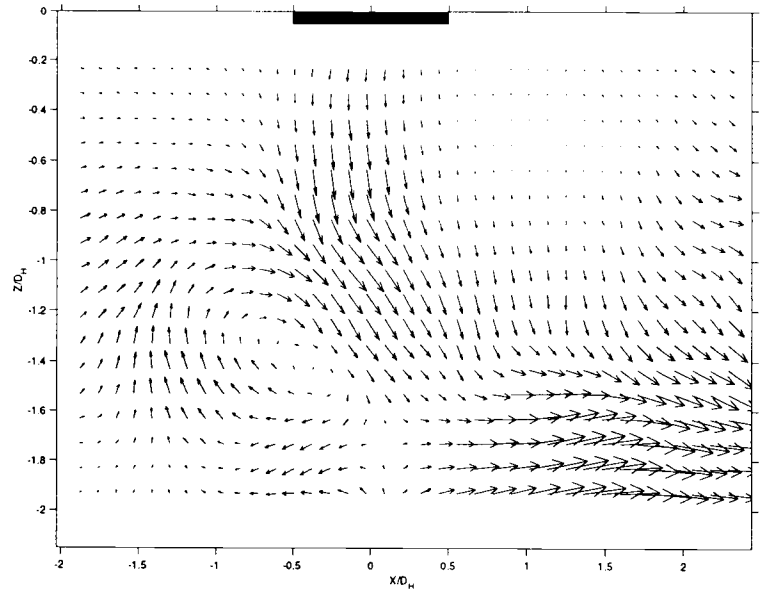

Figure 5.44 PIV, Circular jet, H/D_H=2, Vr=0.095, Re=9,740

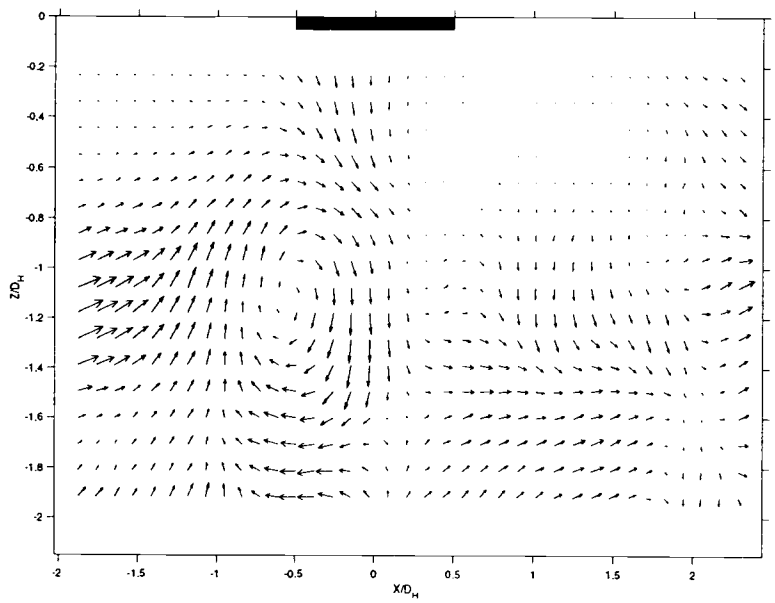

Figure 5.45 PIV, Circular jet, H/D_H=2, Vr=0.095, Re=15,830

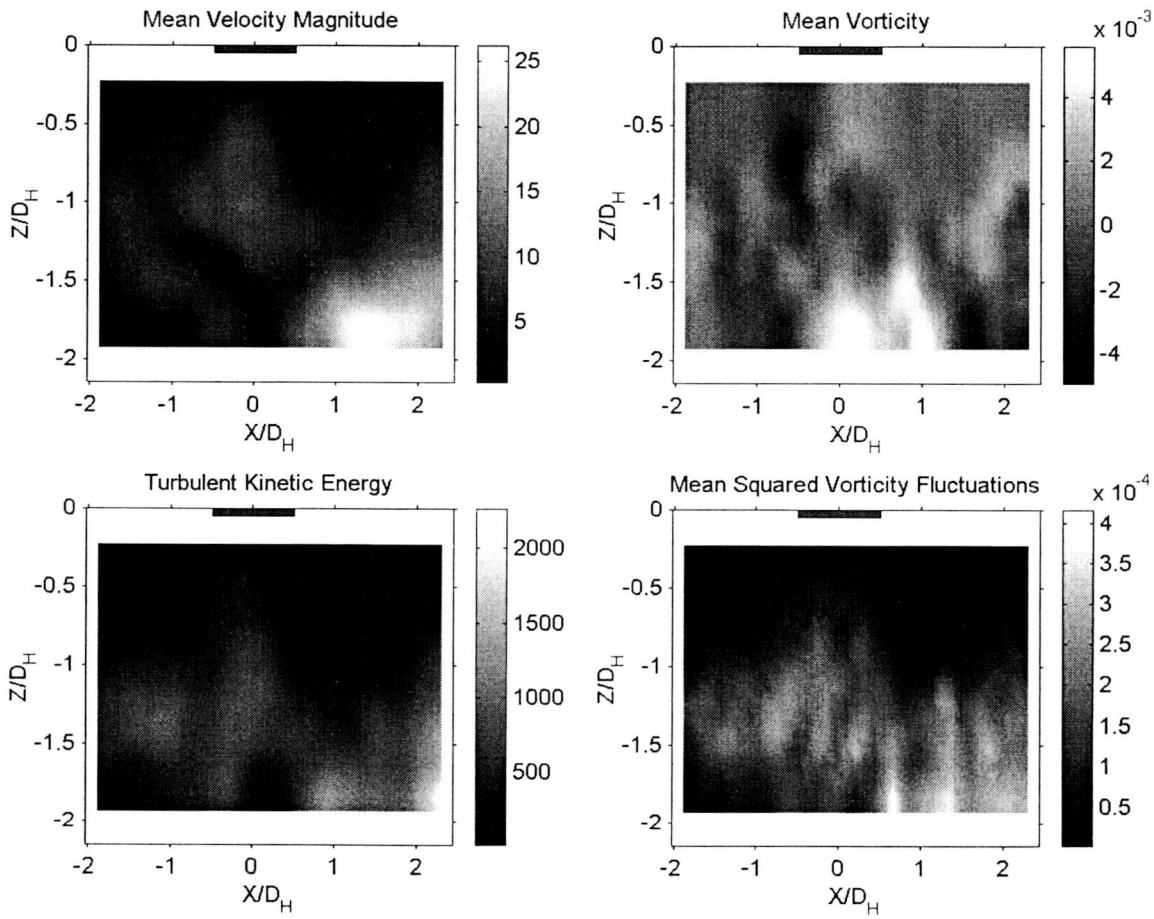

Figure 5.46 Flow characteristics, Circular jet,
H/D_H=2, Vr=0.095, Re=9,740

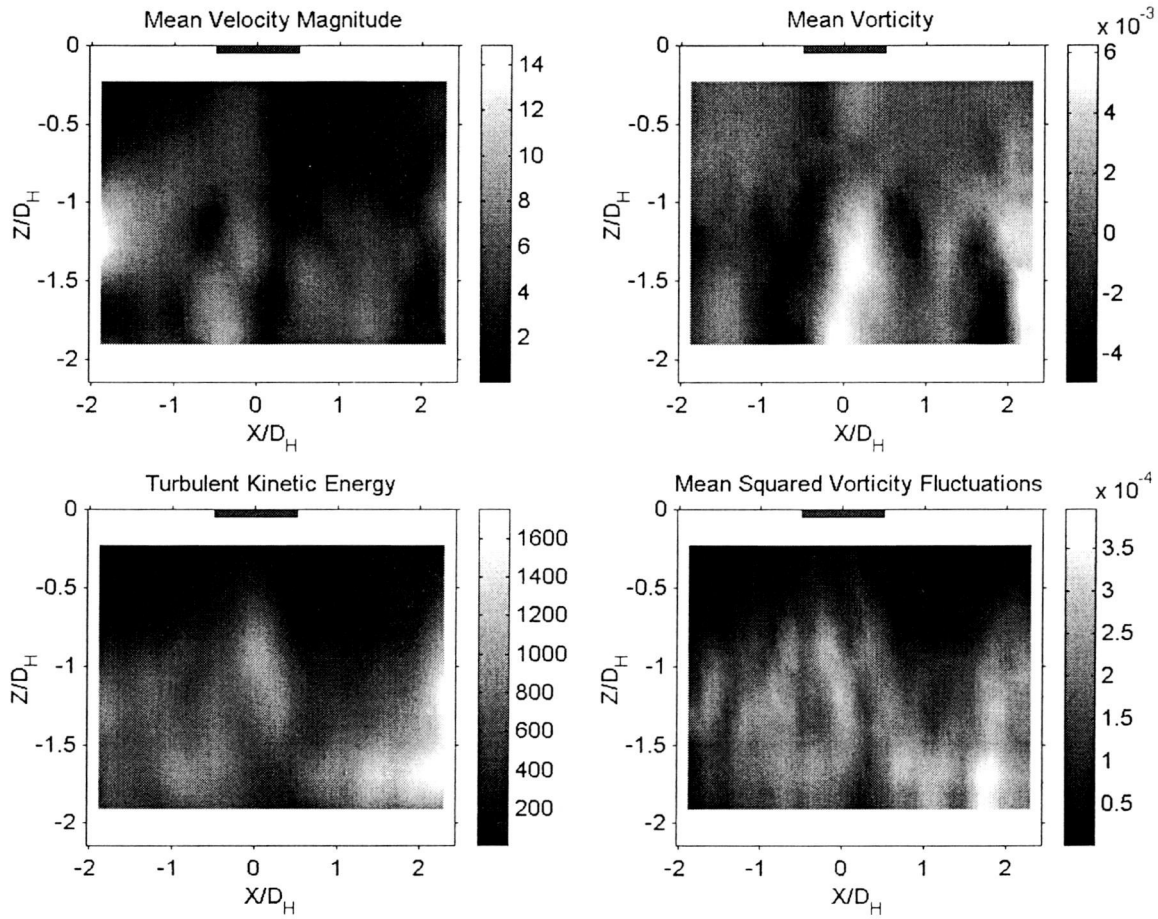

Figure 5.47 Flow characteristics, Circular jet,
H/D_H=2, Vr=0.095, Re=15,830

Figure 5.47. Increasing the Reynolds number seems to increase the feedback process: the jet column appears to merge completely with the surface vortex, feeding directly into the downstream jet location. The vorticity plot shows a larger shearing layer at the jet-surface vortex interface, accompanied by a 78% drop in intensity. There is no downstream deflection is apparent, and a similar downstream flow can be observed, but weaker in magnitude than the lower Re case. Compared to $H/D_H=4$, for higher Re, the level of TKE unexpectedly decreased by 30% while the mean squared vorticity decreased by 23%.

Effects of the Geometry Alignment of the Cusped Ellipse Jet Array

The cusped ellipse shape is a non-axisymmetric shape. Therefore, the jet array can be set into two configurations: the first one with the major axis aligned parallel to the crossflow, and the second one with the major axis aligned normal to the crossflow. This section discusses the effect of these two configurations on the flow structure. The cusped ellipse (0°) and the cusped ellipse (90°) jet arrays are presented for the following conditions: high impingement distance ($H/D_H=4$) and Reynolds number values ranging from 8,500 to 13,500.

The evolution of the flow coefficient versus increasing values of Re are shown in Figure 5.48. Moving downstream from the back to the exit of the array, the flow coefficient, C_D, decreases slightly and monotonically for both

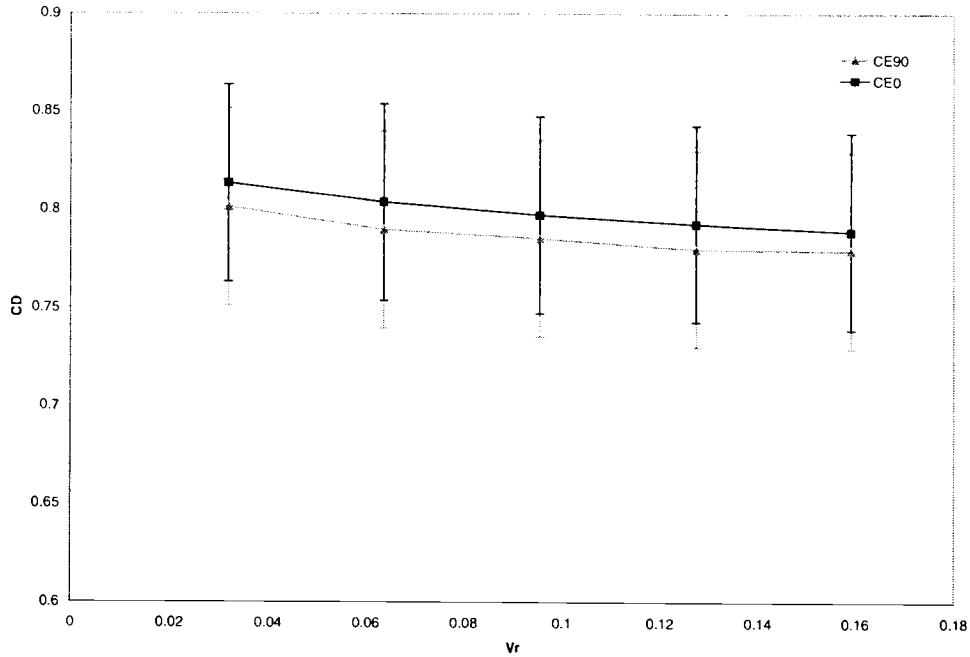

Figure 5.48 Flow coefficient, Cusped ellipse (0°) and (90°) jet arrays, H/D_H=4, Re=8,530

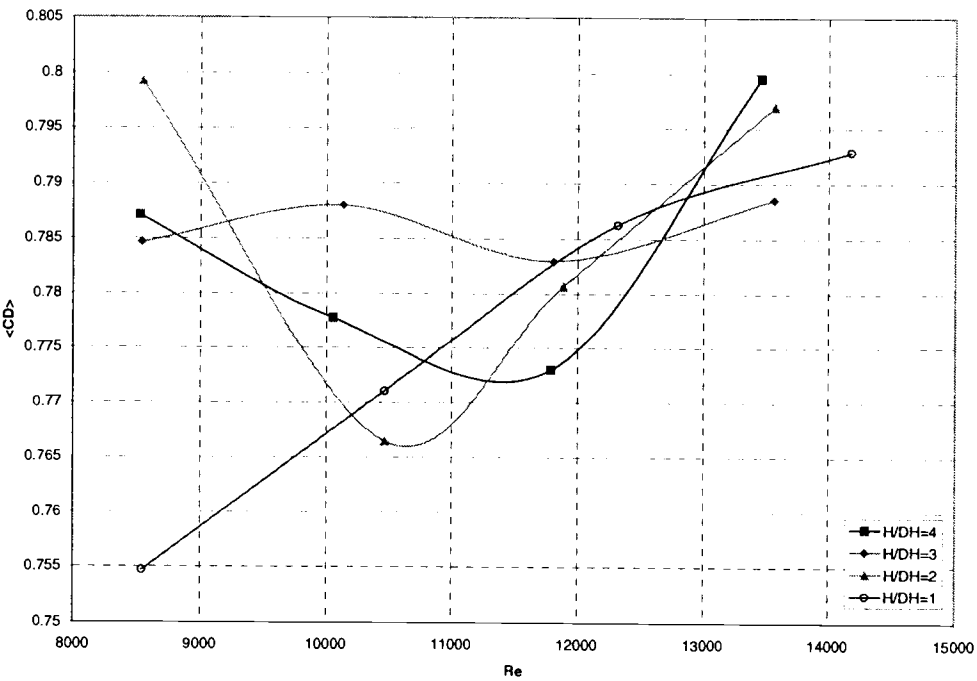

Figure 5.49 Average flow coefficient, Cusped ellipse (90°) jet array, H/D_H=4, Re=8,530

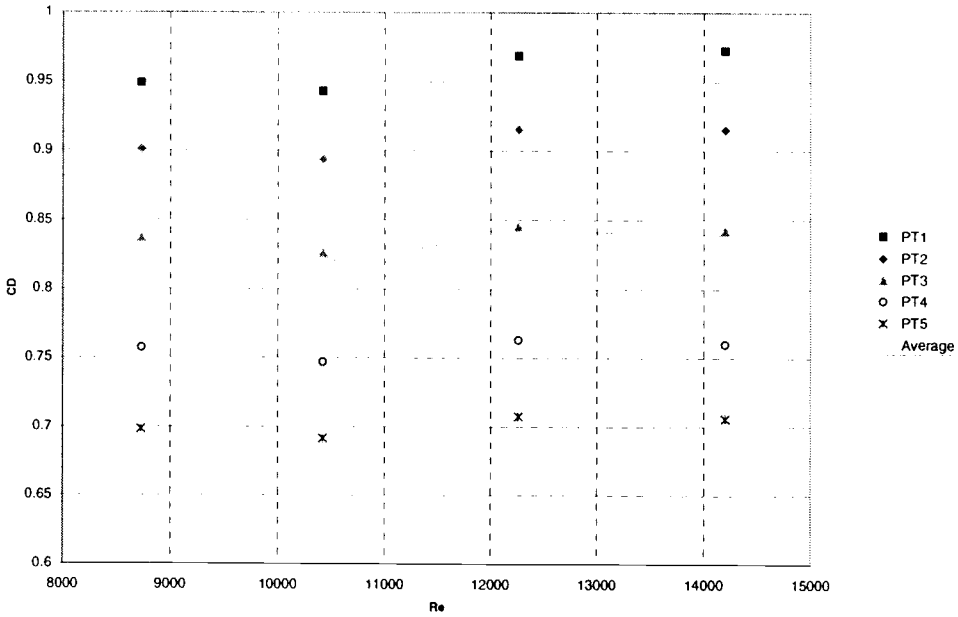

Figure 5.50 Flow coefficient, Cusped ellipse (0°) jet, H/D_H=1

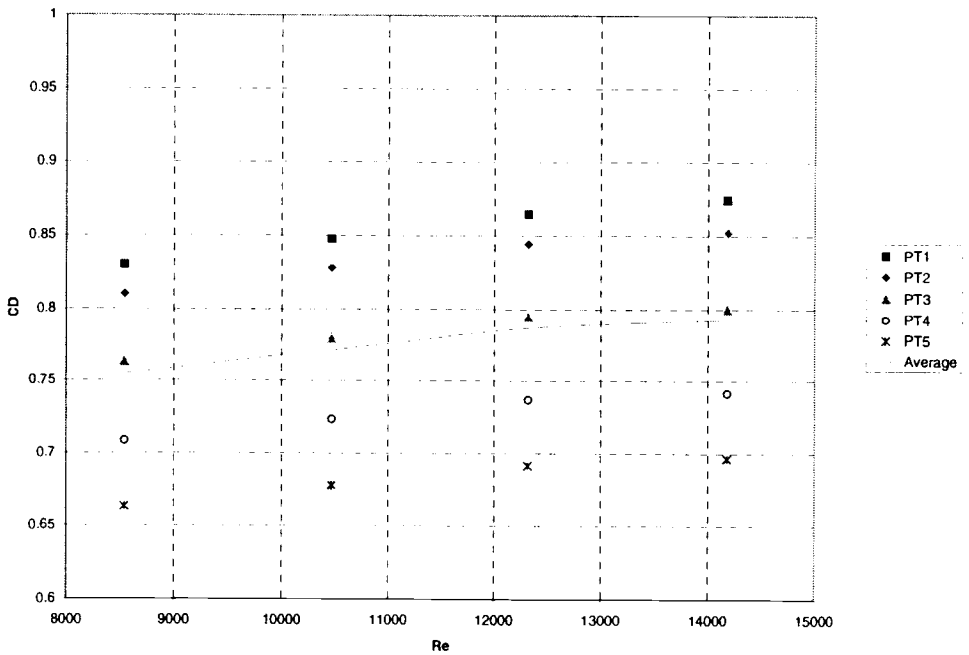

Figure 5.51 Flow coefficient, Cusped ellipse (90°) jet, H/D_H=1

configurations. Shown on Figure 5.49, are the variations of the "controversial" average flow coefficient, $<C_D>$, versus Re and the impingement distance, for the cusped ellipse (90°) jet array. For the lower Re, $<C_D>$ is approximately 0.80 for the cusped ellipse (0°) jet array and 0.79 for the cusped ellipse (90°) jet array. Recall from Figure 5.21, for the cusped ellipse (0°) jet array, no clear pattern could be identified concerning the dependence on Re. A similar behavior is observed for the cusped ellipse (90°) jet array jet with slightly lower values for C_D. When H/D_H is decreased, the flow coefficient increases closer to the back wall and decreases at the channel exit, increasing the slope of the curves. The flow coefficient results of the cusped ellipse (0°) and (90°) jet arrays for $H/D_H=1$ are shown in Figures 5.50 and 5.51. For this extreme case, the flow coefficient for the cusped ellipse (0°) jet array reaches values close to $C_D \approx 0.97$ at the back wall, and a 27% drop is observed along the downstream direction. For the cusped ellipse (90°) jet array the maximum value reaches $C_D \approx 0.87$ at the back wall and drops only 20% along the downstream direction. From the surface flow visualization for the cusped ellipse (90°) jet array at lower and higher Re, shown in Figures 5.52 and 5.53, no major difference is discernable between the two flow pattern. Figures 5.54 shows the evolution of S_{VS} and S_S along the flow direction. For $H/D_H=4$, the surface vortex-to-stagnation point distance appears slightly lower for the cusped ellipse (90°) jet array. The difference increases for lower impingement distance values: for $H/D_H=2$, the surface vortex is 30% closer for the cusped ellipse (90°) jet than for the cusped ellipse (0°) jet. For H/D_H the surface vortex size, S_c, is 14% smaller than for the cusped ellipse (0°) and

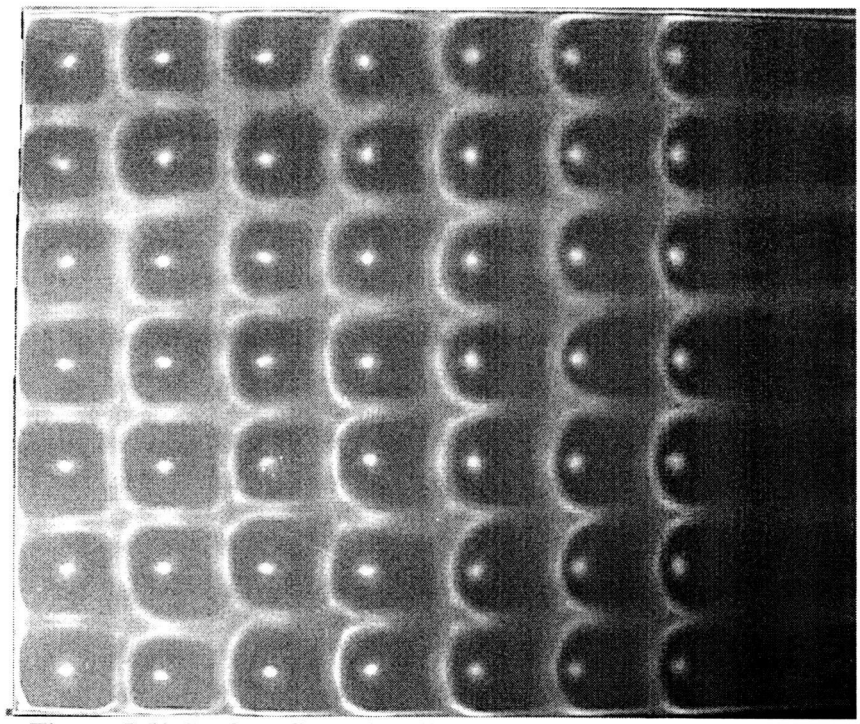

Figure 5.52 Surface flow visualization, Cusped ellipse (90°) jet, H/D_H=4, Re=8,530

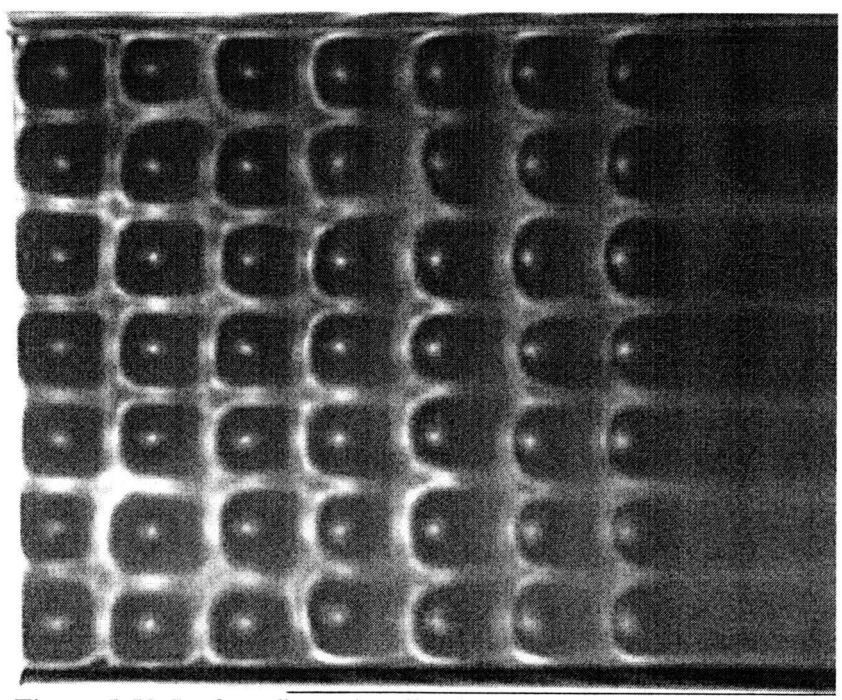

Figure 5.53 Surface flow visualization, Cusped ellipse (90°) jet, H/D_H=4, Re=13,460

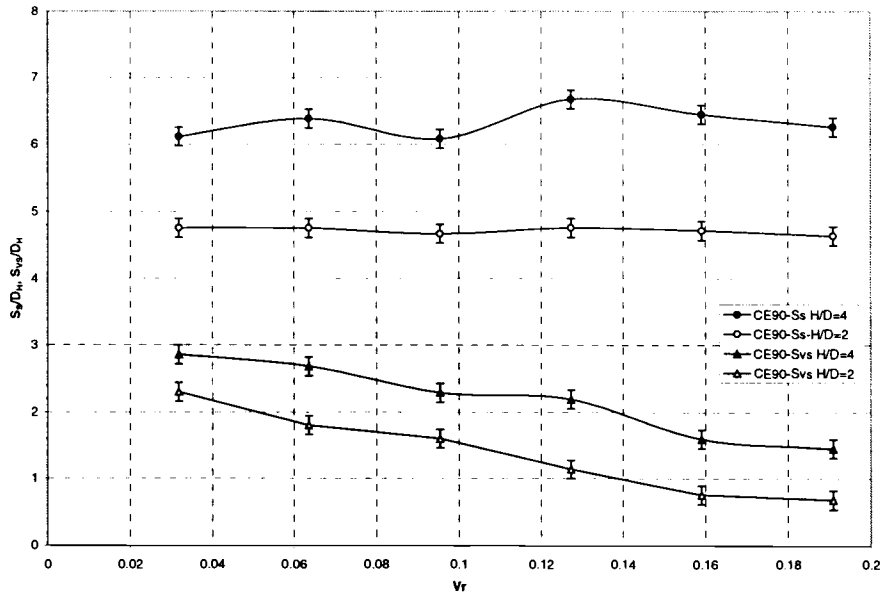

Figure 5.54 Surface vortex and stagnation point relative location, Cusped ellipse (90°) jet, $H/D_H=4$ and $H/D_H=2$

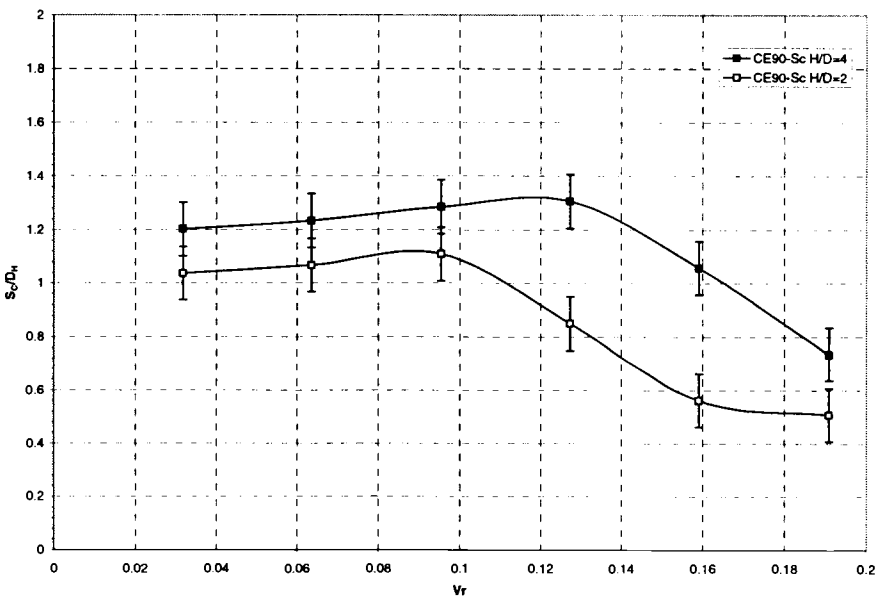

Figure 5.55 Surface vortex deposit size, Cusped ellipse (90°) jet, $H/D_H=4$ and $H/D_H=2$

the circular jet. A 37% drop is observed at the exit (Figure 5.55). For $H/D_H=2$, these result increase to 22% and 60%, respectively.

The mean velocity vector field plot for the cusped ellipse (90°) jet is shown in Figure 5.56. Close to the back wall, at jet 6, the crossflow-to-jet velocity ratio is $V_r=0.032$. No surface vortex is visible for both of the flow configurations. For the cusped ellipse (0°) jet, the jet column breaks down into a return and downstream flow (Figure 5.9). The return-flow, interacting with the upstream flow, appears to create a large rotating structure localized outside of the field of view. The cusped ellipse (90°) jet doesn't show any organized return-flow (Figure 5.56). The jet column appears to contract at $1D_H$ from the impingement surface and breakdown into relatively weak and multidirectional flows. The same behavior is observed for the larger Re, shown in Figure 5.57. The flow characteristics for the lower and higher Re are shown in Figures 5.58 and 5.59, respectively. The vorticity plots confirm the jet column disturbance [region 2] in the lower part of the channel, while multiple "pockets" of vorticity can be found all along the channel but with significant weakness. Compared to the cusped ellipse (0°) jet, the vorticity level is 60% smaller. For the TKE and mean squared vorticity, dramatic changes occur due to cusped ellipse alignment. The cusped ellipse (0°) jet shows a wide mixing of the flow all along the channel, particularly close to the impingement wall. The cusped ellipse (90°) jet shows no evidence of turbulence mixing except in the jet column and the TKE and mean squared vorticity levels drop by 76% and 75%, respectively.

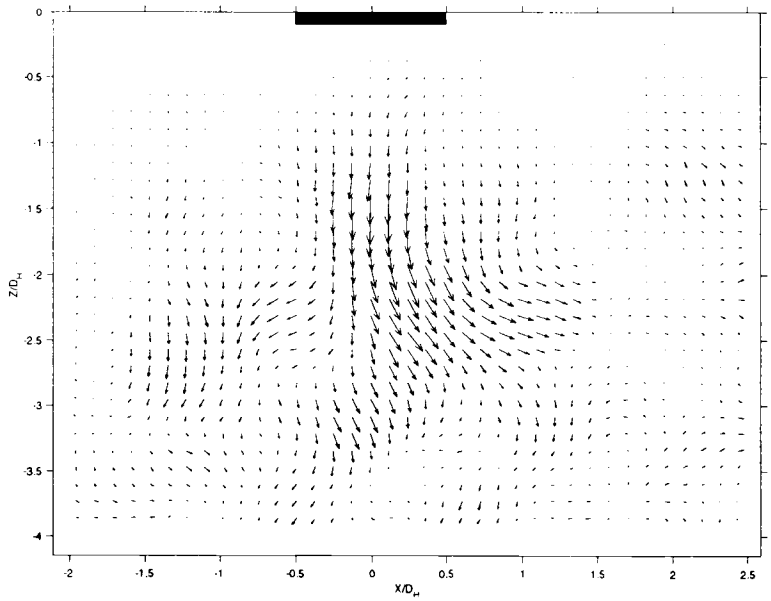

Figure 5.56 PIV, Cusped ellipse (90°) jet, H/D_H=4, Vr=0.032, Re=8,530

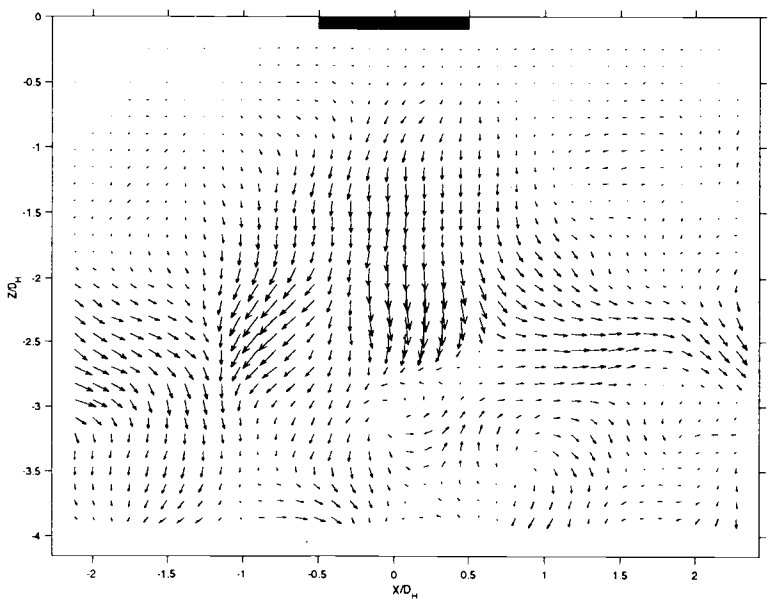

Figure 5.57 PIV, Cusped ellipse (90°) jet, H/D_H=4, Vr=0.032, Re=13,460

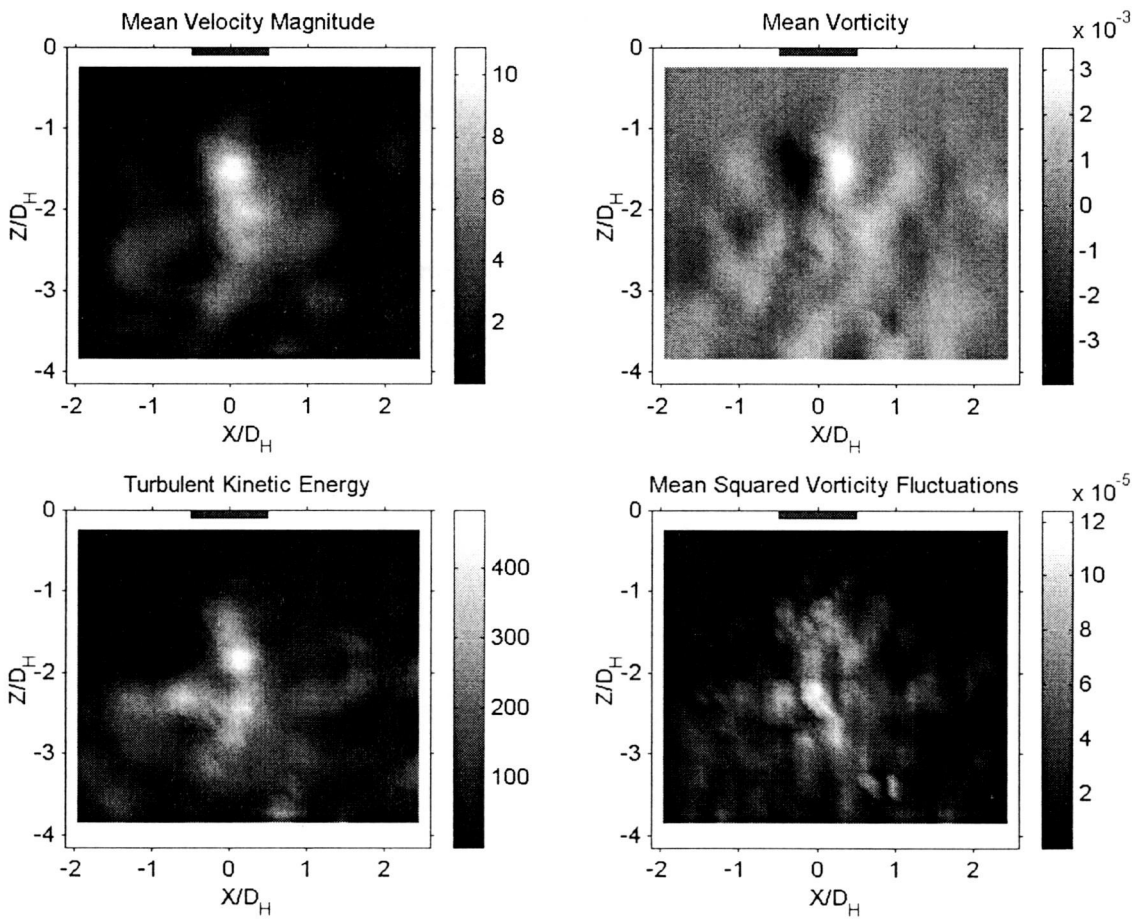

Figure 5.58 Flow characteristics, Cusped ellipse (90°) jet,
H/D_H=4, Vr=0.032, Re=8,530

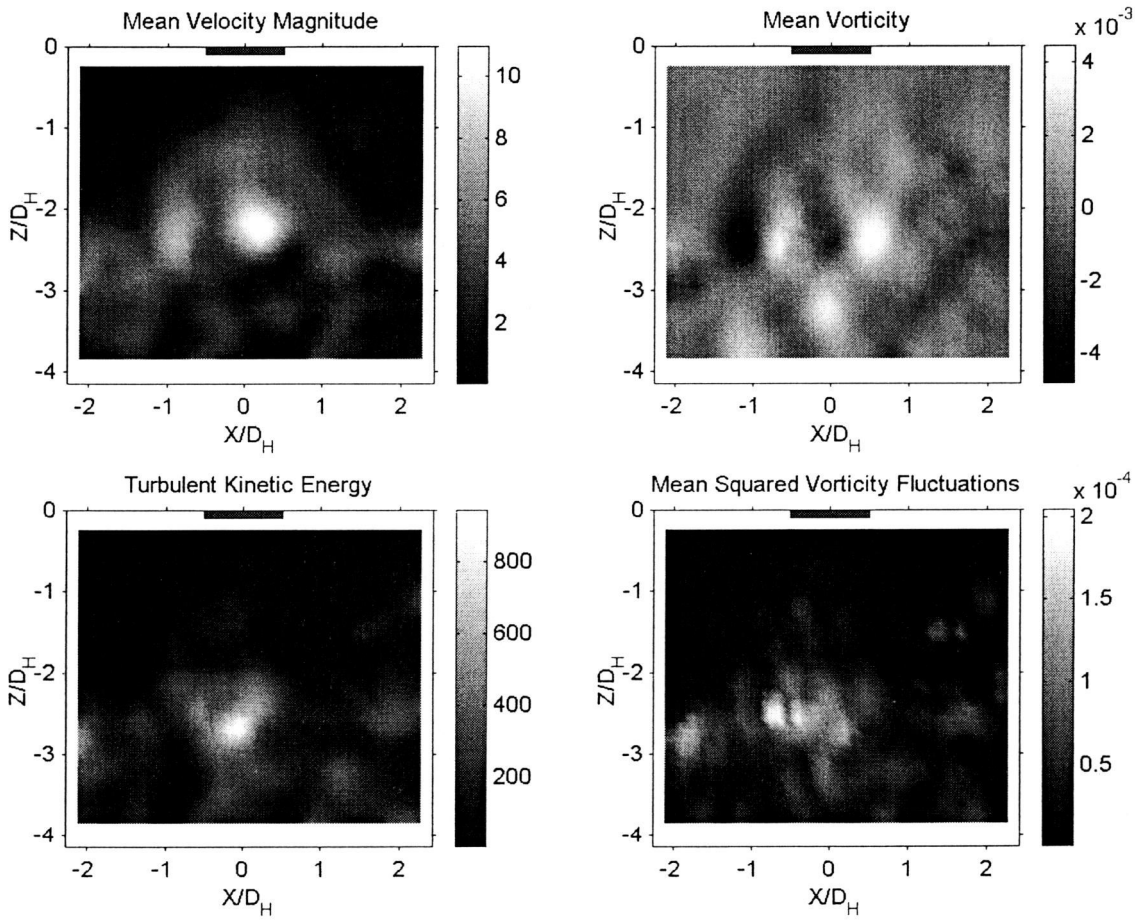

Figure 5.59 Flow characteristics, Cusped ellipse (90°) jet,
H/D_H=4, Vr=0.032, Re=13,460

Increasing Re appears to strengthen slightly the jet column and its shearing layers, but no other significant changes can be observed.

Further downstream, at jet 4, the crossflow-to-jet velocity ratio is V_r=0.095. The flow structure, shown in Figure 5.60, is very similar to the upstream jet 2 flow structure. While the cusped ellipse (0°) jet shows a surface vortex close to the jet column, there is no evidence of surface vortex formation for the cusped ellipse (90°) jet (Figure 5.60). The jet column appears to contract at $1.2D_H$ from the impingement surface, then re-expand and breakdown into relatively weak, multidirectional flows. The downstream flow appears to strengthen slightly when Re is increased (Figure 5.61). The flow characteristics for the cusped ellipse (90°) jet array at this location are shown in Figure 5.62. The jet shearing layers are well defined in the lower part of the flow, with a symmetry break at Z/D_H=3 which appears to be due to the axis switching effect. The vorticity level is still rather weak as for jet 2. The TKE and mean squared vorticity spread over a larger part of the channel than jet 2, but stay relatively localized in the jet column area. The TKE level drops by 45%, while the mean squared vorticity level drops by 49% when compared to the cusped ellipse (0°) jet.

Figures 5.61 and 5.63 show the flow structure and the associated characteristics when Re is increased. Surprisingly, no significant change can be observed. Figures 5.64 and 5.65 show the mean velocity vector field plot for the cusped ellipse (90°) jet 6. The crossflow-to-jet velocity ratio is V_r=0.159. The flow structure of the cusped ellipse (90°) jet appears to turn into a wall jet (Figure 5.64).

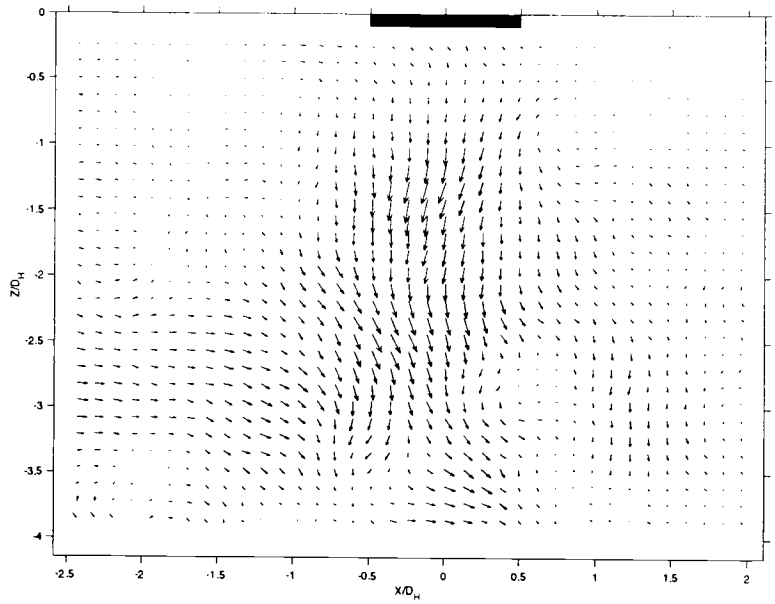

Figure 5.60 PIV, Cusped ellipse (90°) jet, H/D_H=4, Vr=0.095, Re=8,530

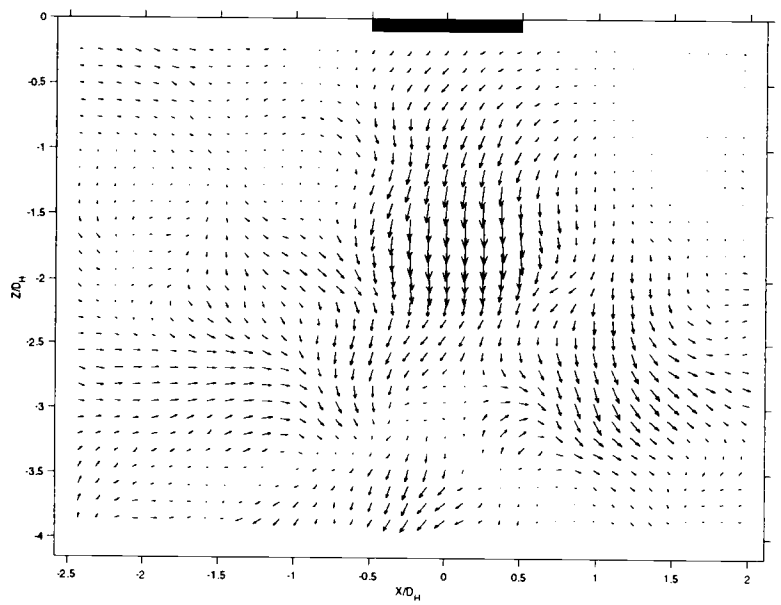

Figure 5.61 PIV, Cusped ellipse (90°) jet, H/D_H=4, Vr=0.095, Re=13,460

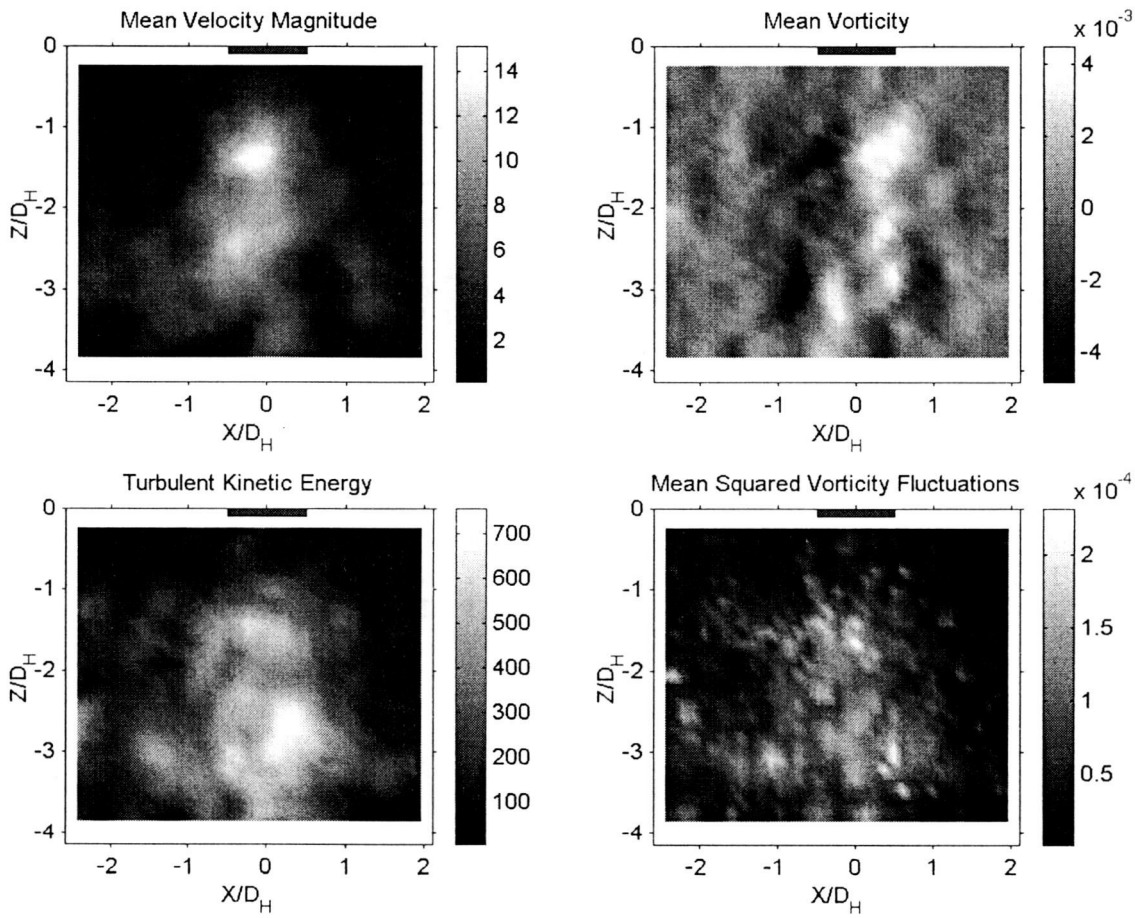

Figure 5.62 Flow characteristics, Cusped ellipse (90°) jet,
H/D_H=4, Vr=0.095, Re=8,530

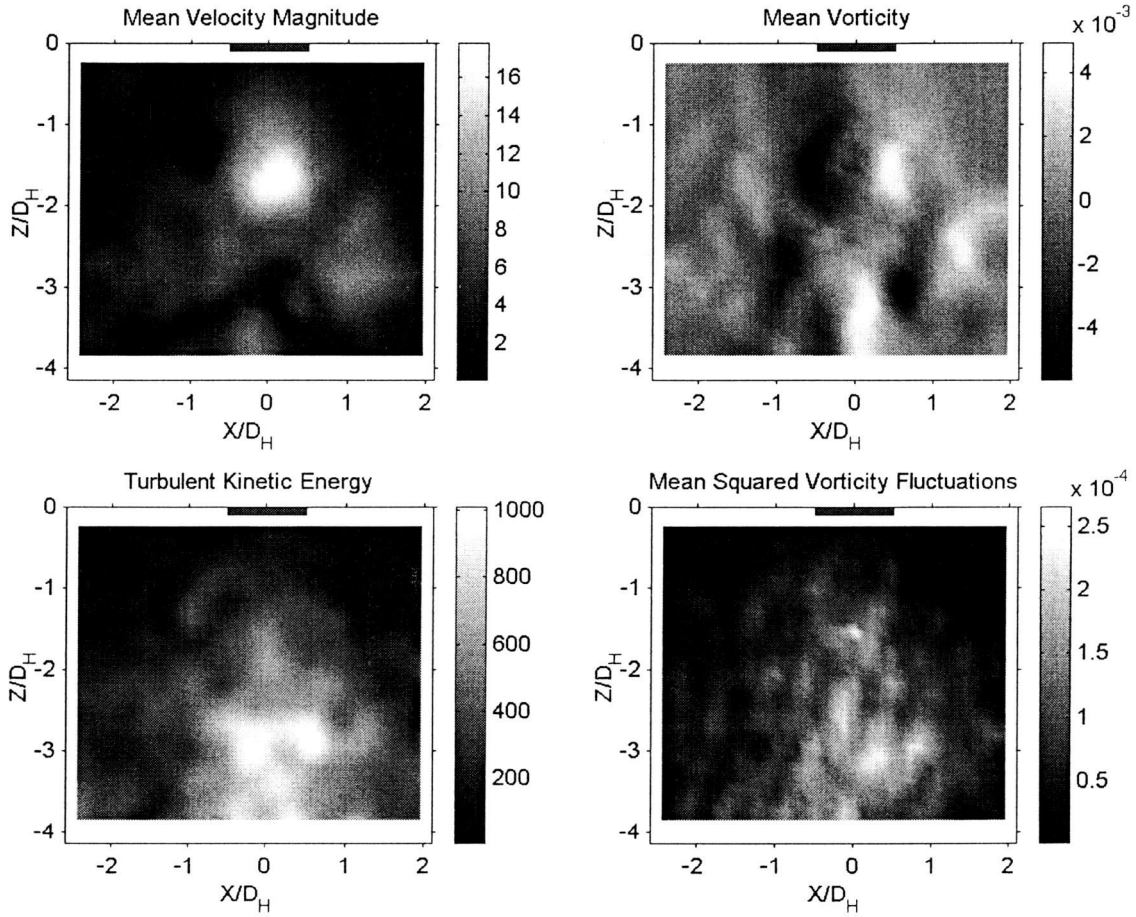

Figure 5.63 Flow characteristics, Cusped ellipse (90°) jet,
H/D_H=4, Vr=0.095, Re=13,460

The jet column is progressively deflected by the crossflow until it is completely aligned parallel with the impingement surface. The flow seems to grow in speed in the lower half of the channel, creating a large entrainment of the upper flow, but there is no surface vortex visible. Increasing the Reynolds number augments the flow entrainment and shows an increase in flow velocity, but the general flow structure remains the same (Figure 5.65). The flow characteristics for this jet and for the two different Re are shown in Figures 5.66 and 5.67. The jet shearing layers appear very scattered, and multiple pockets of vorticity can by found all over the jet column and the impingement point area. The TKE and mean squared vorticity spread over a larger area of the channel, but without matching the cusped ellipse (0°) jet mixing. No dramatic change in TKE and mean squared vorticity levels are observed when compared to those of jet 4. But when compared to the cusped ellipse (0°) jet, there is a drop of 57% for the TKE and a 76% drop for the mean squared vorticity.

Side-Wall Effects

During the PIV measurements, some configurations were less willing to show what they had to offer. The images obtained from the digital camera showed a zone of "blur" in the upper part of the flow, which introduced error into the analysis. This problem occurred mainly for the cusped ellipse configurations, but

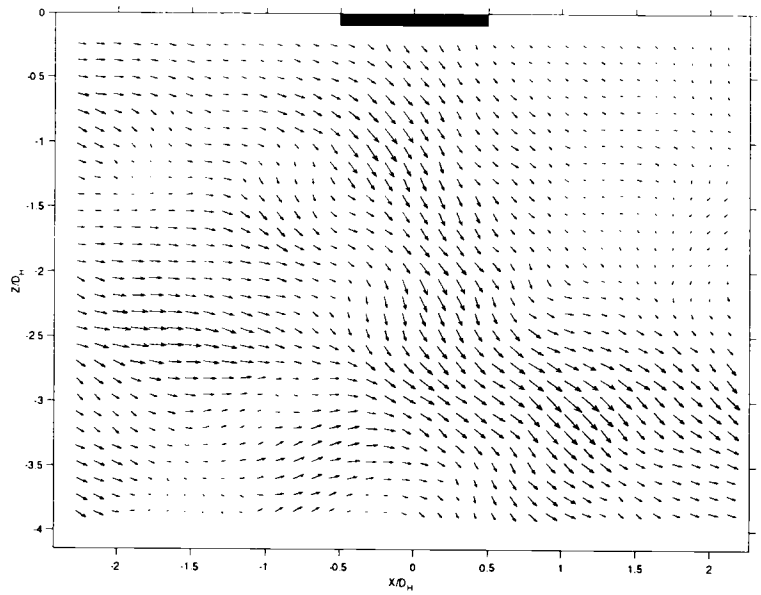

Figure 5.64 PIV, Cusped ellipse (90°) jet, H/D_H=4, Vr=0.159, Re=8,530

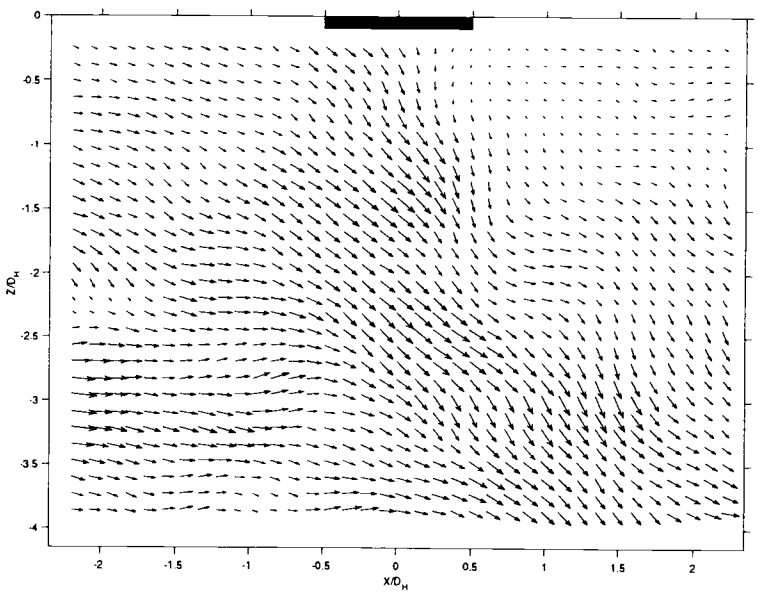

Figure 5.65 PIV, Cusped ellipse (90°) jet, H/D_H=4, Vr=0.159, Re=13,460

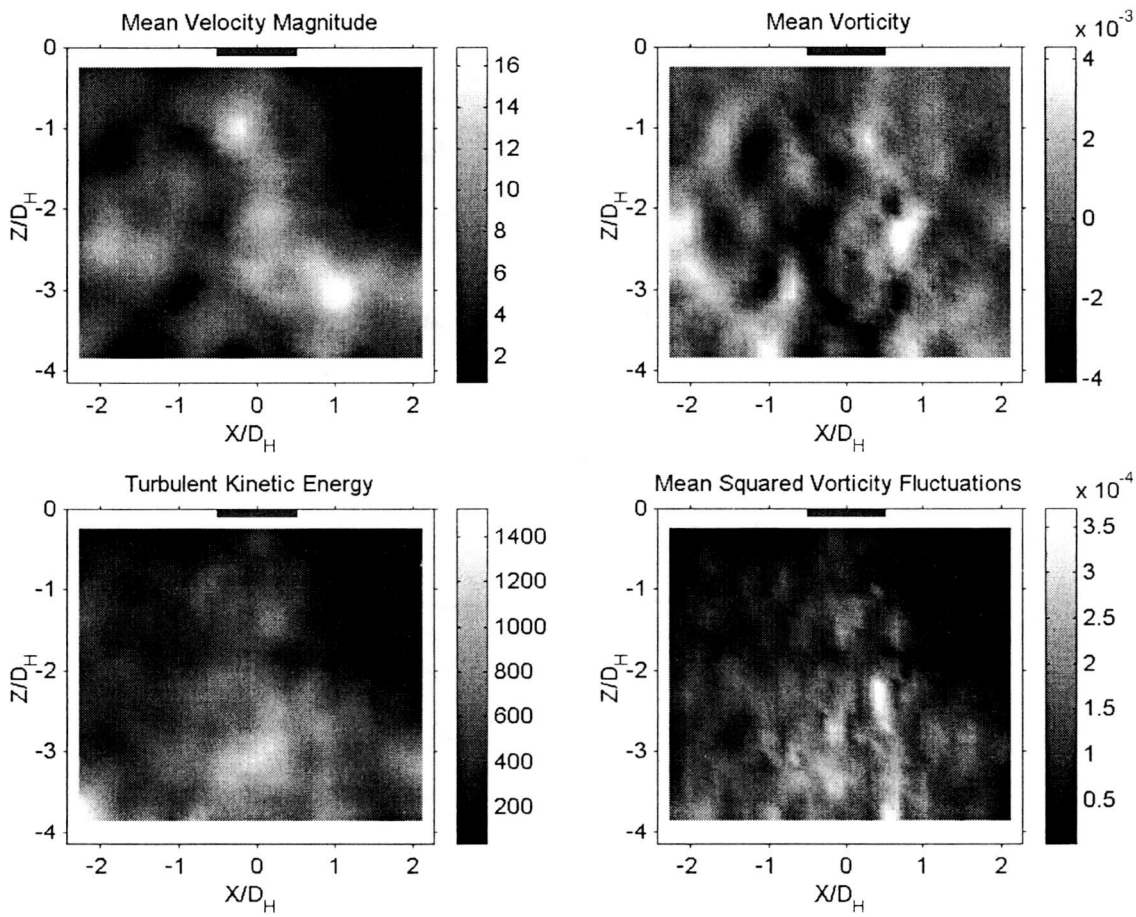

Figure 5.66 Flow characteristics, Cusped ellipse (90°) jet,
H/D_H=4, Vr=0.159, Re=8,530

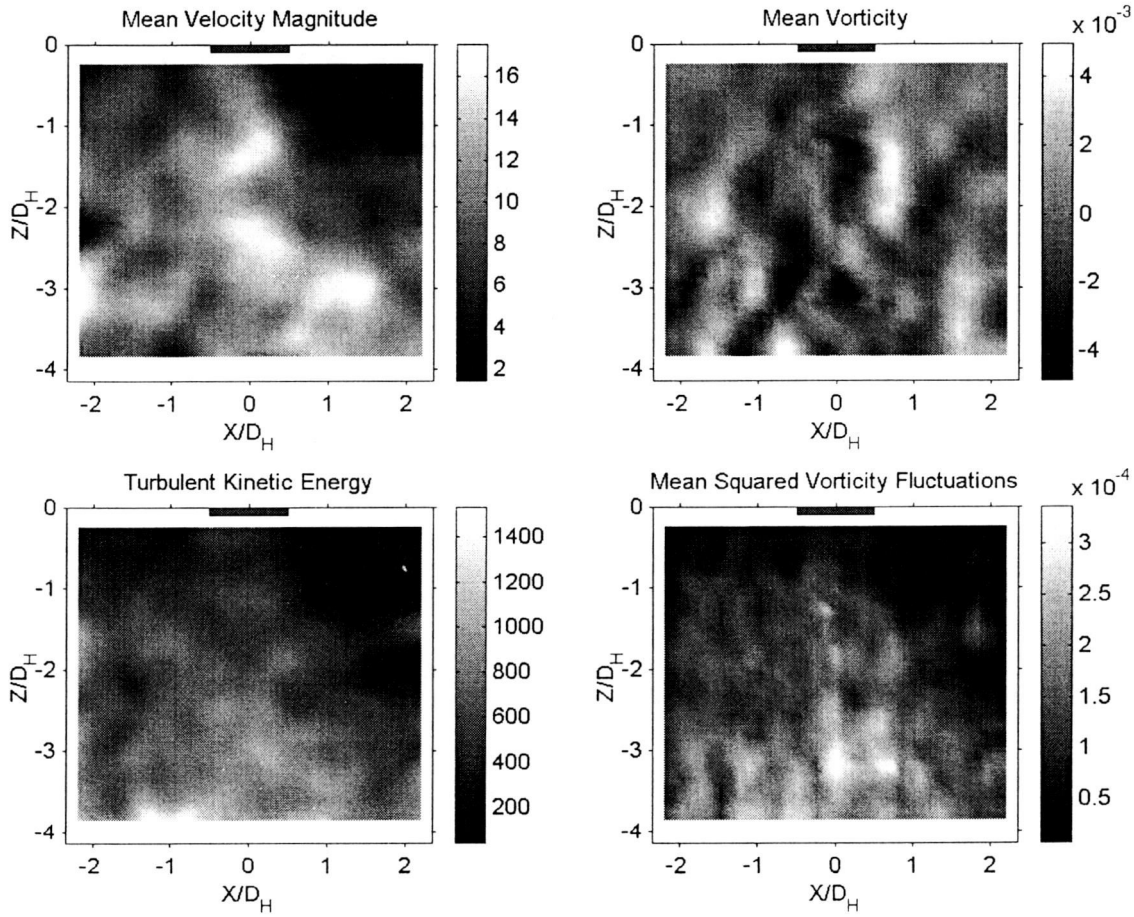

Figure 5.67 Flow characteristics, Cusped ellipse (90°) jet,
H/D_H=4, Vr=0.159, Re=13,460

also occurred for all of the jets when the impingement distance was low, $H/D_H=2$. The reason for this can be seen in Figure 5.68. The insert-layer used to identify the surface flow conditions was folded to fit the wall of the channel. This insert-layer provides information on the side-wall effects. As the surface vortex develops downstream around the edge jets, outside the PIV laser sheet, it also grows in height along the side-wall. A detachment zone is formed, resulting in a deposit of particles on the channel's sides. The camera is focused on the laser sheet's plane and the pictures are captured directly through the glass side-wall. The deposit on the wall explains the "blur" effect and the resulting error in velocity calculation. It was also observed that the size of the side-wall "band" of deposit decreases slowly into a "bow" curve as the horseshoe vortex increase in size.

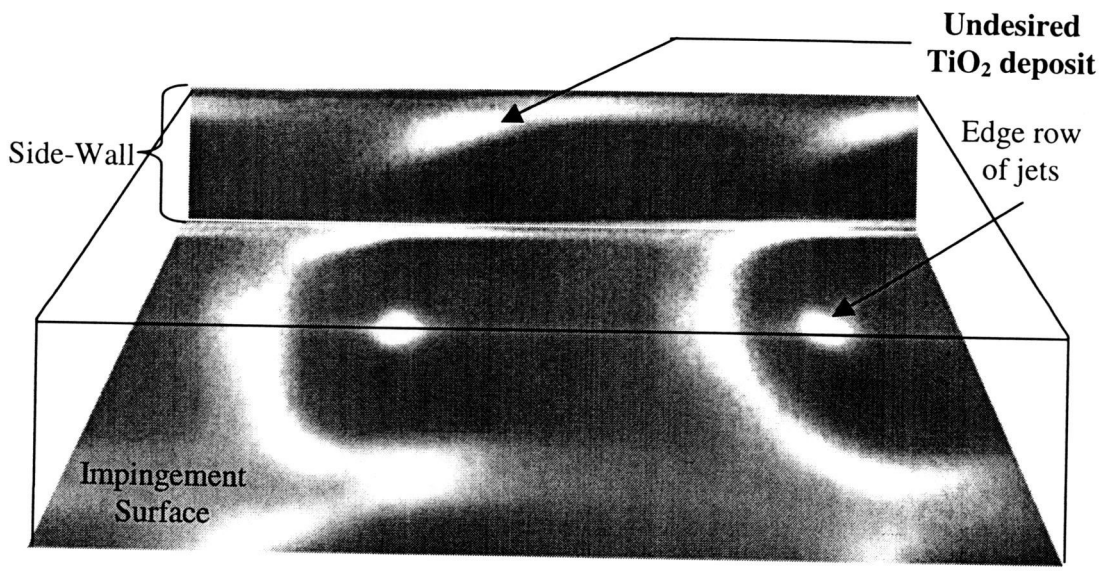

Fig. 5.68 Side-wall flow visualization

Discussion

Surface flow visualization, jet orifice flow coefficient measurements, and PIV measurements of the entire flow field were used to interpret the complex flow features. Based on these measurements, specific conclusions can be drawn about this flow and the impact of the flow parameters on the flow structure.

The surface flow visualization provides details of the flow pattern at the impingement surface. For all the jet configurations, the jets spread over the surface creating cells defined by multiple detachment-reattachment zones with a characteristic "horseshoe" shape around each jet. The cell size appears to expand slightly along the downstream flow direction (less than 4%). The impingement point distance to the upstream detachment zone was measured and was found to be linearly decreasing function of the downstream position, with a 50% drop for H/D_H=4 and 70% drop for H/D_H=2. On the other hand, the results show little change over the range of Re studied. Therefore, decreasing the impingement distance affects the cells distribution with increased sensitivity to changes along the flow direction.

The flow coefficient, C_D, was found to decrease along the downstream crossflow direction. The average is 0.70 for the round jet and 0.80 for the cusped ellipse (0°) jet. As Re is increased, C_D drops slightly (less than 5% over the range of Reynolds numbers studied) for all of the configurations. However when the impingement distance H/D_H is decreased, C_D is much more sensitive to the

crossflow effect. Locally, C_D is largest close to the back of the channel and decreases at the exit, therefore the overall average value $<C_D>$, increases slightly (<5 %). It must be kept in mind that these results assume uniform mass flow rate from all of the jets in the array.

The PIV results provide a large amount of information about the two-dimensional flow structure. Each jet appears to split near the impingement surface, into downstream flow and return-flow. This return flow and the flow coming from the upstream jets collide and create a large recirculation region identified as a "surface vortex" that can be observed upstream of the jet column. Close to the back of the channel, this vortex appears large and relatively slow. Further downstream, the surface vortex location moves downstream relative to the jet column. Its size appears to decrease while its strength increases. Its proximity with the jet creates a large flow entrainment that leads to a relatively large acceleration and a slight deviation of the jet column in the impingement area. This phenomenon appears to be sensitive to Re. The higher the value of Re, the closer the surface vortex is to the jet.

The vorticity field provides details of the various large-scale vortex locations resulting from the interaction of the crossflow and the jets. Shown in Figure 5.69 are the overall averaged mean vorticity squared, $<\omega^2>$, and for each jet array configuration. The corresponding flow conditions are shown in Table 5.1. Pairs of counter-rotating vorticity are visible, delimiting the jet shearing layers. For lower Re, the jet is mostly well defined. For increasing Re, the symmetry breaks-up

Table 5.1 Jet array flow conditions

	Reynolds Number	
Jet Array Configuration	Low Re1	High Re2
Circular jet	9740	15,800
Cusped ellipse (0°)	8,570	13,500
Cusped ellipse (90°)	8,570	13,500

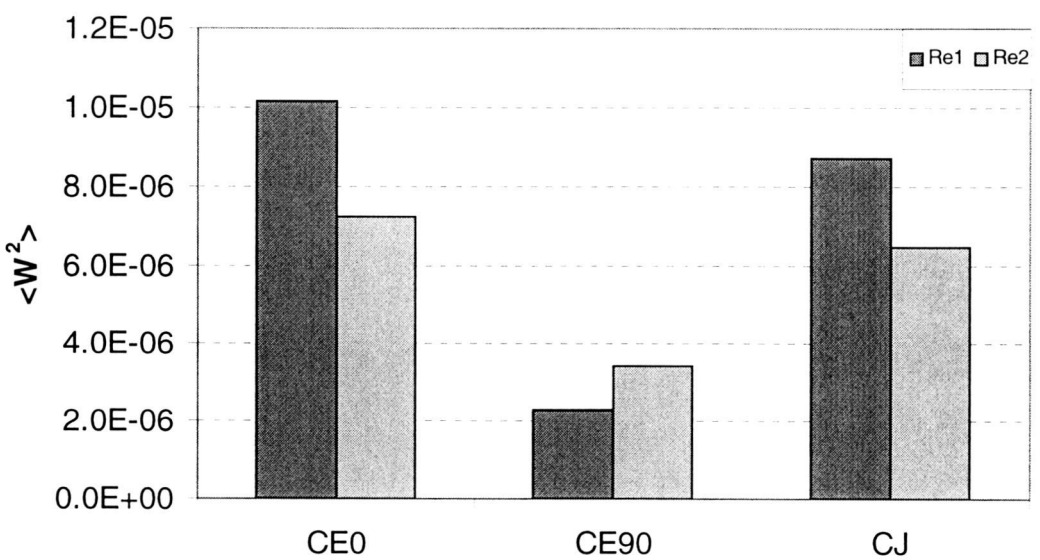

Figure 5.69 Comparison of $<\omega^2>$ levels

and pockets of vorticity can be found throughout the flow field. The "cusped" ellipse shows a much better spreading of these pockets all over the channel associate with a greater level of intensity. Compared to the circular jet, a 16% increase in averaged vorticity, $<\omega^2>$, is observed for the cusped ellipse (0°) jet array while in the (90°) orientation, the $<\omega^2>$ level is 4 times smaller. Therefore, significant changes to the mean vorticity level can be made by changes in the jet orifice geometry.

The TKE field shows wide variations from one configuration to the other. Figure 5.70 shows the spatially averaged levels of <TKE> for each jet array. One can clearly see that the cusped ellipse in the (0°) position generates more turbulence than in the (90°) position. Compared to the circular jet, a 36% increase in TKE is observed throughout the overall surface.

The Mean squared Vorticity (Wms) fields also show wide variations from one jet array to the other. In Figure 5.71, the overall spatially averaged dissipation for each jet configuration is shown. Again, one can see that cusped ellipse (0°) generates 97% more dissipation than the circular jet while the (90°) configuration shows its relative weakness.

For a Re, the above results seem to change notably. The circular jet and the cusped ellipse in the (0°) configuration show similar intensity of TKE and dissipation with the circular jet results only a few percent larger than the cusped

ellipse (0°) jet array. The cusped ellipse (90°) jet array improves slightly, but the results stay well below the values for the two other configurations.

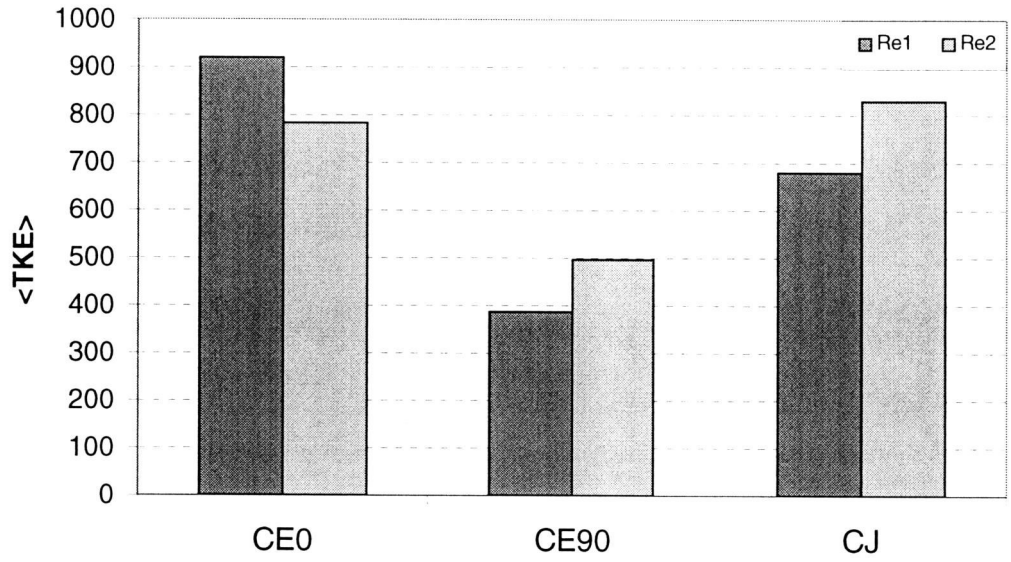

Figure 5.70 Comparison of <TKE> levels

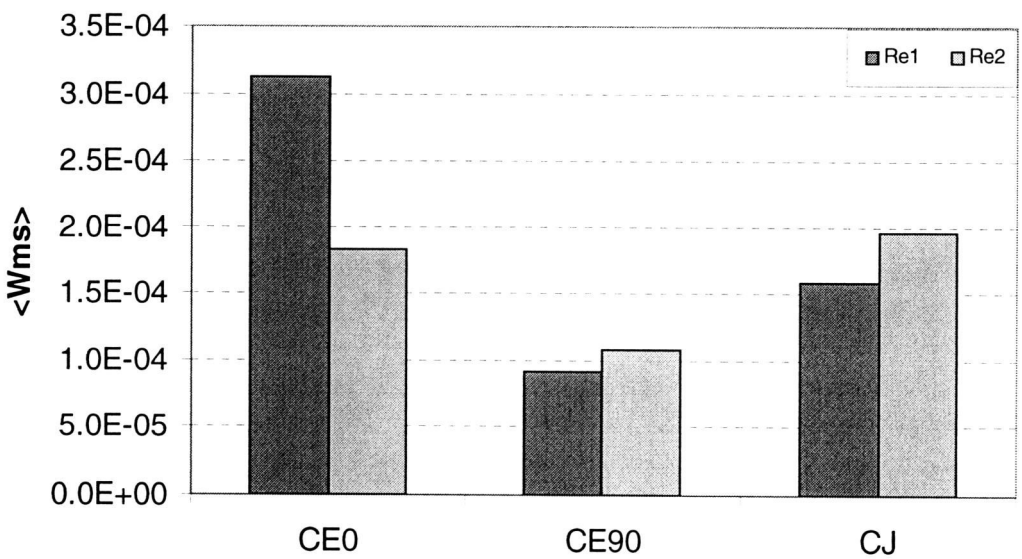

Figure 5.71 Comparison of <Wms> levels

CHAPTER VI

CONCLUSION AND RECOMMENDATIONS

The experimental investigation presented in this study was focused on an array of jets impinging on a surface, enclosed by three walls. The air, leaving in one preferential direction, generates a crossflow that interacts with the jet structure of the other jets. Two main objectives guided the study. The first focused on understanding this crossflow-to-jet interaction along the flow and its dependence on various parameters such as the impingement distance and the flow rate. The second objective was to identify any specific behavior for a particular jet array with a non-axisymmetric geometry.

The study of two 7x7 array of impinging air jets was based on three experimental methods used to define the jet structure within the channel and in the vicinity of the impingement surface. The first array was a circular orifice array while the second was a "cusped" ellipse array. The non-symmetry of the cusped ellipse shape allowed two alignments with the crossflow. For all case, the flow area for each configuration was held constant.

Surface flow visualization, jet orifice flow coefficient measurements, and PIV measurements of the entire flow field were used to interpret the complex flow features. The visual observation of the impinging pattern shows similar results for all the different configurations. The jets generated cells that progressively expand in size with increasing crossflow. The flow coefficient of each jet decreases

monotonically and quasi-linearly along the crossflow direction, while the average value increases only a few percent for increasing Re. The most variation along the flow was found for the lowest impingement distance, $H/D_H=1$. PIV measurements of the entire flow field in the vicinity of the jet exits reveals complex flow structures: a large rotating vortex created by the merging of the crossflow and the jet column return-flow, moves towards the jet column as the crossflow increases in strength. This proximity generates multiple turbulent flow patterns. This may have consequences for improved surface cooling applications.

For low Re, the cusped ellipse jet array placed in the (0°) position, major axis aligned parallel to the crossflow, appears to generate significantly more turbulence than the circular jet array, while for higher Re, both configurations show similar results. However, in the (90°) position, major axis normal to the crossflow, the results show considerably smaller increases in the levels of turbulence when compared with the circular jets. Meanwhile, evidence of axis switching in the jet column development tends to prove that a transport in the lateral direction could be a secondary factor to take into account for surface cooling efficiency.

Recommendations for further studies are to find a different "tracer" for the PIV measurements that would combine a good reflectivity for flow visualization with a smaller tendency to agglomerate and to use a faster digital camera to capture PIV fields at a higher data rate to better measure the turbulence. Recommendations for future studies involve 3D flow visualization methods in order to obtain the full channel flow structure and the lateral flow structure development.

BIBLIOGRAPHY

1. Raghunathan S. and Reid I.M, 1981, "A study of multiple jets", *AIAA Journal*, Vol. 19, No. 1, pp. 124-126.

2. Moustafa G.H., Sundararajan T. and Rathakrishnan E., 1993, "Mean streamwise velocity measurement of a triple jet of equilateral triangular configuration", *Transactions of the ASME*, Vol. 115, pp. 534-536.

3. Moustafa G.H. and Rathakrishnan E., 1993, "Studies of the flowfield of multijet with square configuration", *AIAA Journal*, vol. 37, No. 7, pp. 1189-1190.

4. Villermaux, E. and Hopfinger, E. J., 1994, "Periodically Arranged Co-flowing Jets", *Journal of Fluid Mechanics*, Vol. 263, pp. 63-92.

5. Kim S.-W. and Benson T.J., 1993, "Fluid flow of a row of jets in crossflow - a numerical study", *AIAA Journal*, Vol. 31, No. 5, pp. 806-811.

6. Arjocu S. C. and Liburdy J. A., 1999, "Near surface characterization of an impinging elliptic jet array", *Transactions of the ASME*, vol. 121. Pp. 384-390

7. Barata J.M.M., Durao D.F.G. and Heitor M.V., 1992, "Velocity Characteristics of Multiple Impinging Jets Through a Crossflow", *Journal of Fluids Engineering*, Vol. 114, pp. 231-239.

8. Barata J.M.M., 1996, "Fountain Flows Produced by Multiple Impinging Jets in a Crossflow", *AIAA Journal*, Vol. 34, No. 12, pp. 2523-2530.

9. Florschuetz L.W. and Isoda Y., 1983, "Flow distributions and discharge coefficient effects for jet array impingement with initial crossflow", *Transactions of the ASME*, Vol. 105, pp. 296-304.

10. Bernard A., Brizzi L.-E. and Bousgarbies J.-L., 1999, "Study of Several Jets Impinging on a Plane Wall: Visualizations and Laser Velocimetry Investigation", *Transactions of the ASME*, Vol. 121, pp. 808-812.

11. Metzger, D.E., "Heat Transfer in Gas Turbine Engines," Winter Annual Meeting of The American Society of Mechanical Engineers, Boston, Massachusettes, Vol. 87, December 13-18, 1987.

12. Kanokjaruvijit, K., "Effects of orifice geometry and surface boundary condition on heat transfer of impinging jet array", MS Thesis, Oregon State University, February 2000.

APPENDICES

APPENDIX A

Uncertainty Analysis

This appendix is presented to determine the uncertainty of the following dependent and independent variables: volumetric flow rate, mass flow rate, Reynolds number, and the flow coefficient.

Volume Flow Rate

According to the gas correction formula provided by the manufacturer, the readout volumetric flow rate needs to be corrected according to the downstream pressure and temperature immediately downstream of the flowmeter.

$$Q_{Actual}=Q_{Readout} \text{ x } CF$$

CF is the correction factor: $CF = \sqrt{\frac{14.7 + P(psig)}{14.7}} \sqrt{\frac{530}{460 + T(^{\circ}F)}}$.

The uncertainty for the volume flow rate is estimated from the Kline-McClintock relation:

$$u_{Q_{Actual}} = \sqrt{\left(\frac{\partial Q_{Actual}}{\partial Q_{Readout}} u_{Q_{Readout}}\right)^2 + \left(\frac{\partial Q_{Actual}}{\partial Q_{CF}} u_{CF}\right)^2 + u_{manu}^2 + u_{cal}^2}.$$

The readout uncertainty was $u_{Qreadout}$= 0.5 CFM. The temperature was measured using a calibrated thermocouple (J type) connected to a Fluke data logger, introducing an error of U_T= 0.04°C. The pressure was measured using a pressure gauge that introduced an uncertainty of U_P=1 PSI. Since the flowmeter used was only 4% full-scale accurate, it has been re-calibrated using a more accurate flowmeter (2% full-scale accurate) reducing the manufacturer uncertainty to u_{manu}=0.4 CFM. This re-calibration induced a bias of u_{cal}=0.5 CFM. The final uncertainty for the actual flowrate ranged from 4.47 to 6.98%.

Mass flow rate

The mass flow rate, $\dot{M}$, was computed based on the density, ρ, and the previously obtained actual flow rate, Q_{Actual}. It is calculated from the expression:

$$\dot{M} = \rho Q_{Actual} = \frac{P_0}{RT_0} Q_{Actual}.$$

The uncertainty for the mass flow rate is estimated from the Kline-McClintock relation:

$$u_{\dot{M}} = \sqrt{\left(\frac{\partial \dot{M}}{\partial P_0} u_{P_0}\right)^2 + \left(\frac{\partial \dot{M}}{\partial T_0} u_{T_0}\right)^2 + \left(\frac{\partial \dot{M}}{\partial Q_{Actual}} u_{Q_{actual}}\right)^2}.$$

The plenum pressure, P_0, was measured with a pressure transducer, introducing an error of u_{P_0}=0.75 psi. The temperature was measured using a calibrated J-type thermocouple connected to a Fluke data logger, introducing an error of u_{T_0}= 0.04°C. The uncertainty in mass flow rate was computed to be 4.5 to 7.0%.

Reynolds number

The Reynolds number is calculated as follows:

$$Re = \frac{\dot{M} D_H}{\mu A_T},$$

where $\dot{M}$ is the mass flow rate, D_H is the jet hydraulic diameter, and A_T is the total orifice surface area. The total surface area being A_T= 49xA_j. The uncertainty for the mass flow rate is estimated from the Kline-McClintock relation:

$$u_{Re} = \sqrt{\left(\frac{\partial Re}{\partial \dot{M}} u_{\dot{M}}\right)^2 + \left(\frac{\partial Re}{\partial D_H} u_{D_H}\right)^2 + \left(\frac{\partial Re}{\partial A_j} u_{A_j}\right)^2}.$$

The instrument to measure D_H and A_j introduced an uncertainty of u_{D_H}=3μm and u_{A_j}=0.007μm^2, respectively. Finally, the uncertainty for the Reynolds number ranged from 4.51 to 7.01%.

Flow coefficient

The flow coefficient is calculated from the expression:

$$C_D = \frac{\frac{\dot{M}}{A_t}}{P_0\left(\frac{P}{P_0}\right)^{\frac{1}{\gamma}}\sqrt{\frac{2\gamma}{R.T_0(\gamma-1)}.\left[1-\left(\frac{P}{P_0}\right)^{\frac{\gamma-1}{\gamma}}\right]}},$$

where $\dot{M}$ is the mass flow rate, A_T is the total orifice surface area, P_0 is the plenum chamber pressure, P is the impingement surface pressure, and T_0 is the plenum chamber temperature.

The secondary part under the square root in the denominator is a second order term for the error definition. Therefore, it is discarded for the final error computation. The uncertainty for the flow coefficient is estimated from the Kline-McClintock relation:

$$u_{C_D} = \sqrt{\left(\frac{\partial C_D}{\partial \dot{M}} u_{\dot{M}}\right)^2 + \left(\frac{\partial C_D}{\partial P_0} u_p\right)^2 + \left(\frac{\partial C_D}{\partial P} u_p\right)^2 + \left(\frac{\partial C_D}{\partial T_0} u_{T_0}\right)^2}.$$

The pressure transducer used for the measurement of the plenum and impingement surface pressure introduced an uncertainty of $u_{P_0} = u_P$=0.75psi. The temperature was measured using a calibrated J-type thermocouple connected to a Fluke data logger, introducing an error of u_{To}= 0.04°C. Finally, the uncertainty for the flow coefficient ranged from 4.11% to 7.16%.

Impingement Flow Pattern Characteristics

The size of the surface vortex stagnation, S_C, the distances between the surface vortex stagnation and the stagnation point, S_{VS}, and the relative distance between two respective surface vortex stagnation, S_S, have been measured directly from the images of the flow pattern in pixels, then re-scaled in mm. The uncertainty on the edge location, u_x, was 1 pixel.

S_C is expressed as $S_C = X_{S2} - X_{S1}$, where X_{S2} and X_{S1} are the stagnation point edges location. The uncertainty in S_C can be expressed as:

$$u_{S_C} = \sqrt{\left(\frac{\partial S_C}{\partial X_2} u_{X_2}\right)^2 + \left(\frac{\partial S_C}{\partial X_1} u_{X_1}\right)^2} = \sqrt{2}.u_x$$

Separation distances, such as S_{VS} and S_S, are expressed as $S = (X_{V2} + X_{V1} - X_{S2} - X_{S1})/2$, where X_{V2} and X_{V1} are the vortex stagnation edges location. The uncertainty in S_{VS} and S_S can be expressed as:

$$u_S = \sqrt{4\left(\frac{\partial S}{\partial X} u_X\right)^2} = u_x$$

Finally, the uncertainty for S_C was $0.10 \times D_H$, and the uncertainty for S_{VS} and S_S was $0.07 \times D_H$.

APPENDIX B

Flow Visualization Software analysis and methods

The PIV analyses have been obtained using VISIFLOW™, a software package that computed the velocity vector fields of the flow. The method used to compute the PIV flow-fields for this dissertation were obtained by cross-correlation of pairs of images, taken at a known time delay.

First, the general parameters of the flow are entered: (1) the pulse separation, which is the time between the multiple laser pulses, (2) the image scale, obtained from the channel size on the images (in pixels), and (3) the real size of the channel (in m). The software support both square and non-square image pixels. The software divides the two pictures into cells, which are compared/correlated against the corresponding cell of the second picture. For each cell, a cross correlation function is yielded where one (or more) more peaks appears, distributed non-symmetrically. These secondary peaks are due to correlation with other particles rather than themselves. These peaks, which are usually of lower amplitude can be thought of as noise, and can occasionally give bad results. The spatial position of the main peak within the cross-correlation image of the region gives the average frequency of the multiple particle image separation in the PIV image. This information is then combined with the time separation to give the average velocity vector of the particles in the cell. Various parameters are applicable for this

analysis. The analysis resolution determines the precision used to compute the cross correlation function of the images. It can be adjusted from (16x16) to (256x256) pixels. Higher values give greater accuracy of velocity determination. The degree of overlap of the correlation area can be varied from 0% (areas are bordering, but not overlapping), to 50%, to 75% (areas are overlapping by 75%). Finally, a choice between two algorithms is given: Gaussian fit or center of gravity. The Gaussian option uses a two-dimensional Gaussian function, which is adjusted to fit around the highest point of the peak. The center of gravity option thresholds the pixels around the peak maximum, and then computes a center of gravity for the threshold shape. This center of gravity is taken as the new maximum. The Gaussian option is potentially more accurate, but the center of gravity option may give better results when the correlation peaks have a distorted shape.

All of the PIV analyses in this dissertation have been obtained using the Gaussian algorithm with the following parameters: (1) the pulse separation was set to 2μs, (2) the image scale was 118μm/pixel μm/pixel, and (3) the analysis resolution was 256x256 pixels, with a 75% overlap.

APPENDIX C

Raw Data Tables

Table C.1 Jet arrays orifice geometry

	Perimeter (m)	Hydraulic Diameter (m)	Orifice Area (m^2)	Total Area (m^2)
Circular	0.003989832	0.001270	1.26687E-06	6.207E-05
Cusped Ellipse	0.004453128	0.001138	1.26697E-06	6.208E-05
(% difference)	(11.612%)	(10.38%)	(0.0079%)	(0.015%)

Table C.2 Flow coefficient, Circular Jet

$H/D_H=1$

Q_{actual}	Re	$C_{D\,(PT1)}$	$C_{D\,(PT2)}$	$C_{D\,(PT3)}$	$C_{D\,(PT4)}$	$C_{D\,(PT4)}$	$C_{D\,(PT5)}$	$C_{D\,(PT6)}$	$<C_D>$
14	9,863	0.810	0.782	0.743	0.699	0.660	0.758	0.758	0.744
16	11,884	0.776	0.750	0.713	0.675	0.639	0.727	0.727	0.715
18	13,922	0.744	0.721	0.686	0.651	0.622	0.699	0.699	0.689
20	16,767	0.742	0.717	0.683	0.642	0.619	0.695	0.695	0.685

$H/D_H=2$

Q_{actual}	Re	$C_{D\,(PT1)}$	$C_{D\,(PT2)}$	$C_{D\,(PT3)}$	$C_{D\,(PT4)}$	$C_{D\,(PT4)}$	$C_{D\,(PT5)}$	$C_{D\,(PT6)}$	$<C_D>$
14	9,736	0.758	0.744	0.728	0.717	0.711	0.737	0.737	0.733
16	11,683	0.717	0.705	0.692	0.683	0.678	0.699	0.699	0.696
18	13,661	0.711	0.701	0.689	0.682	0.677	0.695	0.695	0.693
20	15,984	0.698	0.689	0.680	0.674	0.670	0.684	0.684	0.683

$H/D_H=3$

Q_{actual}	Re	$C_{D\,(PT1)}$	$C_{D\,(PT2)}$	$C_{D\,(PT3)}$	$C_{D\,(PT4)}$	$C_{D\,(PT4)}$	$C_{D\,(PT5)}$	$C_{D\,(PT6)}$	$<C_D>$
14	9,736	0.729	0.718	0.710	0.705	0.703	0.719	0.719	0.715
16	11,539	0.699	0.690	0.683	0.678	0.677	0.690	0.690	0.687
18	13,582	0.711	0.702	0.696	0.692	0.691	0.703	0.703	0.700
20	15,818	0.693	0.687	0.682	0.679	0.678	0.687	0.687	0.685

$H/D_H=4$

Q_{actual}	Re	$C_{D\,(PT1)}$	$C_{D\,(PT2)}$	$C_{D\,(PT3)}$	$C_{D\,(PT4)}$	$C_{D\,(PT4)}$	$C_{D\,(PT5)}$	$C_{D\,(PT6)}$	$<C_D>$
14	9,740	0.717	0.707	0.702	0.699	0.700	0.712	0.712	0.707
16	11,545	0.689	0.681	0.677	0.675	0.675	0.685	0.685	0.681
18	13,592	0.703	0.695	0.691	0.689	0.690	0.699	0.699	0.695
20	15,829	0.687	0.681	0.679	0.677	0.677	0.684	0.684	0.681

Table C.3 Flow coefficient, Cusped ellipse (0°)

$H/D_H=1$

Q_{actual}	Re	$C_{D\,(PT1)}$	$C_{D\,(PT2)}$	$C_{D\,(PT3)}$	$C_{D\,(PT4)}$	$C_{D\,(PT4)}$	$C_{D\,(PT5)}$	$C_{D\,(PT6)}$	$<C_D>$
14	8,736	0.949	0.901	0.836	0.758	0.698	0.867	0.867	0.839
16	10,421	0.943	0.893	0.826	0.747	0.691	0.856	0.856	0.830
18	12,260	0.969	0.915	0.845	0.763	0.708	0.877	0.877	0.851
20	14,198	0.973	0.915	0.842	0.760	0.706	0.877	0.877	0.850

$H/D_H=2$

Q_{actual}	Re	$C_{D\,(PT1)}$	$C_{D\,(PT2)}$	$C_{D\,(PT3)}$	$C_{D\,(PT4)}$	$C_{D\,(PT4)}$	$C_{D\,(PT5)}$	$C_{D\,(PT6)}$	$<C_D>$
14	8,559	0.845	0.824	0.812	0.792	0.777	0.817	0.817	0.812
16	10,224	0.817	0.797	0.786	0.771	0.755	0.790	0.790	0.787
18	11,829	0.836	0.818	0.807	0.792	0.776	0.810	0.810	0.807
20	13,584	0.852	0.835	0.824	0.809	0.794	0.826	0.826	0.824

$H/D_H=3$

Q_{actual}	Re	$C_{D\,(PT1)}$	$C_{D\,(PT2)}$	$C_{D\,(PT3)}$	$C_{D\,(PT4)}$	$C_{D\,(PT4)}$	$C_{D\,(PT5)}$	$C_{D\,(PT6)}$	$<C_D>$
14	8,562	0.829	0.814	0.806	0.800	0.789	0.815	0.815	0.810
16	10,162	0.811	0.798	0.791	0.785	0.775	0.801	0.801	0.794
18	11,767	0.822	0.810	0.803	0.797	0.788	0.813	0.813	0.807
20	13,517	0.823	0.813	0.806	0.801	0.792	0.814	0.814	0.809

$H/D_H=4$

Q_{actual}	Re	$C_{D\,(PT1)}$	$C_{D\,(PT2)}$	$C_{D\,(PT3)}$	$C_{D\,(PT4)}$	$C_{D\,(PT4)}$	$C_{D\,(PT5)}$	$C_{D\,(PT6)}$	$<C_D>$
14	8,568	0.813	0.804	0.797	0.793	0.789	0.808	0.808	0.802
16	10,169	0.784	0.776	0.770	0.765	0.762	0.782	0.782	0.774
18	11,777	0.803	0.796	0.791	0.786	0.783	0.803	0.803	0.795
20	13,530	0.819	0.813	0.807	0.803	0.801	0.819	0.819	0.812

Table C.4 Flow coefficient, Cusped ellipse (90°)

H/D_H=1

Q_{actual}	Re	$C_{D\,(PT1)}$	$C_{D\,(PT2)}$	$C_{D\,(PT3)}$	$C_{D\,(PT4)}$	$C_{D\,(PT4)}$	$C_{D\,(PT5)}$	$C_{D\,(PT6)}$	$<C_D>$
14	8,543	0.830	0.810	0.763	0.708	0.663	0.780	0.780	0.762
16	10,469	0.848	0.828	0.779	0.723	0.678	0.795	0.795	0.778
18	12,318	0.865	0.844	0.794	0.737	0.691	0.809	0.809	0.793
20	14,182	0.874	0.852	0.800	0.741	0.696	0.816	0.816	0.799

H/D_H=2

Q_{actual}	Re	$C_{D\,(PT1)}$	$C_{D\,(PT2)}$	$C_{D\,(PT3)}$	$C_{D\,(PT4)}$	$C_{D\,(PT4)}$	$C_{D\,(PT5)}$	$C_{D\,(PT6)}$	$<C_D>$
14	8,545	0.818	0.815	0.803	0.786	0.774	0.792	0.792	0.797
16	10,470	0.781	0.780	0.768	0.754	0.749	0.759	0.759	0.764
18	11,886	0.797	0.795	0.783	0.769	0.758	0.776	0.776	0.779
20	13,565	0.810	0.812	0.800	0.787	0.776	0.793	0.793	0.796

H/D_H=3

Q_{actual}	Re	$C_{D\,(PT1)}$	$C_{D\,(PT2)}$	$C_{D\,(PT3)}$	$C_{D\,(PT4)}$	$C_{D\,(PT4)}$	$C_{D\,(PT5)}$	$C_{D\,(PT6)}$	$<C_D>$
14	8,540	0.800	0.793	0.786	0.776	0.769	0.792	0.792	0.787
16	10,136	0.803	0.796	0.789	0.779	0.773	0.795	0.795	0.790
18	11,809	0.795	0.791	0.784	0.775	0.769	0.788	0.788	0.785
20	13,561	0.800	0.795	0.790	0.782	0.776	0.789	0.789	0.789

H/D_H=4

Q_{actual}	Re	$C_{D\,(PT1)}$	$C_{D\,(PT2)}$	$C_{D\,(PT3)}$	$C_{D\,(PT4)}$	$C_{D\,(PT4)}$	$C_{D\,(PT5)}$	$C_{D\,(PT6)}$	$<C_D>$
14	8,526	0.801	0.790	0.785	0.780	0.779	0.801	0.801	0.791
16	10,054	0.791	0.780	0.776	0.771	0.770	0.792	0.792	0.782
18	11,789	0.785	0.775	0.772	0.767	0.766	0.784	0.784	0.776
20	13,460	0.811	0.802	0.798	0.794	0.792	0.808	0.808	0.802